POLITECNICO DI MILANO
Dipartimento di Ingegneria Civile e Ambientale

Corso di Laurea Magistrale in Ingegneria Civile

POTENTIAL FLOW MODEL IMPLEMENTATION OF A MOORED FLOATING BODY

Relatore: Prof. Ing. Renata Archetti
Correlatori: Prof. Ing. Giuseppe Passoni
Ing. Maria Gabriella Gaeta, Ph.D.

Studente:
Giacomo Segurini
Matr. 880874

Anno accademico 2018/2019
Sessione I

Abstract

This thesis aims at building a three Degrees of Freedom (DoFs) mathematical model in order to represent the motion of a cylindrical buoy subjected to the action of regular waves, calibrating it through a comparison between the model results and the experiments performed at LIDR (Laboratory of Hydraulic Engineering of Alma Mater Studiorum University of Bologna). The simplicity of the model is a very important feature as it should be used as a preliminary study to understand how the buoy moves under a certain incident wave in terms of oscillation amplitude and frequency. The model has been written by making use of the software Matlab.

The cylindrical buoy is placed at the middle of a channel and anchored at the bottom through a mooring system made of four catenaries.

The mathematical model consists of two main parts: the first part is developed in the frequency domain while the second one in the time domain. In the frequency domain part, hydrodynamic coefficients are computed through the specific function named Nemoh (developed by LHEEA Laboratoire de recherche en Hydrodynamique, Énergétique et Environnement Atmosphérique di Nantes), which first builds a grid to divide the body surface in little elements and then performs an integration with the boundary element method (BEM). The result represented by the assessment of excitation force, radiation force and added mass coefficients are expressed as function of frequency. Then, the coefficients for the response amplitude operator (RAO) are calculated again as function of frequency.

The model in the time domain makes use of the hydrodynamic coefficients estimated in the frequency domain in order to build the actual mathematical model, which consists of an equation of motion built considering inertia and drag forces, neglecting diffraction contribution. Furthermore, mooring system has first been analysed and then inserted into the equation of motion to complete the model. The implemented mooring system model contains constants on which a calibration process has to be performed.

Experimental tests consist of perturbing the free surface with a wave generator and creating a situation in which the buoy is solicited by regular waves. Different tests have been carried out as to analyse several wave conditions, in particular with different wave heights and periods. Two GoPro cameras capture the body motion, and videos of the tests are then analysed in order to be able to compare the data with the model results.

The model results are then compared with the laboratory ones in order to calibrate the model itself and define the value of calibration coefficients. This procedure allows to be able to compute the buoy dynamics with an accurate potential flow model.

Contents

List of figures

List of Tables

1

Introduction

1.1 Renewable energy

Abundant presence of energy resources has permitted industrial and social development of today society. In facts, society growth and evolution is based on an increasing consumption of energy resources, which has also brought to energy production and storage too. It is then true that human activities need a lot of energy in order to maintain and improve society itself, and the amount of requested energy grows according to the living standard which has today become very high in some parts of the world. Unfortunately, this great energy amount that society needs is today based on fossil fuels as primary energy resources, and fossil fuel consumption is then what current world economic model is based on. The greatest deal fossil fuels bring is GreenHouse Gasses (GHG) production: their effect upon natural and anthropic systems is already visible, with large consequences on humans' health, biodiversity, migrations, natural hazards and resources availability.

GHG can be considered the principal cause of the climate change that we are nowadays able to experience and which, together with the previously reported effects, is defined through the temperature growth. The latter aspect has been studied by the IPCC (Intergovernmental Panel on Climate Change), which has developed models to predict climate change effects and especially temperature growth following several scenarios, concerning the human behaviour in terms of use of fossil fuels during next decades. Figure 1.03 shows the different model predictions in terms of temperature increase, associated to CO2 concentration until 2100. The worst one predicts an increase until 5°C in 2100, which represents a catastrophic scenario for humankind and for life on planet earth in general.

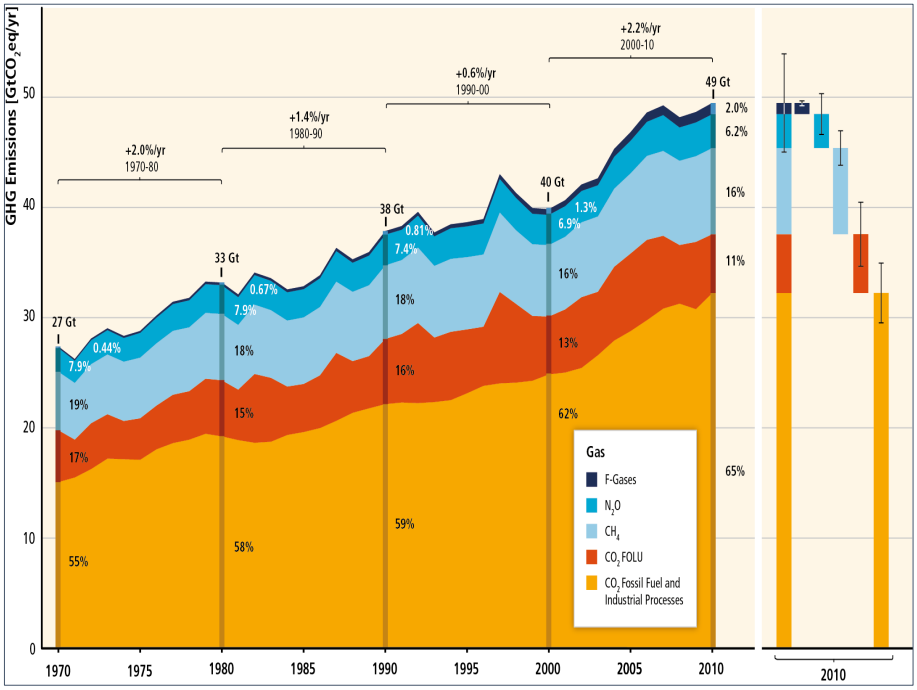

Figure 1.01 Total annual anthropogenic GHG Emissions by Groups of Gases 1970-2010 [1].

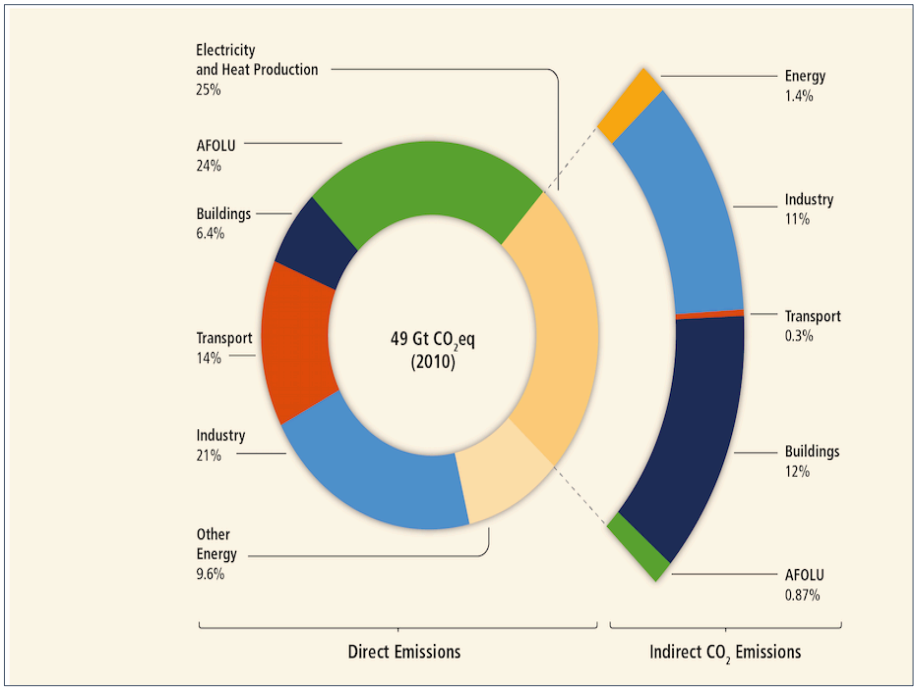

Figure 1.02 Greenhouse Gas Emissions by Economic Sectors [1].

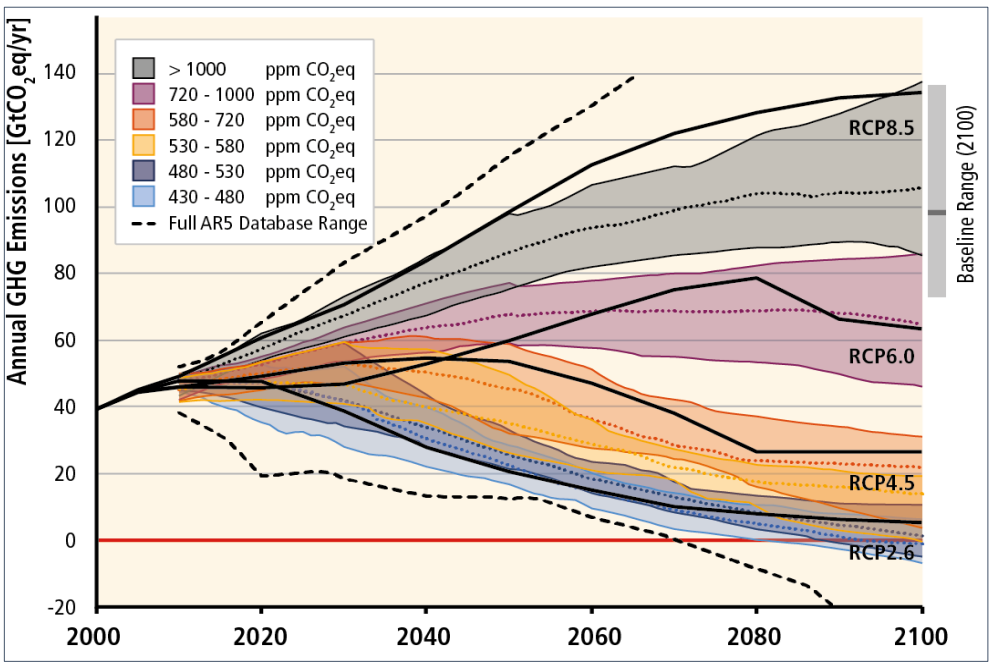

Figure 1.03 Total GHG Emissions in all AR5 Scenarios [1].

In order to prevent such predictions from becoming a reality, a new energetic model has to be developed. This should be fulfilled by reducing fossil fuels demand replacing it by renewable resources: they are represented by all those kind of energy sources that can be replenished at the same rate as it is consumed during a human timescale. The natures of renewable energies are four: geothermal, hydroelectric, biomass and solar.

Geothermal energy is the heat from the Earth and it is clean and sustainable. Resources of geothermal energy range from the shallow ground to hot water and hot rock found a few miles beneath the earth's surface, and down even deeper to the extremely high temperatures of molten rock called magma. For this reason, it can be hard to reach. Hydroelectric energy merely takes advantages of the potential energy stored in high quoted water reservoirs typically found in mountainous systems. Biomass energy can be produced by any material of organic-vegetable origin (trees, plants, farming or industrial waste, urban waste). It is regarded as more of a valid resource for the environment than an answer to the energy shortage. As such the growth and informed use of the large quantities of vegetation across the world can contribute to improving the ecosystem through a greater level of carbon dioxide absorption. The use of plants fuelled by biomass energy makes it possible to complete the so-called “carbon cycle”: the amount of carbon emitted through their use is the same as the amount absorbed by the plants to produce the same quantity of biomass. It is partially considered as a solar type of energy resource, since plants in order to thrive need to capture energy from the sun by means of

photosynthesis. Last form of renewable energy is the one coming from the sun, which can be captured directly both as photovoltaic and thermal, storing energy as heat in water with the second one, or indirectly. The most diffused form indirect solar energy is wind energy.

1.1.2 Wind energy

Wind energy is due to the difference in terms of solar energy that invests earth surface at the equator and the poles, creating as consequence a remarkable pressure gap in the atmosphere producing winds and moving huge amounts of air from high pressure regions to low pressure ones, [4,35]. It is interest to report that this process causes an energy density increase, as wind energy ($0.5kW/m^2$), in average more concentrated than solar energy ($0.1 - 0.3kW/m^2$). Wind power is one of the fastest-growing renewable energy technologies. Usage is on the rise worldwide, in part because costs are falling. Global installed wind-generation capacity onshore and offshore has increased by a factor of almost 50 in the past two decades, jumping from 7.5 GW in 1997 to some 487 GW by 2016, according to figures from the Renewable Energy Network for the 21st Century (REN21). Production of wind electricity doubled between 2009 and 2013 as it is possible to understand from the histogram of Figure 1.04 and Figure 1.05. Many parts of the world have strong wind speeds, but the best locations for generating wind power are sometimes remote ones. Offshore wind power offers tremendous potential: higher wind speeds are available offshore compared to on land, so offshore wind power electricity generation is higher per amount of capacity installed. For this reason, offshore wind energy use is increased a lot in the last decade and at the end of 2017, the total worldwide offshore wind power capacity was 18.8 GW [3].

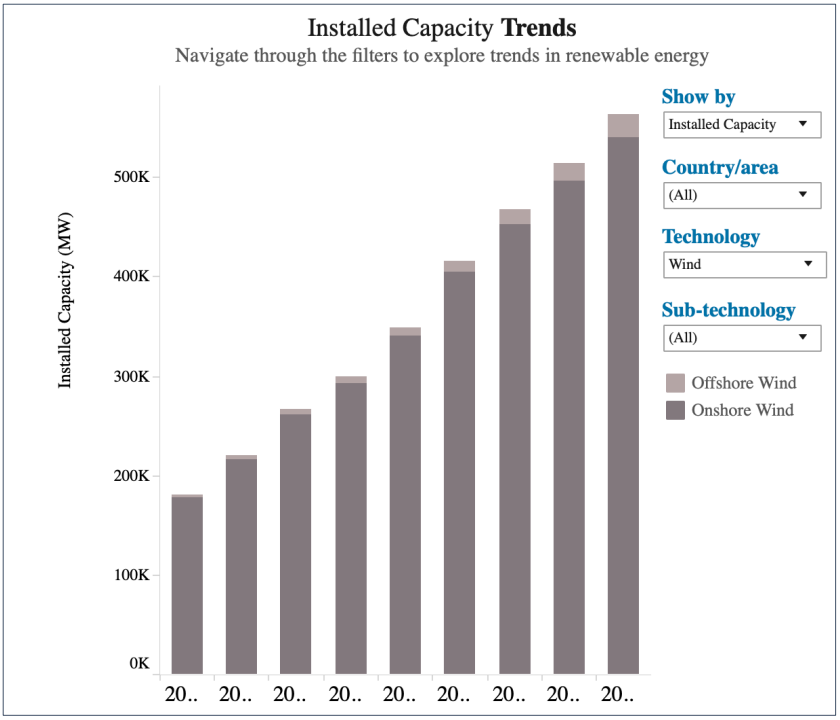

Figure 1.04 Installed Capacity trends for both Onshore and Offshore Wind energy [2].

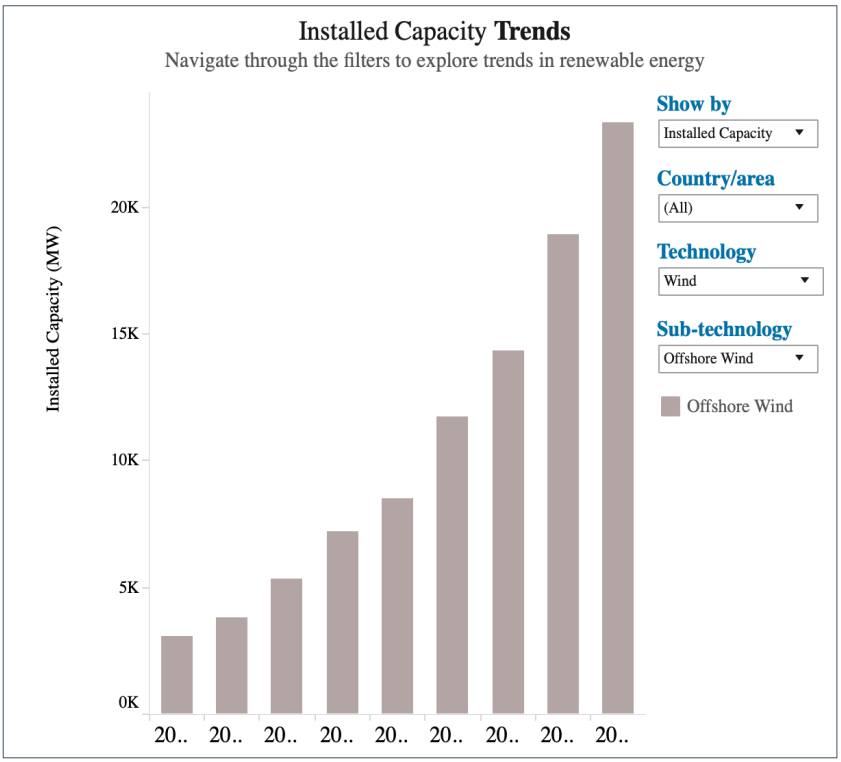

Figure 1.05 Installed Capacity trends for Offshore Wind energy [2].

Offshore wind power includes inshore water areas such as lakes, fjords and sheltered coastal areas, utilizing traditional fixed-bottom wind turbine technologies, as well as deeper-water areas utilizing floating wind turbines.
The most used way of placing wind turbines is to gather a lot of turbines together forming a wind farm. Large wind farms are formed by hundreds of wind turbines to cover total surfaces of hundreds of square miles. All the largest offshore wind farms are currently in northern Europe, especially in the United Kingdom and Germany, which together account for over two thirds of the total offshore wind power installed worldwide. Figure (1.06) shows the example a wind farm located in the North Sea in Germany.

Figure 1.06 Offshore wind farm in the North Sea.

Wind is used to produce electricity using the kinetic energy created by air in motion. This is transformed into electrical energy using wind turbines or wind energy conversion systems. Wind first hits turbine blades, causing them to rotate and turn the turbine connected to them. That changes the kinetic energy to rotational energy, by moving a shaft which is connected to a generator, and thereby producing electrical energy through electromagnetism. The amount of power that can be harvested from wind depends on the size of the turbine and the length of its blades. The output is proportional to the dimensions of the rotor and to the cube of the wind speed. Theoretically, when wind speed doubles, wind power potential increases by a factor of eight.

Wind-turbine capacity has increased over time. In 1985, typical turbines had a rated capacity of 0.05 MW and a rotor diameter of 15 m. Today new wind power projects have turbine capacities of about 2 MW onshore and 3–5 MW offshore. Commercially available wind turbines have reached 8 MW capacity, with rotor diameters of up to 164 metres. The average capacity of wind turbines increased from 1.6 MW in 2009 to 2 MW in 2014 [4].
Several are the mooring system that allow the single wind turbine to maintain its position offshore, as shown in Figure 1.07. The first is the one using a ballast stabilized buoy linked to the bottom through a mooring system consisting of catenaries. The second system consists of a tension leg platform positioned under the free surface and then linked to the bottom through mooring lines anchored to the bottom itself. Another possible method is the one that takes advantage of barge platform floating at the MWL anchored to the bottom with catenaries.
The first mooring method is the one that is going to be analysed in the following chapters of this thesis. As all the other mooring system, it is meant to decrease the motion of the wind turbine in response to sea state and the consequently wave action. They are a very stable kind of buoys because both of their form which reaches deep water and their mass: their design is based on a weighted mass at the bottom to keep it upright, a big container of water in the middle, and typical air-filled hull at the top.

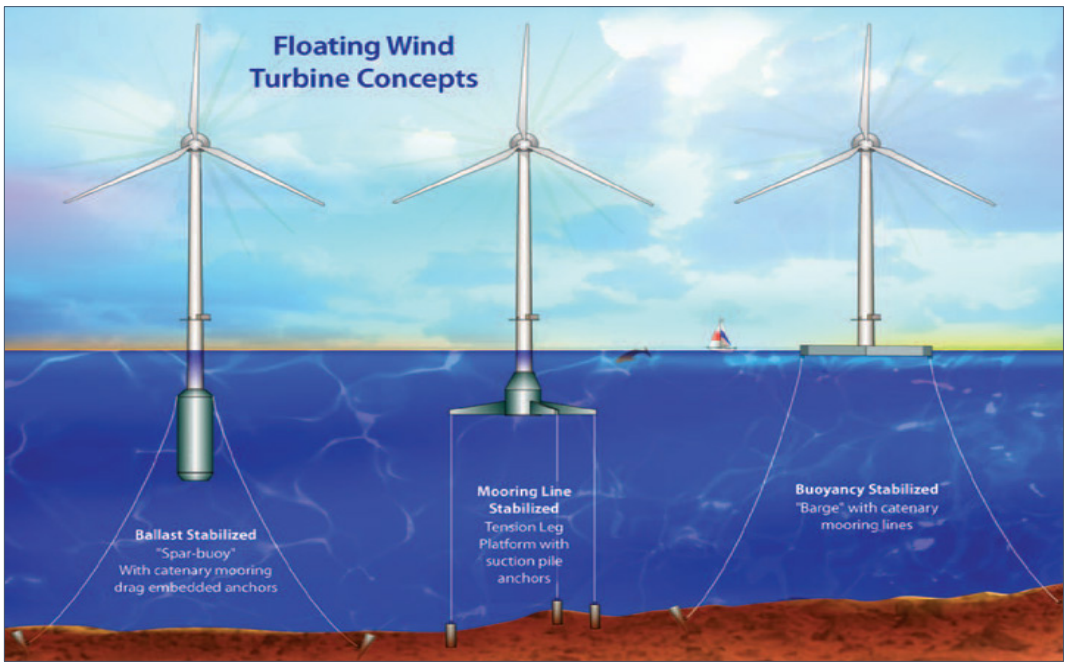

Figure 1.07 Mooring system for buoys.

1.2 Scope of the thesis

This thesis aims at developing a potential flow model able to represent the dynamics of a floating body. In particular, the scope is to analyse the motion of a cylindrical buoy under the action of regular waves both experimentally and mathematically, and perform a model calibration by comparing the results of the two approaches. The mathematical model has been carried out with the software Matlab, writing several routines that will be better exposed in chapter 4. The model describes the buoy dynamics in two dimensions, and it is based on few hypothesis and approximations which tend to limit its applicability range. Nevertheless, it has to serve as a simple one in order to predict the experimental buoy motion under the action of the tested sea states. Simplicity of the model implies the use of some hypothesis that allow to neglect several forces and effects that are actually present, but that are worth not to be considered as suggested by the aim of the model. Furthermore, it will be possible to apply the model to other floating bodies.

1.3 Structure of the thesis

This document is developed in five chapters, introduction included, where an overview of renewable energies is given and the aim that this work is meant to have is explained.
The second chapter is devoted to the presentation of the theoretical background that has been needed to develop such study. Particular attention is given to the linear wave theory, Airy theory [38], through which waves have been studied and their characteristics have been described. Then, principal aspects of fluid-structure interaction theory are carefully explained in such a way to understand their application in this thesis case.
Third chapter is dedicated to the laboratory set-up description. First, the whole set-up is described focusing on the dimensions of both the buoy and all the other structure involved. Furthermore, attention is given to the gauges recording system installed into the channel through which the free surface perturbation during simulation events is recorded, explaining how they work and how to perform their calibration. Last part of third chapter is related to the study of such waves, with particular attention to their propagation in time together with wave particles velocities, representing an important aspect from which the following development of the model is influenced by.
In the fourth chapter the essence of this work, the mathematical model, is developed. First a careful explanation of all the forces involved is carried on, describing their physical meaning and how they have been modelled when inserting them into the

equation itself. Besides, during this part, further important hypothesis are reported as to better understand why some forces have been neglected or considered. The construction of motion equation is then described gathering all the acting forces selected. The mooring system is involved too, and a particular section is written in order to describe how it has been modelled. After that, the real model is finally explained, starting from a frequency domain part where principal characteristics of the cylindrical buoy motion are discovered arriving to the second and most important part of the code, time domain one, where equation is solved and buoy motion is actually determined. Particular attention is paid to the used algorithm, explained in a dedicated section.

Last chapter is devoted to the comparison between model and laboratory results, both in frequency and time domain, and to the calibration of the model itself. Plots of buoy motions under several incident waves and calibration coefficients values are reported. At the end, some conclusions are drawn.

2

Theoretical background

2.1 Linear wave theory

In the present thesis, the wave generation is performed taking into account linear wave theory. This is possible because of the characteristics of the waves created by the generator, which is programmed to create regular waves.

Linear wave theory is based on the velocity potential concept, which represents the spatial integral form of velocity. In particular, under the hypothesis of

- Irrotational motion;
- Inviscid fluid;
- Conservative forces.

it is possible to say that a velocity potential exists and it should satisfy the continuity equation

$$\nabla \cdot u = 0 \tag{2.01}$$

or

$$\nabla \cdot \nabla \phi = 0 \tag{2.02}$$

The divergence of a gradient leads to the Laplace equation (2.03), which must hold throughout the fluid.

$$\nabla^2 \phi = \frac{\partial^2 \phi}{\partial x^2} + \frac{\partial^2 \phi}{\partial y^2} + \frac{\partial^2 \phi}{\partial z^2} = 0 \tag{2.03}$$

Furthermore, under the same hypothesis it is possible to derive Bernoulli equation (2.04) too, as

$$\frac{\partial \phi}{\partial t} + \frac{1}{2}|\nabla \phi|^2 + \frac{p}{\rho} + gz = 0 \tag{2.04}$$

Together, these equations represent irrotational theory bases for wave motion.

Besides, experimental studies have demonstrated that another constraint must be added to maintain the theory validity. The period of the sea waves must be within the following range of almost 1s < T < 30s. In essence, it must not be too much high in order to be able to neglect the influence of bottom friction and at the same time not too much low in order to be able to neglect surface tension.
For what this thesis is concerned, as the work is developed on a small scale laboratory setup, the considered period is around 1s, so it is still possible to apply this theory.

Unfortunately, due to the difficulties related to the nonlinearity of the boundary conditions, it is not possible to achieve exact analytical solutions of the problem. So, in order to obtain valid analytical solutions, it is necessary to simplify the problem. For this reason, in the following paragraphs the linear wave theory, also known as first order theory, will be developed.
This theory is applied within the boundaries of a domain, and in particular the adopted one is delimited by four boundaries: two lateral ones, the bottom one and the free surface boundary.
Considering a flat and impermeable bottom, both Laplace equation and the kinematic bottom boundary condition are linear. The problem is that both kinematic and dynamic free surface boundary conditions are nonlinear, so, firstly, they have to be linearized.
As already said, the two free surface conditions are respectively expressed by the kinematic equation (2.05) and the dynamic equation (2.06):

$$\frac{\partial \eta}{\partial t} + \frac{\partial \phi}{\partial x}\frac{\partial \eta}{\partial x} + \frac{\partial \phi}{\partial y}\frac{\partial \eta}{\partial y} + \frac{\partial \phi}{\partial z} = 0 \quad \text{for } z = \eta(x, y, t) \tag{2.05}$$

$$g\eta + \frac{\partial \phi}{\partial t} + \frac{1}{2}\left[\left(\frac{\partial \phi^2}{\partial x} + \frac{\partial \phi^2}{\partial y} + \frac{\partial \phi^2}{\partial z}\right)\right] = 0 \quad \text{for } z = \eta(x, y, t) \tag{2.06}$$

First, these equations are directly nonlinear for the unknowns η and ϕ, but they also present a hidden nonlinearity because of the fact that they have to be applied on the free surface $z = \eta(x, y, t)$, which is the unknown itself. In order to make these conditions useful for the achievement of an analytical solution they have to be linearized, and to do this the introduction of new constrains is necessary.
Figure 2.01 fully describes a progressive periodic wave and all its involved parameters; this wave propagates in a flat-bottomed channel, following the x axis, and is mainly defined by its period T, its wavelength L and its wave height H =

2a. Analyzing the figure, the proportion among the different parameters is clear and the orders of magnitude can securely be determined:

$$\eta = O(H) \quad \frac{\partial \eta}{\partial t} = O\left(\frac{H}{T}\right) \quad \frac{\partial \eta}{\partial x} = O\left(\frac{H}{L}\right) \tag{2.07}$$

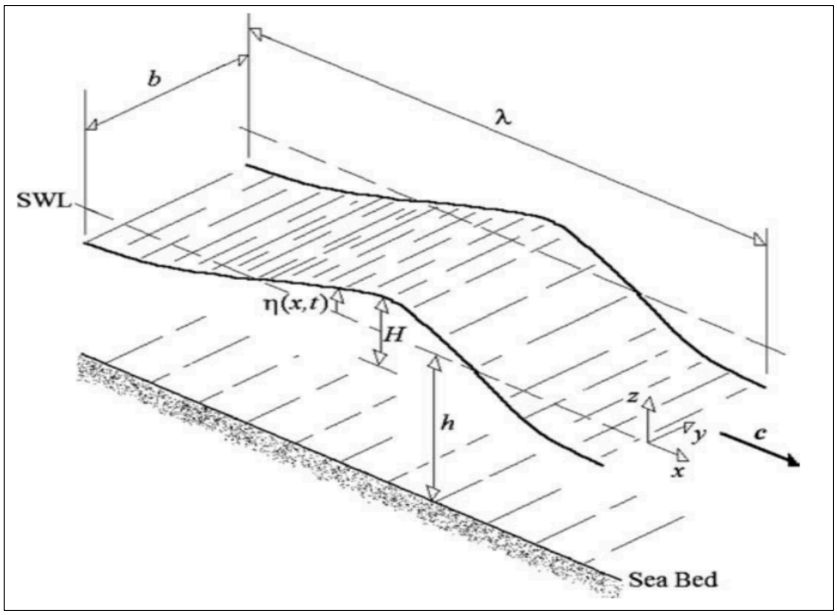

Figure 2.01 Parameters of a progressive periodic wave [5].

The maximum velocity of the water particles can be approximated to πH/T, which leads to the following relation:

$$u_{max} = v_{max} = w_{max} = \frac{\partial \phi}{\partial x_{max}} = \frac{\partial \phi}{\partial y_{max}} = \frac{\partial \phi}{\partial z_{max}} = \frac{\pi H}{T} = O\left(\frac{H}{T}\right) \tag{2.08}$$

Being wave celerity c = L/T, the nonlinear terms have the following orders of magnitude:

$$\frac{\partial \phi}{\partial z} = O\left(\frac{H}{T}\right) = O\left(c\frac{\Phi}{L}\right) \tag{2.09}$$

$$\frac{\partial \eta}{\partial z} = O\left(\frac{H}{T}\right) = O\left(c\frac{\partial \phi}{\partial z}\right) \tag{2.10}$$

$$\frac{\partial \phi}{\partial x}\frac{\partial \eta}{\partial x} = \frac{\partial \phi}{\partial y}\frac{\partial \eta}{\partial y} = O\left(c\frac{H^2}{L^2}\right) = \frac{H}{L}O\left(\frac{\partial \phi}{\partial z}\right) \tag{2.11}$$

These relations proof that the nonlinear terms have an order of magnitude H/L times the one of the linear terms. Assuming that the wave slope is ε = H/L << 1, the nonlinear terms of the free surface BC can be, in first approximation, neglected due to their small influence. In this way, direct nonlinearity has been suppressed.
In order to suppress the hidden nonlinearity too, a similar approach can be used. Indeed, it is possible to express the condition as a Taylor series referring to $z = \eta = 0$:

$$\frac{\partial \phi}{\partial z}(x,\eta,t)=\frac{\partial \phi}{\partial z}(x,0,t)+\eta\ \frac{\partial^2 \phi}{\partial z^2}(x,0,t)+... \tag{2.12}$$

Being that

$$\eta\frac{\partial \phi^2}{\partial z}(x,0,t)=O\left(\frac{H}{T}\frac{H}{h}\right)=O\left(c\frac{H}{L}\frac{H}{h}\right) \tag{2.13}$$

the second order term of the series can be neglected if compared with the first order term if $H/h << 1$.
This means that if the ratio between wave height and water depth is sufficiently low, the free surface boundary condition can be applied at $z = \eta = 0$, suppressing the hidden nonlinearity. At the end, the kinematic and dynamic free surface boundary conditions are linearized and become:

$$\frac{\partial \eta}{\partial t}-\frac{\partial \phi}{\partial z}=0 \quad \text{for } z=0 \tag{2.14}$$

$$g\eta+\frac{\partial \phi}{\partial t}=0 \quad \text{for } z=0 \tag{2.15}$$

It is possible to gather the two free surface conditions into one single equation considering the relation (2.16) and simplifying the problem.

$$\eta=\frac{1}{g}\frac{\partial \phi}{\partial t}\Big|_{z=0} \tag{2.16}$$

At last, also considering the expressions of the bottom boundary condition (2.19) and the linearized Bernoulli equation (2.18), where p+ is the pressure excess induced by the wave in the fluid, it is possible to get to the final expression of the linearized problem through which a solution for the velocity potential and the velocity field can now be found:

$$\nabla^2\phi=\frac{\partial^2 \phi}{\partial x^2}+\frac{\partial^2 \phi}{\partial y^2}+\frac{\partial^2 \phi}{\partial z^2} \tag{2.17}$$

$$p^{+}=p+\rho gz=-\rho\frac{\partial\phi}{\partial t} \tag{2.18}$$

$$\frac{\partial^2\phi}{\partial t^2}+g\frac{\partial\phi}{\partial z}=0 \quad \text{for } z=0 \tag{2.19}$$

$$\frac{\partial\phi}{\partial z}=0 \quad \text{for } z=-h \tag{2.20}$$

In order to find a solution for the velocity potential, some additional hypothesis need to be introduced:

- Constant period T: waves need to be periodic in time (equation (2.21));
- Constant shape: waves need to be periodic in space throughout the entire domain (equation (2.22));
- Bidimensional waves in the xz plane, hence neglecting the y component of the velocity potential.

$$\frac{\partial\phi}{\partial x}(x,\eta,t)=\frac{\partial\phi}{\partial x}(x,\eta,t+T) \tag{2.21}$$

$$\frac{\partial\phi}{\partial x}(x,\eta,t)=\frac{\partial\phi}{\partial x}(x+L,\eta,t) \tag{2.22}$$

The periodicity hypothesis shows that the previously described phase celerity relation c = L/T is constant, finding a valid link between the spatial and the temporal domain. This link can be used by formulating a new variable theta, which fulfils the conditions described above:

$$\theta=2\pi\left(\frac{x}{L}-\frac{t}{T}\right) \tag{2.23}$$

Dependencies now change from $\eta(x,t)$ and $\varphi(x,z,t)$ to $\eta(\theta)$ and $\varphi(\theta,z)$. Two new parameters are introduced in order to achieve a full determination of the equations of motion (2.13 -2.16). These are called the wave number $k = 2\pi/L$ and the angular frequency $\omega = 2\pi/T$. Applying the changes, the simplified Laplace system of equations can be written again as follows:

$$\theta=kx-\omega t \tag{2.24}$$

$$\frac{\partial^2\phi}{\partial z^2}+k^2\frac{\partial^2\phi}{\partial\theta^2}=0 \tag{2.25}$$

$$p^{+}=p+\rho gz=-\rho\frac{\partial\phi}{\partial t} \tag{2.26}$$

$$\frac{\partial\phi}{\partial z}+\frac{\omega^2}{g}\frac{\partial^2\phi}{\partial\theta^2}=0 \qquad for\ z=0 \tag{2.27}$$

$$\frac{\partial\phi}{\partial z}=0 \quad \text{for } z=-h \tag{2.28}$$

$$\frac{\partial\phi}{\partial\theta}\left[\theta=-2\pi\frac{t}{T},z\right]=\frac{\partial\phi}{\partial\theta}\left[\theta=-2\pi\left(1-\frac{t}{T}\right),z\right] \tag{2.29}$$

Equation (2.25) is an Ordinary Differential Equation (ODE) and its resolution leads to the velocity potential and the free water surface, [6]:

$$\phi(\theta,z)=\frac{ag}{\omega}\frac{\cosh[k(h+z)]}{\cosh(kh)}\sin(\theta) \tag{2.30}$$

$$\eta=a\cos(\theta) \tag{2.31}$$

However, the problem is not yet fully defined since the wave number k is still an arbitrary number, given that no relation between ω and k has been provided yet, and thus a wavelength cannot be computed for a fixed period. In order to solve this problem, the dynamic free surface BC is used. In particular, combining the free surface BC in (2.31) and the derivative of (2.30), the following expression are derived:

$$\left[\frac{\partial\phi}{\partial z}\right]_{z=0}=\frac{ag}{\omega}\tanh(kh)\sin(\theta) \tag{2.32}$$

$$\left[\frac{\partial^2\phi}{\partial z^2}\right]_{z=0}=-ag\omega\sin(\theta) \tag{2.33}$$

At this point, substituting both the obtained equations into (2.16) the dispersion relation (2.34) is obtained. Firstly, this relation gives a link between ω and k, thus between T and L:

$$\omega^2=gk\tanh(kh) \tag{2.34}$$

Being $L=cT$, also considering the expression of frequency ($w=2\pi/T$) and wave number ($k=2\pi/L$), between ω, k and c the following relation exists:

$$\omega=ck \tag{2.35}$$

Substituting into the dispersion relation it is possible to get to the wave velocity expression (2.36)

$$c=\sqrt{\frac{gL}{2\pi}\tanh\left(\frac{2\pi h}{L}\right)} \tag{2.36}$$

Being wave celerity computed as the ratio between wave length and wave period c=L/T, substituting in the previous expression it is possible to write down dispersion relation such as in equation (2.37). The latter allows the computation of wave length L when h and T are known, in an iterative way since L compares in both left and right member of the implicit equation.

$$L=\frac{gL^2}{2\pi}\tanh\left(\frac{2\pi h}{L}\right) \tag{2.37}$$

2.1.1 Velocity field

Once dispersion relation is obtained, the velocity field can be easily computed by applying the spatial derivatives to the velocity potential. Since the application of the hypothesis of bidimensional domain only two components are yielded, the horizontal velocity u and the vertical one w.

$$u(\theta,z)=\frac{\partial\phi}{\partial x}=\frac{agk}{\omega}\frac{\cosh[k(h+z)]}{\cosh(kh)}\cos(\theta) \tag{2.38}$$

$$w(\theta,z)=\frac{\partial\phi}{\partial z}=\frac{agk}{\omega}\frac{\sinh[k(h+z)]}{\cosh(kh)}\sin(\theta) \tag{2.39}$$

The velocity expression is a product of three different groups, each representing different contributes: the first term expresses the wave characteristics i.e. wave amplitude, wave number and wave frequency, the second one reflects the velocity variation along the vertical position, and the third group states the armonic behavior of the wave, [6]. From the previous formulas, it is possible to define the principal characteristics of the velocity field under a standing wave. Figure 2.02 represents the velocity field under a wave progressing according to the arrow direction: both horizontal and vertical velocities are maximum at the MWL and experience a decrease along with the depth until they reach their minimum values at the bottom. Furthermore, horizontal velocity reaches its maximum value at wave crest, where particles move in the wave propagation direction, and its

minimum one at the wave cave, where particles move with opposite direction. On the other hand, max vertical velocity is reached between wave crest and cave.

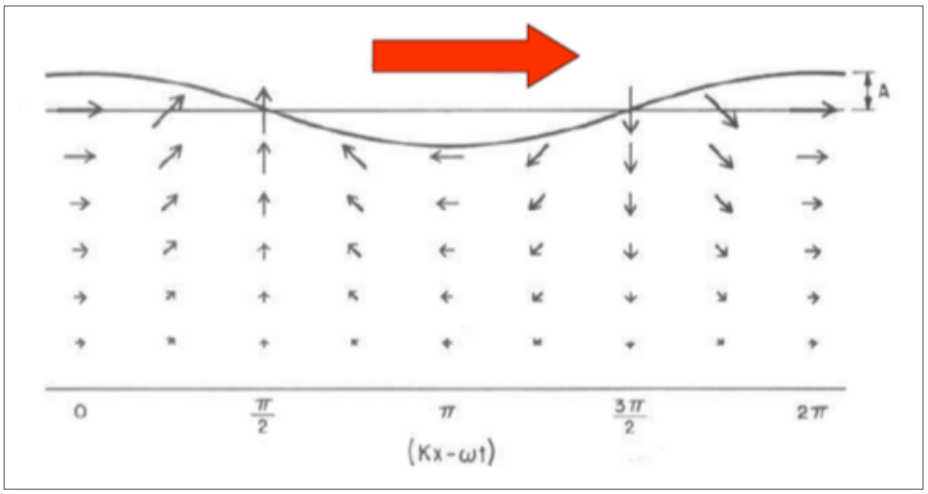

Figure 2.02 Velocity field under a progressive periodic wave.

Once velocity field is known, it is possible to compute water particles trajectories and acceleration, performing integration and derivation of velocity expressions respectively. In particular, to reach a better understanding of the linear wave theory, particles trajectories are derived as follows:

$$x_p(t)=x_0+\int u[x(t),z(t)]dt \tag{2.40}$$

$$z_p(t)=z_0+\int w[x(t),z(t)]dt \tag{2.41}$$

Performing the integral and after some mathematical simplification passages, the expressions of the trajectories become:

$$x_p(t)=x_0-a\frac{\cosh[k(h+z_0)]}{\cosh(kh)}\sin(\theta_0) \tag{2.42}$$

$$z_p(t)=z_0-a\frac{\sinh[k(h+z_0)]}{\cosh(kh)}\cos(\theta_0) \tag{2.43}$$

where $\theta_0 = \omega t - kx_0$, [6].
Introducing the terms α and β

$$\alpha = a\frac{\cosh[k(h+z_0)]}{\sinh(kh)} \tag{2.44}$$

$$\beta = a\frac{\sinh[k(h+z_0)]}{\sinh(kh)} \tag{2.45}$$

Dividing equations (2.42) and (2.43) by α and β respectively, squaring them and then adding them, the obtained result is the well known ellipse equation:

$$\frac{[x_p(t)-x_0]^2}{\alpha^2}+\frac{[z_p(t)-z_0]^2}{\beta^2}=1 \tag{2.46}$$

The parameters α and β define the shape of the ellipse according with water depth. In deep water conditions the ellipses tend to take the form of perfect circles with decreasing radius when approaching increasing depth (Figure (2.03 a)). In shallow water condition the ellipse are quite eccentric, varying the minor radius only when approaching increasing depth Figure 2.03b. In intermediate depth cases, both major and minor radius vary approaching increasing depth.

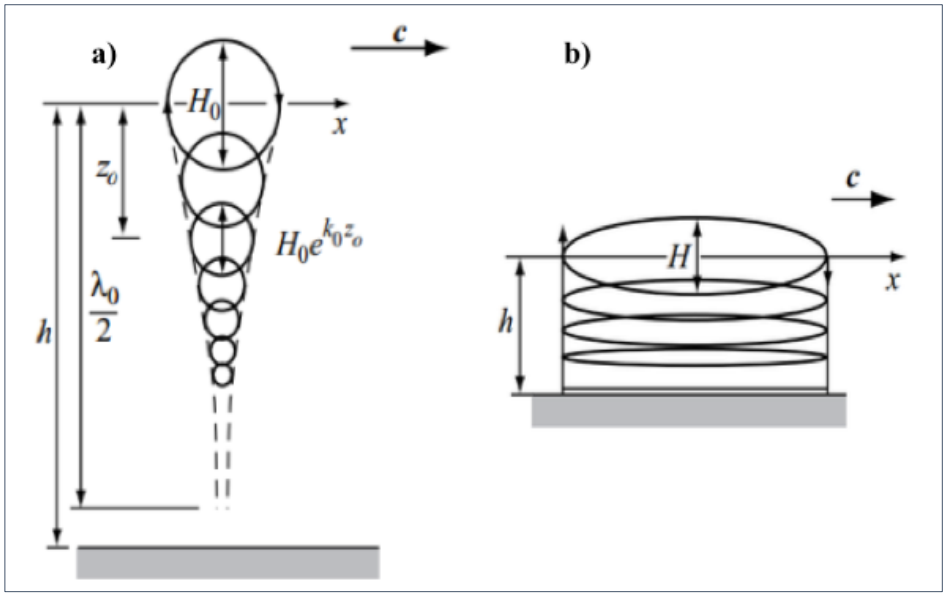

Figure 2.03 Wave particle trajectories for deep water and shallow water situations [5].

The definition of shallow and deep water cases is not immediately achievable, but it depends both on water depth and on the characteristics of the wave: for example tidal or tsunamis waves or any wave with extremely long periods and wave lengths can be shallow water waves in deep ocean too.
So, the definition of the different situations is linked to the calculation of a particular dimensionless quantity defined as the ratio between water depth h and wave length L. A ratio h/L<1/20 represents the situation of shallow water, when h/L>1/2 we are in the deep water case, while when the ratio assumes any value

between the two previous limits the intermediate case takes place. The same conclusion could be achieved by considering a different dimensionless quantity, the product of the wave number k and the water depth h: according to this quantity, $kh<\pi/10$ represents a shallow water situation, $kh>\pi$ a deep water one, and all the included vales are representative of an intermediate situation.

Besides, according to each situation, simplifications exist about the computation of wave characteristics as wave length and celerity. In particular, for what deep water is concerned, being $kh>>1$ it is possible to simplify expression (2.37) in the form (2.47), as wave length in deep water is often called L_0

$$L=L_0=\frac{gT^2}{2\pi} \tag{2.47}$$

Furthermore, L_0 can also be written as

$$L_0= 1.56\ T^2 \tag{2.48}$$

Wave celerity in deep water, also called c_0 becomes

$$c=\sqrt{\frac{g\ L_0}{2\pi}} \tag{2.49}$$

For what shallow water is concerned, the simplified expression of wave length and wave celerity are written below through equations (2.50) and (2.51) respectively.

$$L=\frac{g\ T^2\ h}{L}=T\sqrt{gh} \tag{2.50}$$

$$c = \sqrt{gh} \tag{2.51}$$

When the condition happens to be an intermediate one, wave length and wave celerity have to be computed through the application of the standard equations (2.36) and (2.37).

2.1.2 Pressure distribution

The pressure distribution throughout the fluid domain is obtained through the linearized Bernoulli's equation:

$$p^{+}=-\rho\frac{\partial\phi}{\partial t}=\rho ag\frac{\cosh[k(h+z)]}{\cosh(kh)}\cos(\theta)=\rho g\eta(\theta)\frac{\cosh[k(h+z)]}{\cosh(kh)}=\rho gK_p\eta(\theta) \quad (2.52)$$

The coefficient K_p represents the pressure response factor and it always follow the condition $K_p \leq 1$, depending on the value of z. Considering the expression of p+, pressure profile can be described as

$$p=p^{+}-\rho gz=\rho g(K_p\eta-z) \quad (2.53)$$

When z = 0 then Kp = 1 thus resulting in a pressure p = ρgη. Therefore, in the crest of the wave pressure is p = ρga and in the trough of the wave pressure is p = −ρga. As the depth of the study point grows also the pressure does having the component p+ less important, since the hydrostatic component after a certain value is dominant.

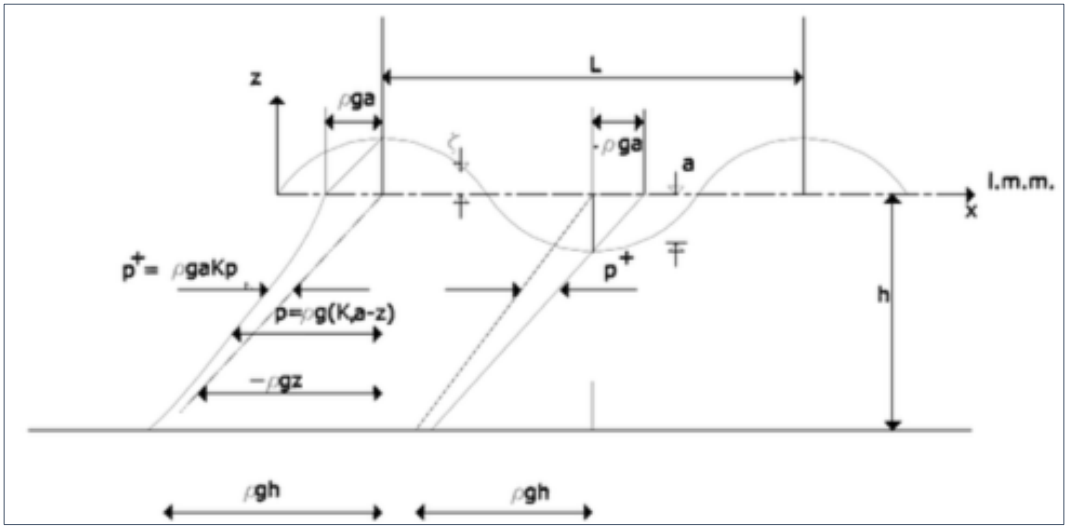

Figure 2.04 Hydrostatic and hydrodynamic pressure under the crest and the cave of a progressive wave [7].

2.1.3 Energy of the wave motion

In linear wave theory, dissipative phenomena are neglected and therefore the energy related to the wave motion consists of two components only: potential energy and kinetic energy. Being the motion an oscillating one, energy at a certain point (x, z) is time dependent. However, the energy at a certain point at a certain time is not really a matter of major interest from the engineering point of view. However, the energy at a certain point at a certain time is not really a matter of major interest from the engineering point of view.

Referring to Figure 2.05, the elementary fluid column of unitary width, length equal to dx and (h+η), it has the following elementary potential energy:

$$d\overline{E}_{p1}=gh_G\,dm \tag{2.54}$$

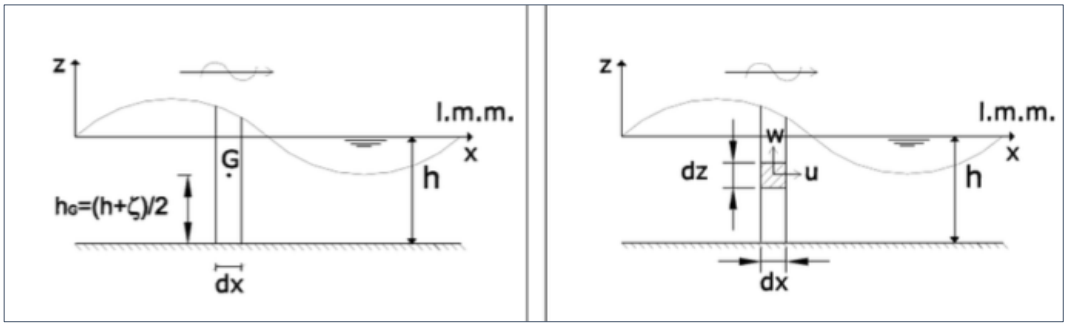

Figure 2.05 Discretization of the wave for the computation of potential and kinetic energy [7].

where h_G represents the distance between the column centre of mass and the potential energy calculation plane, while dm represents the fluid column mass.

$$h_G=\frac{h+\eta}{2} \tag{2.55}$$

$$dm=\rho(h+\eta)dx \tag{2.56}$$

Substituting last two equations in (2.54) it becomes

$$d\overline{E}_{p1}=\frac{1}{2}\rho g(h+\eta)^2\,dx \tag{2.57}$$

which is function of space x and time t, due to the fact that

$$\eta=\eta(x,t)=a\cos(kx-\omega t) \tag{2.58}$$

In order to obtain potential energy density, it is necessary to integrate (2.57) over space x and time t. In particular the kind of energy density that has to be found is an average value both over surface and time, so the easiest way to do this is to integrate over a wave length and a wave period as follows:

$$\overline{E}_{p1}=\frac{1}{LT}\int_t^{t+T}\int_x^{x+L} d\overline{E}_{p1}=\frac{\rho g}{2LT}\int_t^{t+T}\int_x^{x+L}(h+\eta)^2\,dx\,dt \tag{2.59}$$

Integration has been performed along x only because of the hypothesis of cylindrical wave that propagates in direction x.
The result of the integral is represented by the following expression (2.60) which consists of two contributes, the first one is related to the situation without wave motion while the second one to the wave motion only.

$$\overline{E}_{p1}=\frac{\rho g}{2}\left(h^2+\frac{a^2}{2}\right)=\rho g\frac{h^2}{2}+\rho g\frac{a^2}{4} \tag{2.60}$$

Taking in account the second term only, it is possible to describe the potential energy density due to the presence of wave motion as

$$\overline{E}_p=\rho g\frac{a^2}{4} \tag{2.61}$$

To develop the kinetic energy expression, the schematic shown in Figure 2.05b is followed. The study area is also an elementary region of fluid mass, which length, height and width are respectively dx, dz and 1. The resulting expression is:

$$d\overline{E}_c(t)=\frac{1}{2}(u^2+w^2)dm=\frac{\rho}{2}(u^2+w^2)dxdz \tag{2.62}$$

Integrating along the vertical and averaging with respect to time and length the following expression is obtained

$$\overline{E}_c=\frac{1}{LT}\int_t^{t+T}\int_x^{x+L} d\overline{E}_c\,dxdzdt=\frac{\rho}{2LT}\int_t^{t+T}\int_x^{x+L}(u^2+w^2)\,dxdzdt \tag{2.63}$$

After some mathematical manipulation and trigonometric operations, the final simplified expression of the kinetic energy is obtained:

$$\overline{E}_c=\rho g\frac{a^2}{4} \tag{2.64}$$

At the end, the total energy is obtained by summing the two potential and kinetic contributes:

$$\overline{E}=\overline{E}_c+\overline{E}_p=\frac{1}{8}\rho gH^2 \tag{2.65}$$

It is important to remember that this expression is valid for a unitary horizontal section, that is why it is called energy density. Energy density keeps maintaining a positive quantity due to the fact that it is proportional to squared value H.

Furthermore, it is important to note that energy density is not function of the wave period, but it only depends on its wave height.

2.1.4 Groups of waves

Despite the initial hypothesis, linear wave theory is still applicable with slight variations of the hypothesis themselves by suffering small modifications, such as propagation direction or water depth.
Up to now monochromatic wave has been treated, but they are scarcely found in real seas where even a little portion of sea surface is composed by many different waves, with different characteristics, i.e. different heights, directions, periods and phases.
In order to understand groups of waves and their effects, the application of the principle of superposition is valid within linear wave theory premises. Such principle can be practically written, for n different waves propagating along x direction, as

$$\eta(x,t)=\sum_n \eta_n=\sum_n a_n \sin(k_n x-\omega_n x+\delta_n) \tag{2.66}$$

Wave groups have a particular behavior depending on the characteristics of each wave composing it. The shape of a wave group is determined by its envelope and its celerity is different from the one related to single waves. The group celerity is the velocity in which the energy contained in the group propagates, and determines the envelope variation too.

In the following, some particular cases of two waves interacting are explained.

1) Waves propagating in the same direction and with same period:

- with same phase

$$\eta(x,t)=(a_1+a_2)\sin(kx-\omega t+\delta) \tag{2.67}$$

- with π rad opposed phase

$$\eta(x,t)=(a_1-a_2)\sin(kx-\omega t+\pi) \tag{2.68}$$

2) Waves propagating in the same direction but with different periods:

$$\eta(x,t)=2a[\delta k-\delta\omega t-\delta)\ \sin(kx-\omega t)] \tag{2.69}$$

3) Waves propagating in opposed directions (reflected):

- total reflection: if $a_i = a_r$

$$\eta(x,t)=2a_r \cos(kx) \cos(\omega t) \tag{2.70}$$

4) Minimum and maximum values of free surface elevation:

- minimum

$$|\eta_{min}|=a_i-a_r \tag{2.71}$$

- maximum

$$|\eta_{max}|=a_i+a_r \tag{2.72}$$

In order to find the group celerity, dispersion relation needs to be applied and its final expression can be simplified getting to a different form for each condition of depth.
In shallow or deep water conditions, group celerity assumes the following shape

$$c_g=\frac{c}{2}(1+G) \tag{2.73}$$

where G derives from the dispersion relation and it is written as

$$G=\frac{2kh}{\sinh(2kh)} \tag{2.74}$$

In specific conditions of deep and shallow water, the simplified formulas describing group celerity are respectively

$$c_{g0}=\frac{1}{2}c_0 \tag{2.75}$$

$$c_g=c=\sqrt{gh} \tag{2.76}$$

It is now important to focus on the description of the wave energy propagation through a group of waves.
As already said, to each wave belongs an energy density defined as the sum of a potential and a kinetic component. The problem is now to understand how this

energy propagates in space or its mean value over a period propagating through a fluid vertical section.
Taking into account Figure 2.05, the horizontal force acting on the elements equal to *pdz*. Being that the elementary volume of fluid travel with velocity *u*, it covers the distance *udt* in time *dt*. At the left side of the element, at x=0, the fluid acts with an elementary work written as:

$$dL=pudzdt \tag{2.77}$$

During the same time interval, the fluid volume equal to *udzdt* crosses the vertical element dz. Being that potential and kinetic energy can be written respectively as

$$E_p=\rho gz \tag{2.78}$$

$$E_c=\frac{1}{2}\rho(u^2+w^2) \tag{2.79}$$

the elementary fluid volume *udzdt* travels with energy

$$E=\left[\rho gz+\frac{1}{2}\rho(u^2+w^2)\right]udzdt \tag{2.80}$$

Putting together this energy contributes with the pressure one, it is possible to derive the expression of the instantaneous energy flux crossing the vertical section as

$$E_f(t)=\int_{-h}^{\eta}\left[p+\rho gz+\frac{1}{2}\rho(u^2+w^2)\right]udz \tag{2.81}$$

Remembering that $p^+=p+\rho gz$, after few mathematical passages it is possible to get to the expression of
the energy flux related to a wave group, which is given by the energy of the wave multiplied by the group celerity:

$$\overline{E}_f=c_g\overline{E}=\frac{1}{16}\rho gH^2c\left[1+\frac{2kh}{\sinh(2kh)}\right] \tag{2.82}$$

This result shows that energy transport exists along the propagation direction and its mean value for unit of width is called *mean energy flux*, which represents the product between group celerity and specific energy.

Thus, it is possible to conclude that energy propagates with group celerity when talking about linear waves.

2.1.5 Transformation of waves entering shallow water

When approaching the shoreline, in the area called surf or near-shore, the seabed starts having a significant influence in the wave behavior. The first wave response at the presence of seabed is called shoaling. When the wave reaches that area, it has gradually less space to propagate while the energy remains constant, as in linear wave theory there is no energy loss until wave breaking, where the theory is no longer valid. As a result, an initial smooth decrease in wave height happens to give place to a sudden substantial increase of the wave height as the bottom keeps getting closer, as it is possible to see in Figure 2.06. The shoaling development is represented by the shoaling coefficient KS:

$$K_S = \frac{H}{H_0} = \sqrt{\frac{c_0}{2c_g}} = \frac{1}{\sqrt{\tanh(kh)(1+G)}} \tag{2.83}$$

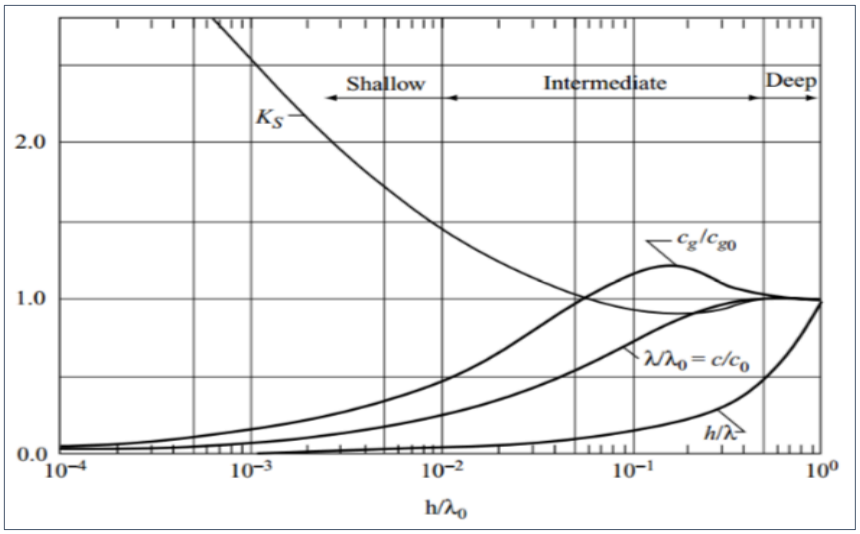

Figure 2.06 Shoaling coefficient K_S trend vs the ratio between water depth and wave length [5].

The offshore direction of propagation of waves is not always perpendicular to coastal line; however, when breaking, waves have turn and oriented perpendicularly to the coast. This phenomenon is called refraction and follows Snell law, developed for light waves but also valid for sea waves, which delivers the refraction coefficient Kr (2.84). Figure 2.07 shows a geometric representation of the Snell's law applied in the near-shore area, determining the wave front width used to compute the refraction coefficient in the following way:

$$K_r = \sqrt{\frac{L_1}{L_2}} \tag{2.84}$$

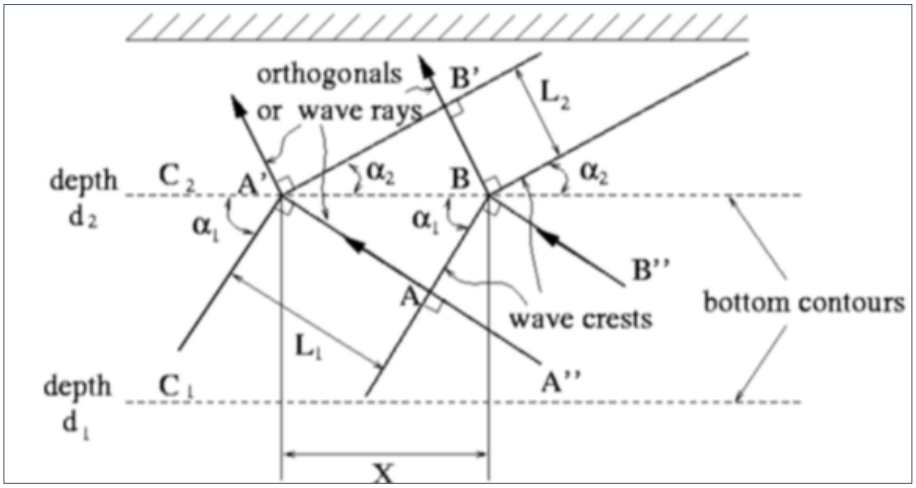

Figure 2.07 Geometric representation for Snell's law.

Depending on the coastline shape, the wave height can increase or decrease when refracted, i.e. if the coast is a bay (concave form) waves will tend to spread into a wider area and therefore, their height will decrease. On the contrary, if the coast is a cape (convex form) the waves will tend to concentrate towards the tip of the cape and their height will grow. The height in this case is computed by combining both coefficients, the shoaling and the refraction coefficient:

$$K_r K_s = \frac{H}{H_0} = \sqrt{\frac{c_0}{2c_g}}\sqrt{\frac{L_1}{L_2}} \tag{2.85}$$

2.1.6 Wave diffraction

Another important phenomenon from the engineering point of view is represented by wave diffraction. Diffraction occurs every time an obstacle is encountered by the wave at the mean sea level and its dimensions are smaller or equal to the incident wave length. So, diffraction means a change in the sea surface due to the presence of the obstacle, which diverts the wave from its natural direction of propagation. Besides, diffraction rarely comes on its own. In facts, it is always linked to other phenomena, for example wave reflection. At the end, diffraction will occur depending on the obstacle size; if this is bigger than one order of magnitude less than the wavelength will take place, if the obstacle is smaller, the wave has enough energy to overcome it without particularly feeling its presence.

From practical point of view, the simplest case is the one representing flat bottom and obstacle with vertical walls coming out from the mean sea level. Concerning these conditions, the diffraction issue is described by the Helmholtz equation, an adaptation of the Laplace equation:

$$\phi(x,y,z,t)=\Im f(z)\Phi(x,y)e^{-ti\omega} \tag{2.86}$$

$$\eta(x,y,z,t)=\Re H(x,y)e^{-ti\omega} \tag{2.87}$$

where

$$f(z)=\frac{\cosh[k(h+z)]}{\cosh(kH)} \tag{2.88}$$

After some mathematical operations and simplifications, the Helmholtz version of the Laplace equation results:

$$\frac{\partial^2\Phi}{\partial x^2}+\frac{\partial^2\Phi}{\partial y^2}+k^2\Phi=0 \tag{2.89}$$

This is an elliptic equation and it has been proved to be valid for the following situations:

- Straight hurdle of semi-infinite length;
- Finite gap in an infinite length straight hurdle;
- Isolated obstacle made of a straight hurdle of finite length;
- Isolated obstacle which horizontal section is circular.

Diffraction is an important element that has to be considered in the design and representations of wave energy converters and in general in every problem concerning fluid structure interaction, depending on the dimensions of the incident waves and of course the structure itself. This problem will be better discussed in paragraph 2.2 while describing the importance of diffraction in the particular case treated in this thesis.

2.2 Fluid-structure interaction

Fluid-structure interaction is a very important subject for this thesis development as the principal aim is to represent, in the best way possible, the cylindrical buoy dynamics when subjected to regular waves. In this section wave-structure

interaction will be explained describing all the forces acting in this kind of situation.

Before the description of the acting forces it is very important, when talking about floating structures dynamics, to define a reference coordinate framework upon which all variables will be based. The most widely used reference system is the Cartesian one, in which three axis x, y and z are defined. For simplicity, the centre of the coordinate system is usually set at the centre of gravity (CoG) of the studied structure or at the Mean Water Level (MWL). Each axis is orthogonal to the other, defining the normal vector of three planes that describe the three-dimensional space. A free-moving body has six DoFs, three of them describing the translations and the other three, the rotations. Therefore, in mathematical formulae the subscripts $1-3$ are linked to the translations and $4-6$ to the rotations. Modes 1, 2 and 4, 5 are ambiguous, especially if the structure is axisymmetric with respect to the z axis and therefore they may be interchanged. However, common praxis is to remove this ambiguity when there is an incident wave; orienting the structure so as to make the wave propagation direction coincide with the x-axis of the structure, see Figure 2.08. In marine structures, each DoF is associated to a particular name, as reported in table 2.08, [8].

Mode	Component	Mode Name
1	$u_1 = U_x$	Surge
2	$u_2 = U_y$	Sway
3	$u_3 = U_z$	Heave
4	$u_4 = \Omega_x$	Roll
5	$u_5 = \Omega_y$	Pitch
6	$u_6 = \Omega_z$	Yaw

Table 2.01 Degrees of Freedom (DoFs) for a floating body.

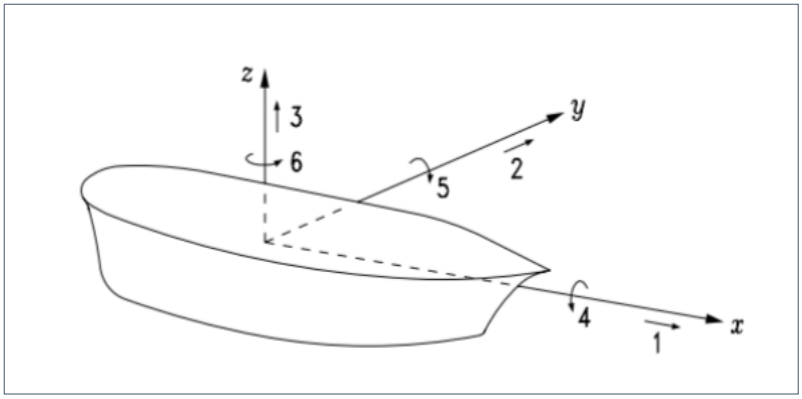

Figure 2.08 DoFs reference system convention for a floating body [26].

For what forces are concerned, first of all it is important to notice that rigid body dynamics is governed by Newton's second law:

$$\sum \vec{F} = m\vec{a} \tag{2.90}$$

where $\vec{F}=F_1,F_2,F_3,F_4,F_5,F_6 \equiv F_x,F_y,F_z,M_x,M_y,M_z$ is the force vector for each DoF, m is the mass matrix of the body, in which the first three components of the diagonal are the mass of the body and the last three are the moments of inertia and $\vec{a}=a_1,a_2,a_3,a_4,a_5,a_6$ is the acceleration vector of the body for each DoF.
When it comes to floating bodies, $\sum \vec{F}$ is decomposed into two main kinds of forces exerted by the incident wave, in particular hydrodynamic force $\vec{F}_{hd}$ and hydrostatic force $\vec{F}_{hs}$:

$$\sum \vec{F} = \vec{F}_{hd} + \vec{F}_{hs} \tag{2.91}$$

For what hydrodynamic force is concerned, it can be seen as the integral of hydrodynamic pressure over the wet surface of the body. So, considering the i^{th} DoF and referring to Figure 2.09, the general expression of hydrodynamic force can be written as

$$F_i = -\iint_S pn_i \, dS \tag{2.92}$$

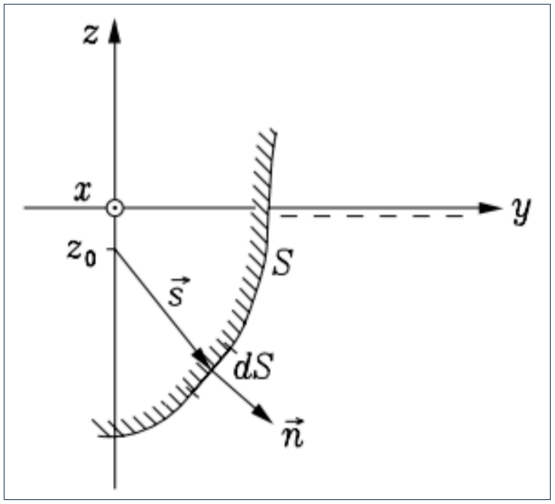

Figure 2.09 Normal to the body surface, direction through which pressure is integrated along the body surface [8].

In terms of complex amplitudes, through the imposition of the relation p=-iωρ$\hat{\phi}$ for a given potential $\hat{\phi}$:

$$F_i = i\omega\rho \iint_S \widehat{phi}\, n_i \, dS \tag{2.93}$$

However, hydrodynamic force is the sum of three different sub forces:

- Excitation force $\vec{F}_{exc}$;
- Radiation damping force $\vec{F}_r$;
- Drag force $\vec{F}_{drag}$;

$$\vec{F}_{hd} = \vec{F}_{exc} + \vec{F}_r + \vec{F}_{drag} \tag{2.94}$$

Excitation force $\vec{F}_{exc}$ is the contribute related to the incident wave considering the body fixed, so a potential that is due to the incoming wave only has to be taken into account. Nevertheless, excitation force is the resultant of two other contributes: Froude-Krylov force which represents the integral of the hydrodynamic pressure on the wet body surface (with potential $\hat{\phi}_0$), and the diffraction force which is due to the diffracted wave field that forms when the wave touches the body surface (with potential $\hat{\phi}_d$).

Substituting into the general form, it is possible to derive the expression for excitation force as

$$F_{exc,i} = i\omega\rho \iint_S \left(\hat{\phi}_0+\hat{\phi}_d\right)n_i dS \tag{2.95}$$

In particular, diffracted wave field is created when the boundary conditions for the wet surface is not satisfied and thus the following relation becomes valid:

$$-\frac{\partial\hat{\phi}_d}{\partial x} = \frac{\partial\hat{\phi}_0}{\partial x} \quad \text{on S} \tag{2.96}$$

Diffraction force can sometimes be neglected if compared to the other acting forces. The cases in which this is possible depends both on the incident wave and body dimensions: in particular the relationship is described on the Koulegan-Carpenter number (KC), [10, 37]. KC is a dimensionless quantity representing the ratio between drag forces and inertia forces, and it is computed as

$$KC = \frac{2\pi A}{L} \tag{2.97}$$

where:

- A represents the incident wave amplitude;
- L stands for the characteristic dimension of the body.

If $KC > 10$ the body can be considered small and drag forces are dominant with respect to diffraction forces, while when $KC \leq 2$ no appreciable flow separation happens and viscous effects are confined to the boundary layer. In case of $KC < 10$ the ratio between a significant body dimension and the wave length l/λ has to be taken into account: if $l/\lambda \ll 1$ diffraction can be neglected, while if $l/\lambda \gg 1/5$ diffraction must be considered.

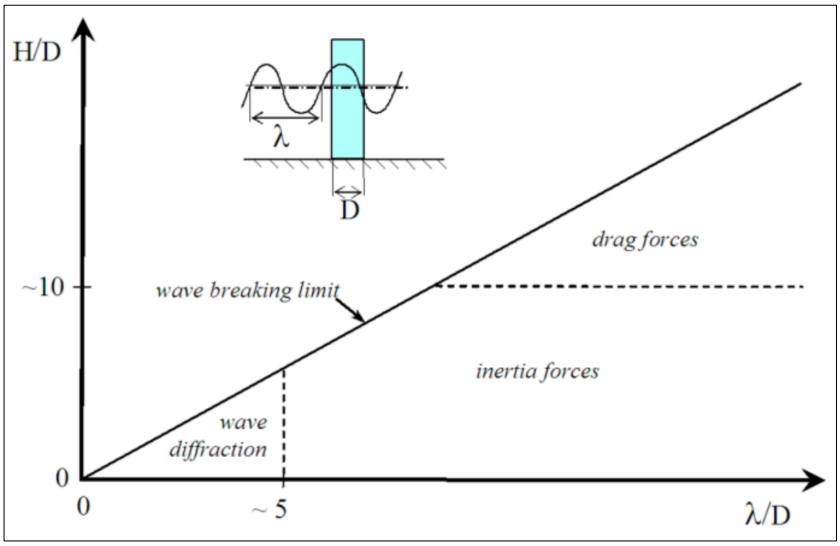

Figure 2.10 Acting forces and their influence domains with respect to H/D and λ/D ratios [11].

Radiation force is the contribute related to the radiation phenomena. In particular, considering a flat free surface, hence setting the incident wave potential equal to zero, but a moving body. While moving, the body produces waves as the result of the displacing of water around its external surface. This produced waves are radiated waves and this phenomenon is called radiation. As well as diffracted waves, radiated ones present a fundamental difference compared with incident wave. An incident wave is a plane wave propagating in only one direction, whereas a diffracted/radiated wave propagates in every direction from the source point (i.e. the oscillating body). In particular, it means that one effect of the wave-structure interaction is to redistribute part of the incident energy, which had been propagating in a single direction, along all other directions. Therefore, the overall wave field is perturbed everywhere around the structure, and not only at the wake of the body, as explained in [29]. The phenomenon is graphically shown in Figure 2.10.

Of course, radiated waves exert a reaction force on the body surface, the so-called radiation force. Radiation potential has to be introduce as $\hat{\phi}_r$ and the force it produces can be written as

$$F_{e,i} = i\omega\rho \int\int_S \hat{\phi}_r \, n_i dS \tag{2.98}$$

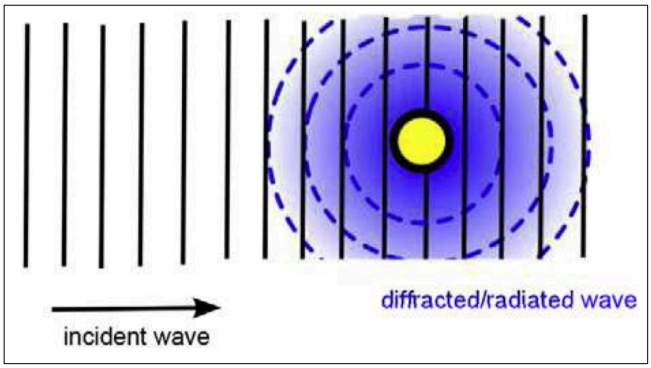

Figure 2.11 Wave pattern around an oscillating body subjected to an incident wave field [30].

Drag force consists of two components too: the surface frictional drag and wake pressure drag. The overall effect that the drag force induces to the body is extremely complicated, to such extent that is still not fully understood. Empirical analysis however, have brought to a formula which is still the widely used to the present date:

$$F_d = \frac{1}{2}\rho C_d A_d u^2 \tag{2.99}$$

where A_d is the area of the wet part of the body projected onto the normal plane of the velocity, Cd is the drag coefficient, which mainly depends on the shape of the body, the roughness of the surface, the KC number and on the Reynolds number (Re). Finally, u is the relative velocity between the body and the fluid flow, considering that in equation (2.99) flow is assumed to be steady. Nonetheless, in the presence of waves the flow cannot be assumed steady as it varies harmonically, the adapted expression for the drag force under the presence of waves is

$$F_d = \frac{1}{2}\rho C_d A_d \, |u| \, u \tag{2.100}$$

The absolute value allows predict the oscillatory behavior of waves by taking into account the sign of the velocity. For simple body shape, C_d can be found tabulated in literature deriving physical experiments. For more complex shapes however; on the one hand, ad-hoc experimental tests need to be carried out in order to determine such parameter; on the other hand, the fast growing computation capacity has led to the irruption of a new tool, the CFD which allow to perform simulations in order to determine the C_d parameter in a much more efficient way, either in terms of cost and times.

Finally, the last force to be determined is the hydrostatic force, caused by the hydrostatic pressure and first postulated by Archimedes. Back in the ancient Greek

times, the Philosopher theorized the following principle: A body placed in a liquid loses and amount of weight equal to the weight of the liquid that it displaces. Following this observation, the equation of hydrostatics can be derived. Considering a partially submerged body, which displaces a volume V of water. Consider also W the total weight of the body, A its cross-sectional area and d its draft. Then, following the Archimede's principle one can write

$$W = \gamma V = (\rho g)Ad \tag{2.101}$$

Where γ is the weight density of the liquid, water in this case. As W is a force, the hydrostatic pressure acting on the bottom of the body can be assumed to $p = -\rho gd$. From its equilibrium position, assume the body be given a small downwards vertical displacement $-\delta z$. From the Archimede's theorem the new equilibrium position results in the following equation:

$$\gamma(\delta V) = -\rho g(\delta z)A = \delta pA \tag{2.102}$$

This variation from the equilibrium, in this example in the vertical axis, causes then a restoring force that tends to bring the body back to its initial equilibrium position. The restoring force, also known as buoyancy force in a more general form is given by the following expression:

$$F_b = -W = (\rho gV)\vec{k} \tag{2.103}$$

Where $\vec{k}$ is the versor of the vertical direction in the orientation of the body.

3

Experimental tests

The experimental part of this thesis has been carried out at the Laboratory of Hydraulic Engineering (LIDR) of Alma Mater Studiorum University of Bologna. In this section, laboratory setup is going to be presented, describing dimensions and characteristics of the cylindrical buoy, of the channel and the initial position of the buoy in comparison with the free surface. Furthermore, wave generation and the measurements of the dynamics of the modelled floating body will be explained.

3.1 Laboratory set-up

Waves are generated by a wave generator positioned at the beginning of the channel. At the end of the channel a wave absorber panel is installed in order to avoid wave reflection which would disturb the experiment reflecting incoming waves, subsequently modifying free surface. The latter is made of structured fill obtained from the assembly of plastic sheets.
The floating body is located at the centre of the flume. The buoy is a cylindrical and slender object made of plastic and lead. While most of the cave structure of the buoy is made of plastic, a lead block is placed at the bottom of the body in order to shift down the centre of mass and allowing the buoy to maintain a vertical configuration while floating.
A mooring system made up of four metal chains of negligible weight is installed with the aim of keeping the buoy around its reference position and avoiding excessive shifts due to the action of the incident waves. Furthermore, as general characteristics of mooring systems, it should control the directional heading of the body it is linked to, when the orientation is important for safety or operational considerations, and, at the end, limiting other motion characteristics as the acceleration of the body. These characteristics of catenaries and other kinds of mooring system are widely described by [27].
This kind of mooring system has a large footprint and the anchor point should be subjected to horizontal forces only. The catenaries are hooked to the buoy

through a plastic crown placed 20 cm below the upper surface of the buoy itself, and anchored at the bottom at the edges of a rectangular platform placed at the bottom of the channel, as shown in Figure 3.04.
In the latter, geometric dimensions of the cylindrical buoy are shown too, with the indication of the centers of mass of the single parts and of the total rigid body, computed as a weighted average, [9]. The characteristics and dimensions of the whole laboratory set-up are reported in Table 3.01.
A recording system made of seven gauges (represented in green) is distributed all along the channel as to register the free surface perturbations during the simulations.
Furthermore, two GoPro cameras (represented in red) are installed in order to record buoy movements from lateral and top points of view respectively. Thanks to the cameras used, the motion of the cylindrical buoy was analyzed, after a video processing which is described in paragraph 3.3.1.

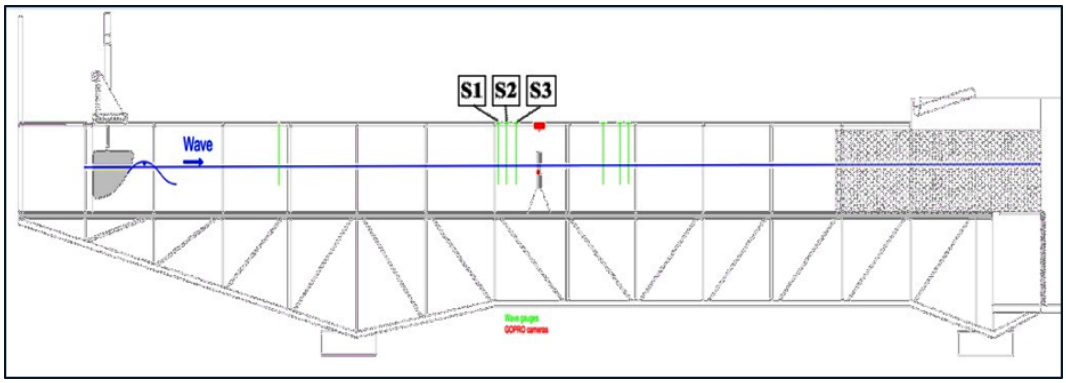

Figure 3.01 Horizontal section of the laboratory channel.

Figure 3.02 Photo of the laboratory set-up.

FLUME		
Length	15.00	m
Width	0.50	m
Height	0.70	m
Water depth	0.40	m
Material	plexiglass	
CYLINDRICAL BUOY		
Height [H]	0.355	m
Diameter [D]	0.050	m
Total Mass	0.601	Kg
Plastic Mass	0.188	Kg
Lead Mass	0.413	Kg
MOORING SYSTEM		
n. of chains	4	-
Chain length	0.35	m
Material	steel	-

Table 3.01 Laboratory set-up characteristics and simulation wave parameters.

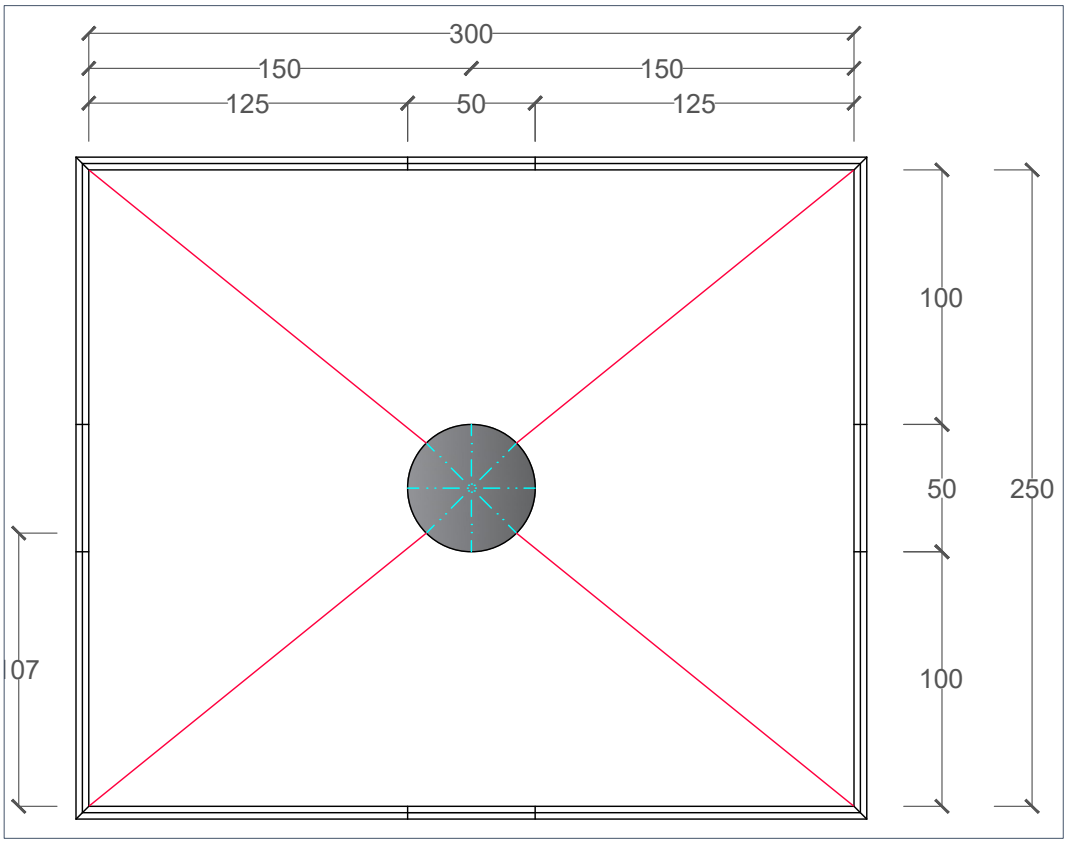

Figure 3.03 Dimensions of the buoy section and mooring system injection, top view (measures in mm).

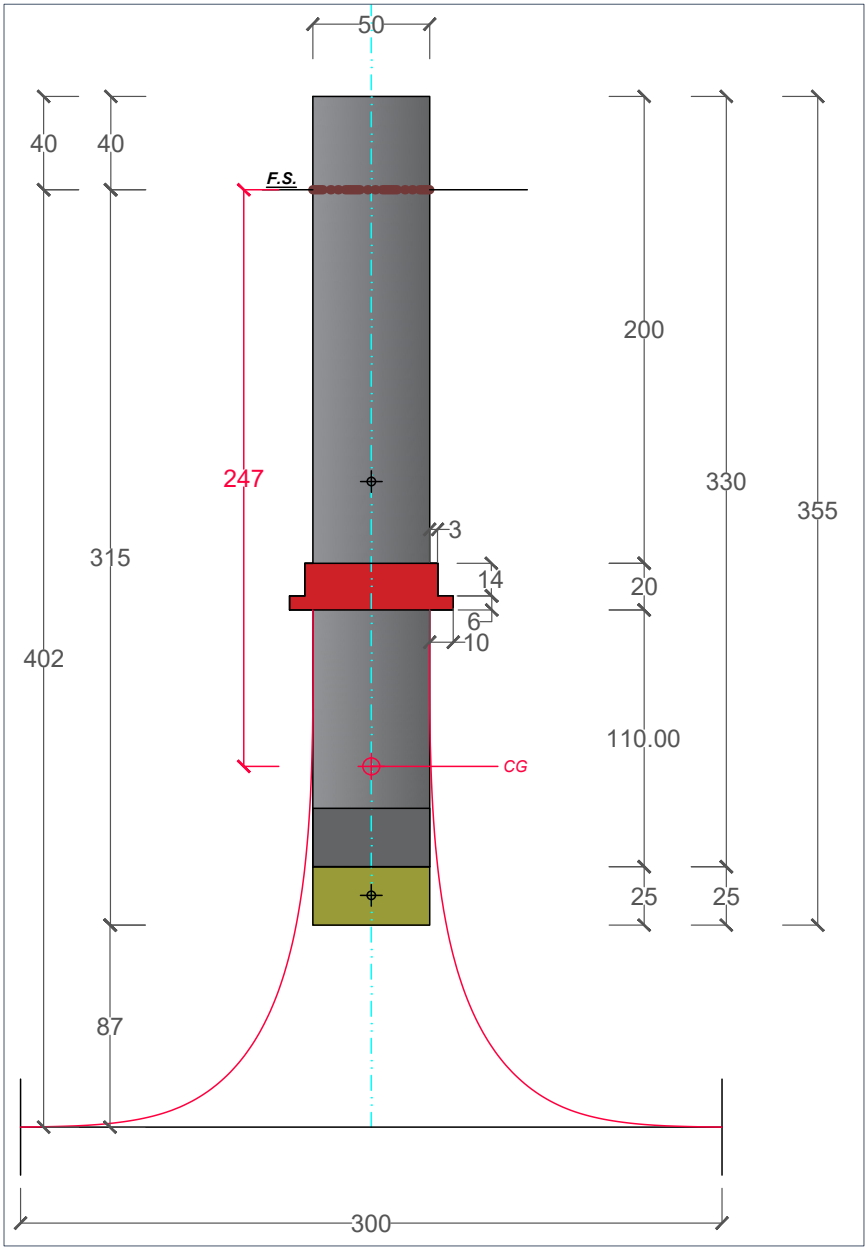

Figure 3.04 Lateral section of the buoy at its balance position (measures in mm).

3.1.1 Experimental tests

Before the experimental test starts, the free surface is flat and hence the buoy takes its balance position, which is described in Figure 3.04. Experimental part is then carried out by a free decay test and then switching on the wave generator which perturbs free surface generating waves of different height and length. By doing so, it is possible to generate both regular and irregular waves, nevertheless in this thesis only regular waves are taken into account. Several experiments with different wave

height and period conditions have been conducted and are catalogued in table 3.02 in order to resume the characteristics related to each wave. During each test event both wave heights and buoy motion are recorded at each instant, respectively through the gauge recording system and the GoPro cameras.

FREE DECAY (heave)		
Initial condition	-40	mm
Wave height [H]	0	mm
WAVE R03		
Height [H]	6.91	mm
Period [T]	0.72	s
Wave length [λ]	800	mm
WAVE R04		
Height [H]	8.23	mm
Period [T]	0.77	s
Wave length [λ]	900	mm
WAVE R05		
Height [H]	8.61	mm
Period [T]	0.82	s
Wave length [λ]	1000	mm
WAVE R06		
Height [H]	10.27	mm
Period [T]	0.85	s
Wave length [λ]	1100	mm
WAVE R07		
Height [H]	10.44	mm
Period [T]	0.90	s
Wave length [λ]	1200	mm
WAVE R08		
Height [H]	11.23	mm
Period [T]	0.94	s
Wave length [λ]	1300	mm
WAVE R10		
Height [H]	33.50	mm
Period [T]	0.93	s
Wave length [λ]	1300	mm

Table 3.02 Laboratory tests parameters.

3.1.2 Gauge recording system

The experimental record apparatus consists of seven gauges which reconstruct generated and diffracted waves during the tests, respectively previously and at the wake of the body. One gauge is positioned at the beginning of the channel, immediately after the generator, in order to reconstruct the generated wave profile, while the remaining six gauges are installed around the object. In particular, three gauges are placed before the buoy as to reconstruct the exact wave which hits the buoy itself, while the others are positioned at the wake of the body to understand how the latter modifies free surface level after waves have hit it. The positions of the gauges are reported in Figure 3.01.
Being the gauges electrical devices, they detect voltage associated with wave elevation at a certain time, so they finally return a vector of voltages related to a one of time instants with regular time step of 0.001s for the entire experiment. Then, thanks to the calibration performed before each test day, voltage series have been converted into wave height series in order to be able to describe the free surface motion. This also represents the needed data to be put into the mathematical model. Examples of the free surface perturbation signal are reported in Figure 3.05 and Figure 3.06, relatively to R05 wave case.
Among the seven gauges distributed along the channel, the motion described by S3 has been taken into account, as it is the nearest gauge to the buoy and hence the one which best captures the perturbation occurring to the buoy itself during tests. Data coming from this gauge will be use as input to the mathematical model as incident wave height.

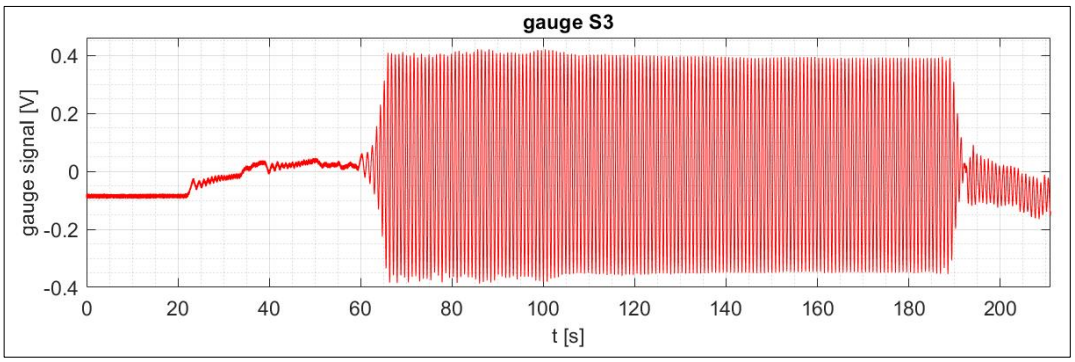

Figure 3.05 Voltage as recorded by the S3 gauge during wave test R05.

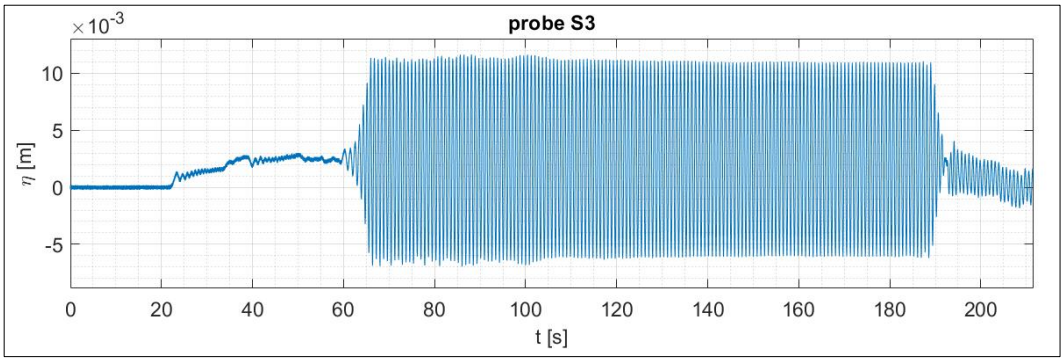

Figure 3.06 Free surface expressed in meters, wave test R05.

It is possible to see, after the wave generator starts working, quite a regular free surface oscillation. This is first due to the fact that the wave generator has been programmed in order to produce waves which are as much regular as possible, that is the reason why in the central part of the plot a sinusoidal form is almost taken by the free surface. Second reason is linked to the presence of the absorber positioned at the end of the channel, which is able to avoid wave reflection nearly completely, in order to maintain a regular wave profile along the channel. For these reasons, every consideration about free surface and every derivation are made considering linear regular waves.
The three gauges positioned at the wake of the cylinder are aimed at capturing how the buoy is capable of deforming the free surface from that point onward. Despite the presence of these three gauges, they are not taken into account due to the fact that the study of the free surface variation at the wake of the body goes beyond the purposes of this thesis work. Furthermore, waves considered are long enough to be able to neglect any diffraction effect.
The last assumptions will be better explained in chapter 4, where the entire hypothesis and considerations list referred to the case studied is presented.

A calibration process has been performed on the gauges in order to transform voltage signals in meters. The result is represented in Figure 3.06, where the example of wave R05 is shown.

3.3 Laboratory tests analysis

3.3.1 Video analysis for body dynamics

With the two GoPro cameras, videos at lateral and top view have been recorded during laboratory tests. These videos are analysed in order to record all the positions occupied by a point of the buoy during the test time, and to be able to plot the buoy motion along the interested DoFs for all the generated sea states. At the end, it will be possible to compare these laboratory results with the model ones.
A Matlab routine for video analysis has been created and applied to each video. First, a calibration process has been performed: a chessboard with known square dimensions has been positioned inside the channel in (at least) five different positions and photographed by the cameras. Then, the calibration procedure has been applied through a Matlab routine, in which, a metrical unit has been associated to the single pixel of the image. This is an important part of the video analysis, which allows to compute the real oscillation of the buoy in meters.
Before starting the main routine, all the videos have been modified by the use of the GoPro Studio program, a dedicated GoPro application useful in order to modify some video characteristics. In particular, the cameras recorded at almost 30 fps (frame per second), a very high number of frames. So, with GoPro Studio, the number of fps has been lowered to 15 fps: this allows to reduce videos dimensions, working in an easier and faster way, but still maintaining quite a good enough resolution.
Then, the videos have been analysed through the introduced Matlab routine. First, the 15 fps video is loaded in Matlab, then, each frame is cut in order to deal with a much less heavy document, keeping inside the cylinder and the space needed to see it moving during the test only. Furthermore, the video is converted in RGB format: this is an important step, as it is useful to associate an RGB colour scale to each pixel of the frames. At this point, two particular points have to be chosen inside the domain described by the cylinder. The choice of these points is crucial for the description of the buoy motion during laboratory tests: the first one has to represents surge and heave motions of the cylinder during tests, while the second one is needed in order to determine pitch motion. So, for what the first point is concerned, it has to coincide with the centre of rotation of the buoy as not to influence surge and heave translations through any contribution coming from rotations. This point practically coincides with the centre of mass detected in Figure 3.04. Concerning the second one, it has to belong to the same axis that crosses the first point and maintaining the same distance from the latter, for all the duration of the tests.
Points individuation practically consists in isolating a zone to which the point belongs, picking the pixel associated to a particular span of RGB colour values and

then finding the position of their centre by performing the computation of the mean of both vertical and horizontal coordinates of the whole picked points. Their centre has to coincide with the desired point.

A point very close to the real centre of rotation has been picked and tracked as Figure 3.07 and Figure 3.08 show, and where points 1 and 2 are represented. The same way of picking and tracking the two points is applied to all the videos of the laboratory tests. As already introduced, tracking point 1 is useful in order to catch both surge and heave motions of the cylinder, while, for what point 2 is concerned, only its surge motion is necessary. In fact, being the cylinder a solid body, the distance between point 1 and 2 does not change during the test and once distance itself and the horizontal motion of both points are determined, pitch rotation is derived by applying some easy trigonometric calculation.

The accuracy and the precision of this kind of procedure depends on the quality of the points that one is able to select and isolate, and of course, on the image quality that each frame is capable of offering. In fact, a very good isolation and determination of the point to track in one frame could not be so good in the following frames: it is possible that color indices slightly vary along with the studied frame. This process characteristic brings to the fact that some noise arises in the data signal and it tends to be higher when the buoy motion is lower. This is the case of the heave motion for wave R03: the wave height is small, and it forces the cylindrical buoy to a very small oscillation in the vertical direction which keeps lower than a millimeter, and the noise becomes a very important and visible phenomenon.

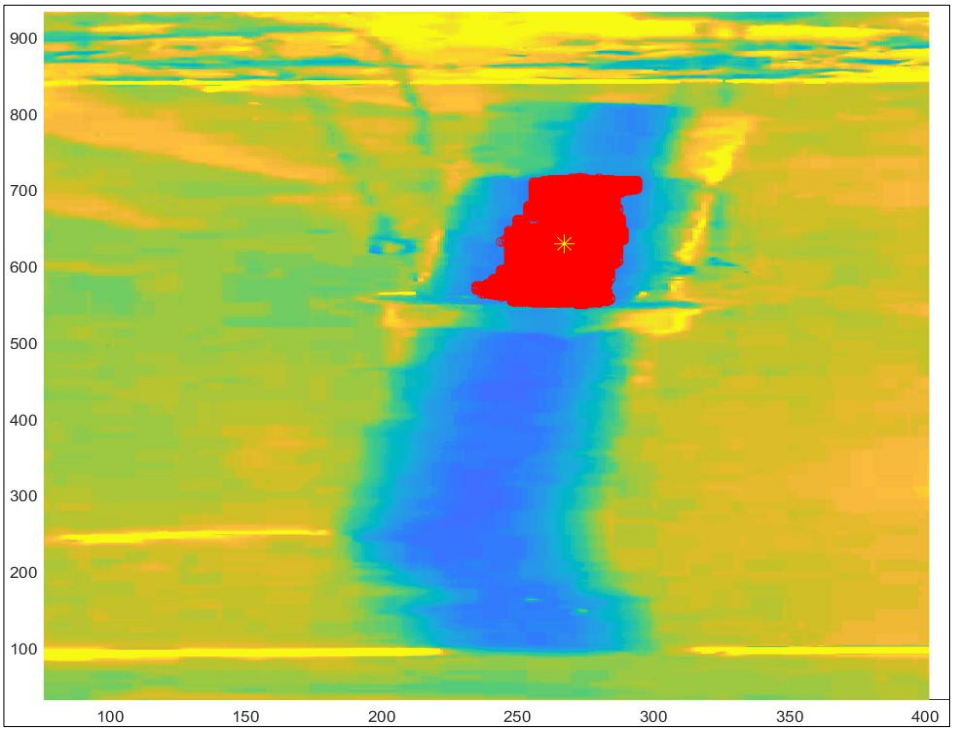

Figure 3.07 Example of video analysis of wave R07. The red area gathers all the points whose centre of gravity is represented in yellow by point 1. The latter is used for surge and heave motions tracking.

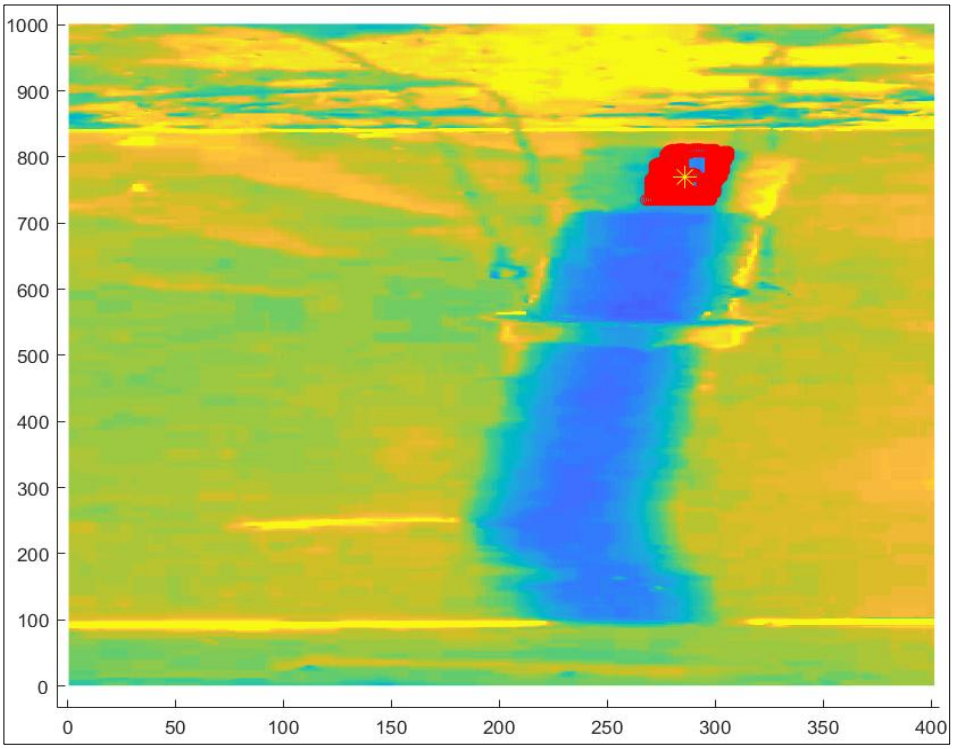

Figure 3.08 Example of video analysis of wave R07: The red area gathers all the points whose centre of gravity is represented in yellow by point 2. The latter, together with point 1, is used for pitch motion tracking.

3.3.2 Analysis of the generated waves

As already introduced in section 3.1, waves are generated by a wave generator, positioned at the beginning of the channel. Each generated regular sea state has been recorded by 7 gauges placed at different sections of the channel itself. The most important and considered one in the development of this thesis is the signal recorded by gauge S3, positioned immediately previously the buoy, as to catch the characteristics of the wave that actually impacts the body in the best way possible. In this section, only the group of waves recorded by the gauge S3 are going to be shown.

Once signals expressed as voltages have been converted into wave heights representing the free surface perturbation that spreads during the laboratory test time, it is possible to plot them. While the seven waves characteristics are expressed in table 3.01, their plots are shown in following Figures 3.07 to 3.13.
The plots show how the surface perturbation produced by the generator is not perfectly regular, but it is still possible to catch small irregularities among the same wave. There are little irregularities for what high frequencies are concerned: higher is the wave height, more likely is this phenomenon occurrence, which is visible in the form of a small perturbation of the waves envelop. Cases R07, R08 and R10 are representative of the latter situation. This phenomenon is due to the not perfect wave absorption provided by the wave absorber that makes wave reflection not completely deleted inside the channel. Furthermore, as the most intense high frequency perturbation is related to the first seconds of test, it is also likely to be due to the free surface displacement from the previous performed tests.

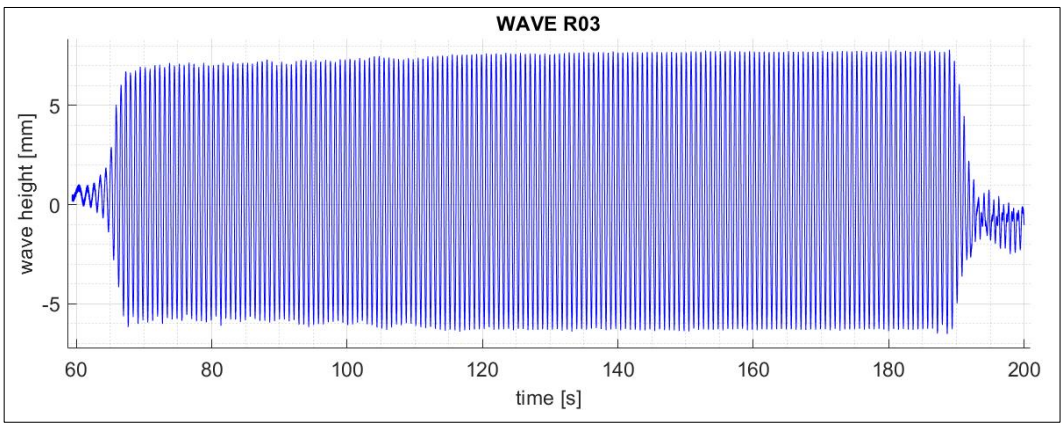

Figure 3.09 Free-surface for wave R03 during the test time.

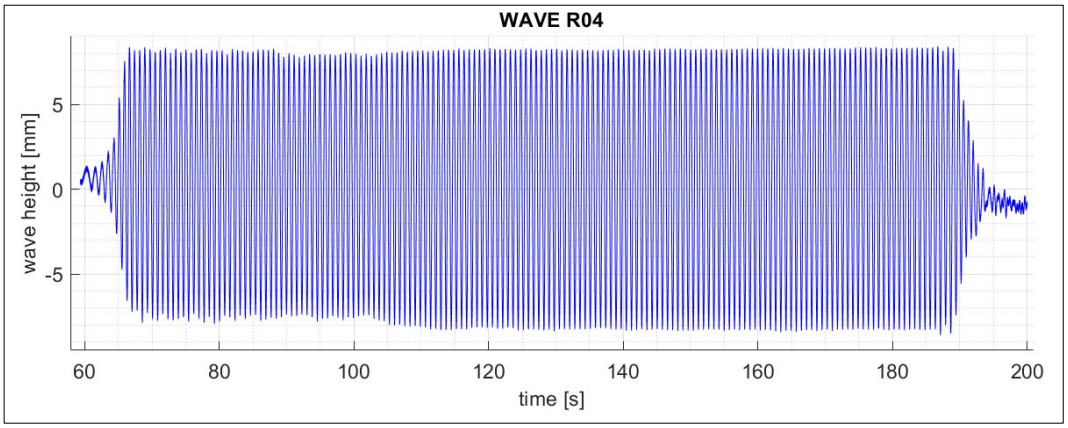

Figure 3.10 Free-surface for wave R04 during the test time.

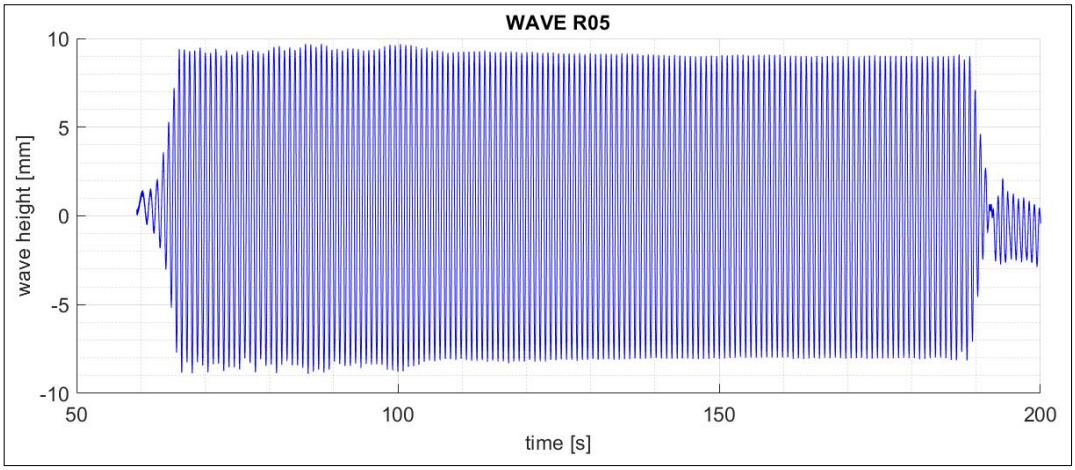

Figure 3.11 Free-surface for wave R05 during the test time.

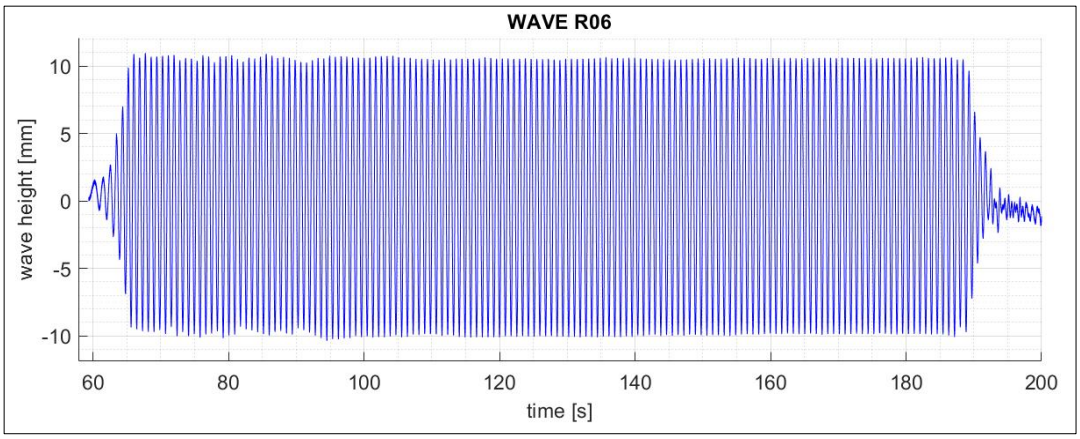

Figure 3.12 Free-surface for wave R05 during the test time.

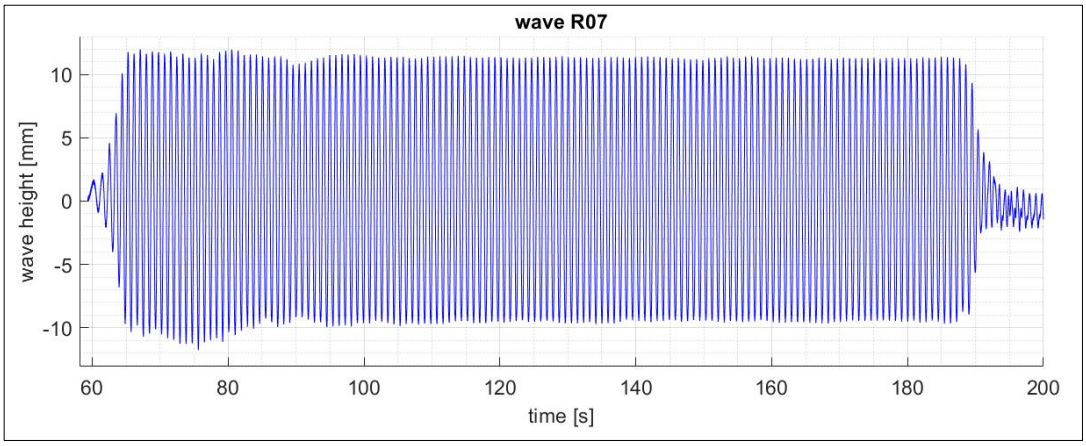

Figure 3.13 Free-surface for wave R06 during the test time.

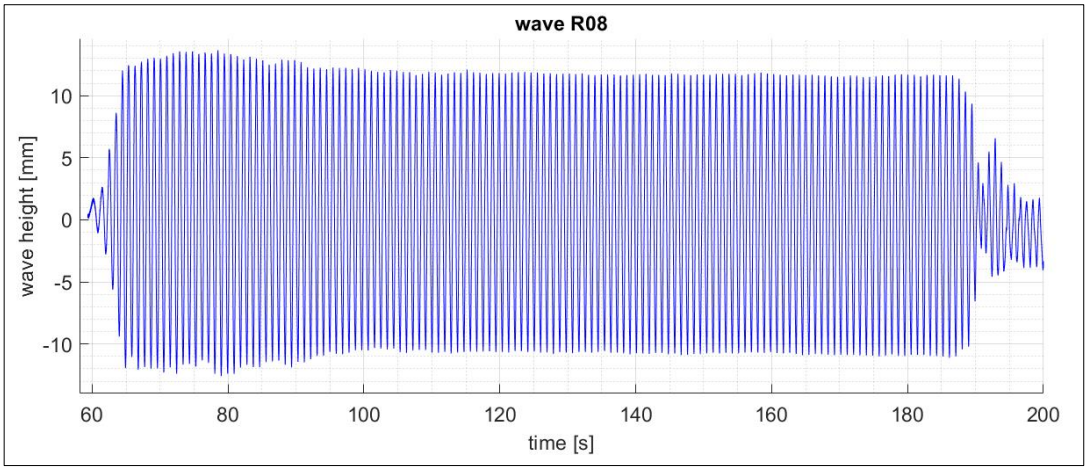

Figure 3.14 Free-surface for wave R07 during the test time.

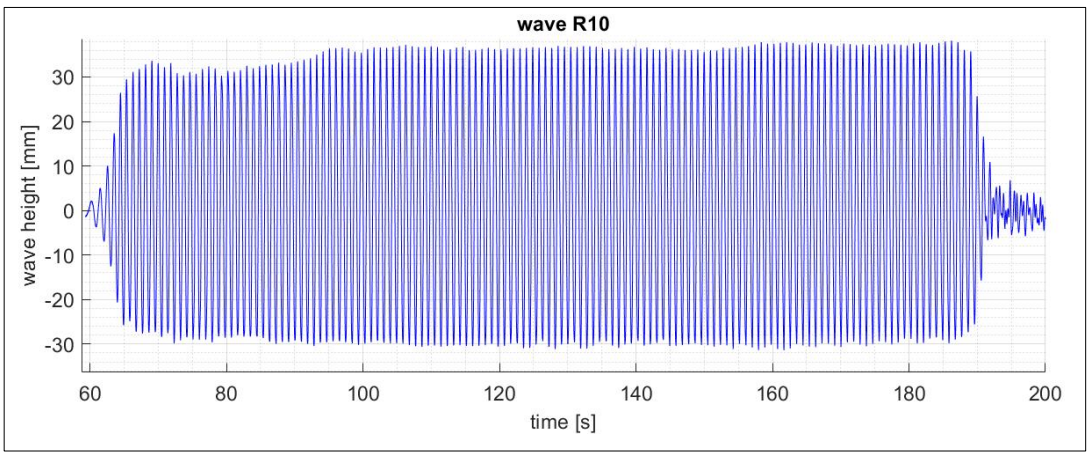

Figure 3.15 Free-surface for wave R10 during the test time.

Wave frequency is a very important characteristic when it comes to the development of the model as it will be accurately explained in chapter 4, where the whole mathematical model is described. Hence, a frequency analysis of the wave signal has been performed in order to define waves frequency in a precise way. Fourier transformed function has been applied to the recorded signals, passing from their description in time domain to the frequency one. This passage has been performed through the use of the Matlab function Fast Fourier Transformed (fft), whose application will be better reported in section 4.6 when talking about the procedure of frequency analysis on the model and laboratory results. It follows a plot gathering all the wave signals in frequency domain.

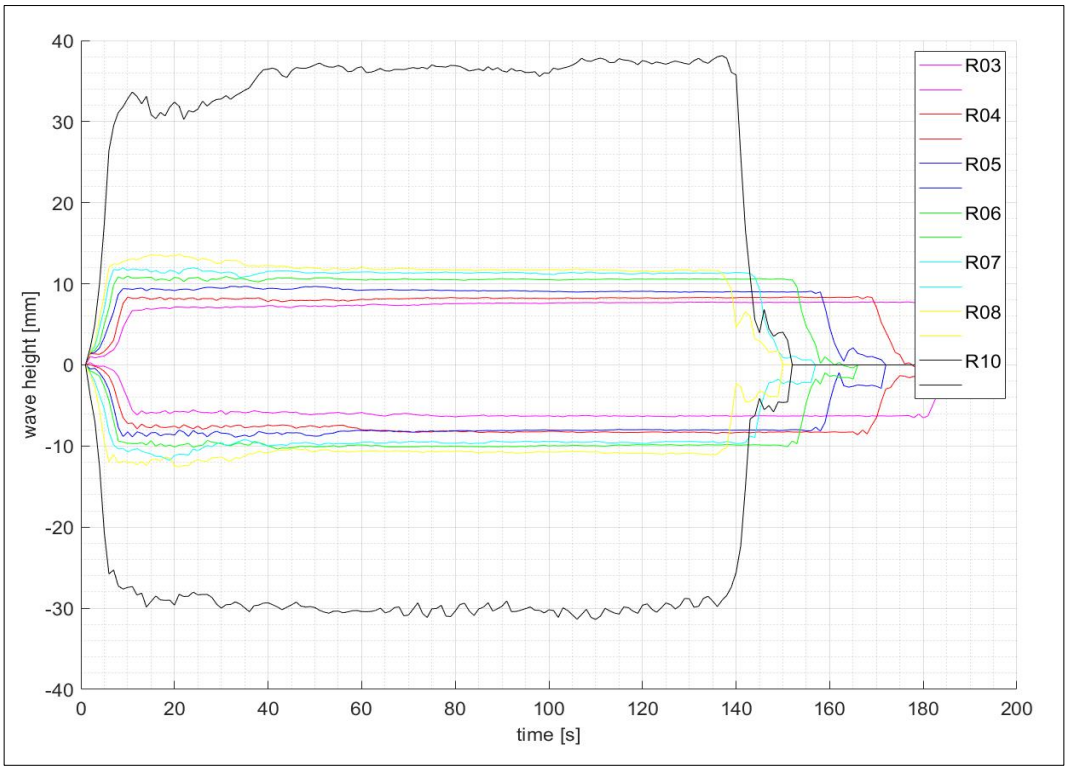

Figure 3.16 Envelops of the waves during experimental test time.

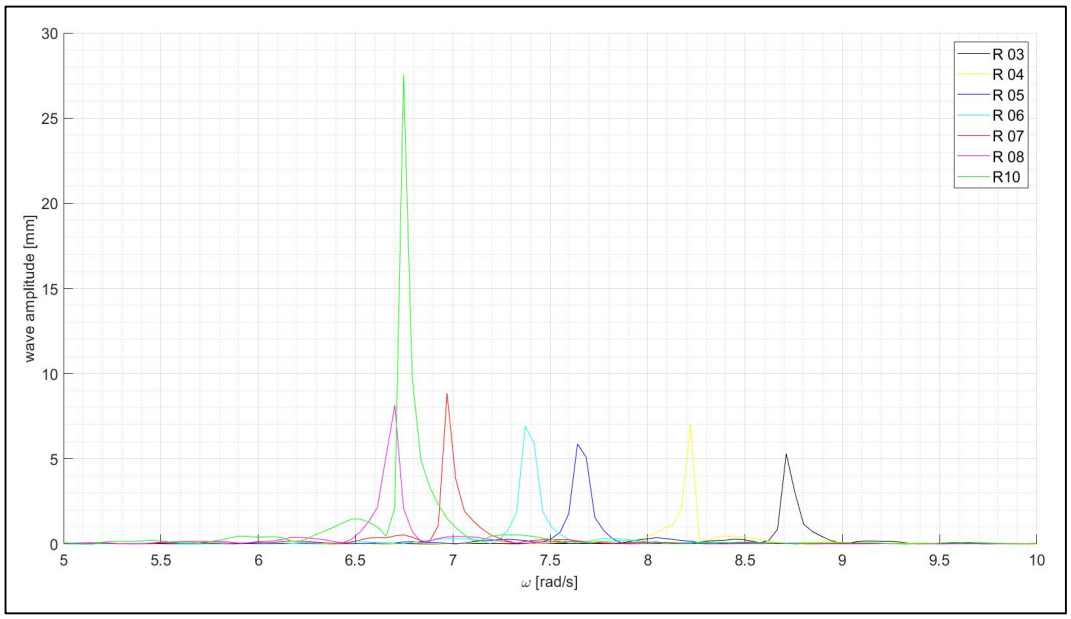

Figure 3.17 Waves signal in frequency domain.

The frequencies of the seven wave signals are then summarized in the following table:

WAVE	ω [rad/s]
R03	8.71
R04	8.22
R05	7.64
R06	7.37
R07	6.97
R08	6.70
R10	6.75

Table 3.03 Peak frequency of simulated wave signals.

Despite some very small undesirable effects, the generated waves keep being regular, and hence, linear wave theory is used to described waves themselves.
Linear wave theory has been used to understand what kind of waves this work has to deal with, first distinguishing shallow water, deep water and intermediate water situations for each case and then studying the particle velocity under the waves themselves. First the coefficients h/L and kh are computed in order to verify which condition among the three previously exposed is satisfied: the results are gathered in table 3.03.

WAVE	h/L	kh
R03	0.50	3.14
R04	0.44	2.79
R05	0.40	2.51
R06	0.36	2.29
R07	0.33	2.09
R08	0.31	1.93
R10	0.31	1.93

Table 3.04 Values of h/L and kh coefficients for each simulated wave to define depth condition.

While wave R03 represents a deep water condition, the others are intermediate values, but very close to the limit between intermediate and deep water. The fact that they are very close to deep water condition makes further analysis worth to be done. In particular, particle velocities are computed at the mean water level MWL according to expressions (2.38) and (2.39), in order to understand the kind of trajectories that particles themselves assume under the free surface. Mean value of maximum horizontal and vertical velocities, u and w respectively, are computed under each wave crest. The velocities u and w under the crests are the biggest ones, because of the smooth asymmetry of the generated waves that brings to slightly bigger wave amplitude and then velocities over MWL. Furthermore, a look at the development of velocities all along simulation time is interesting too.

As it is possible to notice, the difference between u and w enhances with respect to a decrease of h/L ratio (and of the kh coefficient) and hence, it means that the higher h/L is, the smaller is the difference between the two. This result agrees with linear wave theory and confirms that in deep water conditions the two velocities are almost equal and then particles trajectories tend to be circular ones, while when approaching lower values of h/L, and hence entering intermediate or shallow water conditions, trajectories tend to take elliptical form. However, as already said, h/L values indicate that the considered waves, although they belong to intermediate water depth conditions, their characteristics maintain very close to the deep water ones and both mean velocities and plots show that the difference between u and w are very small. Plots of horizontal and vertical velocities of R03 and R08 are shown, as examples to understand the difference between the two velocities, in Figure 3.16 and Figure 3.17. The very small relative percentage gap between the two enhances this concept (Figure 3.18).

Then, all the experimental waves do have circular particles trajectory and then, as linear theory explains, velocity varies very fast under the free surface along water depth, becoming very small at half the channel depth, according to the vertical velocity profile that generally belongs to deep water cases, [6]. Vertical profiles for waves from R03 to R08 are shown in Figure 3.19. Although completely developed

deep water conditions are never really achieved in reported waves tests, velocity decreases very quickly according to depth achieving very small velocity values.

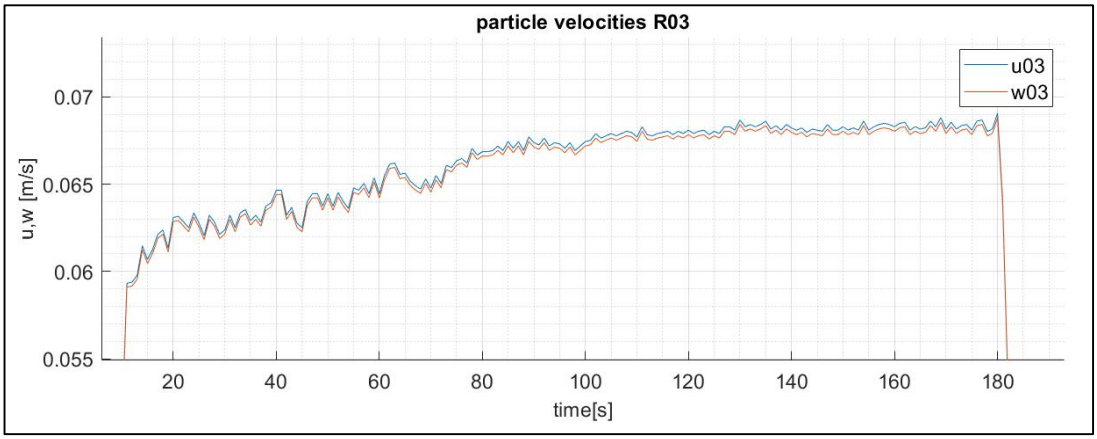

Figure 3.18 Horizontal and vertical particle velocities in wave R03.

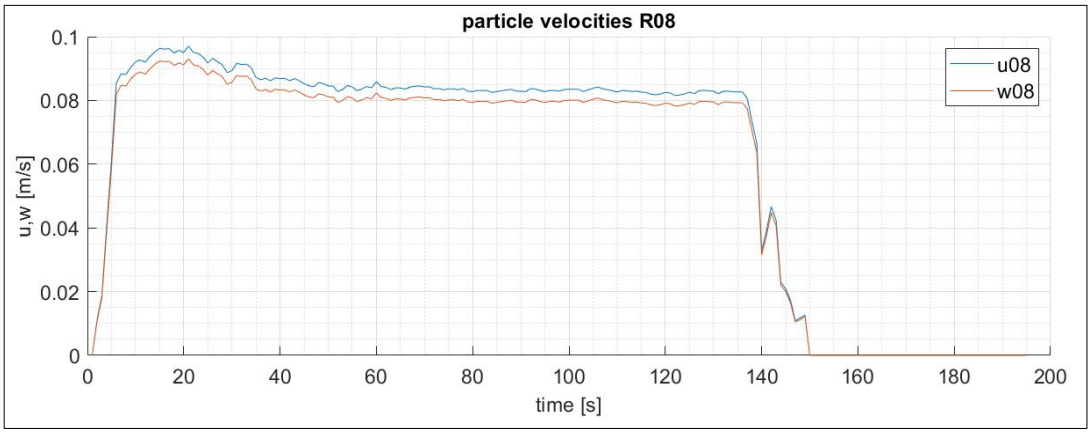

Figure 3.19 Horizontal and vertical particle velocities in wave R08.

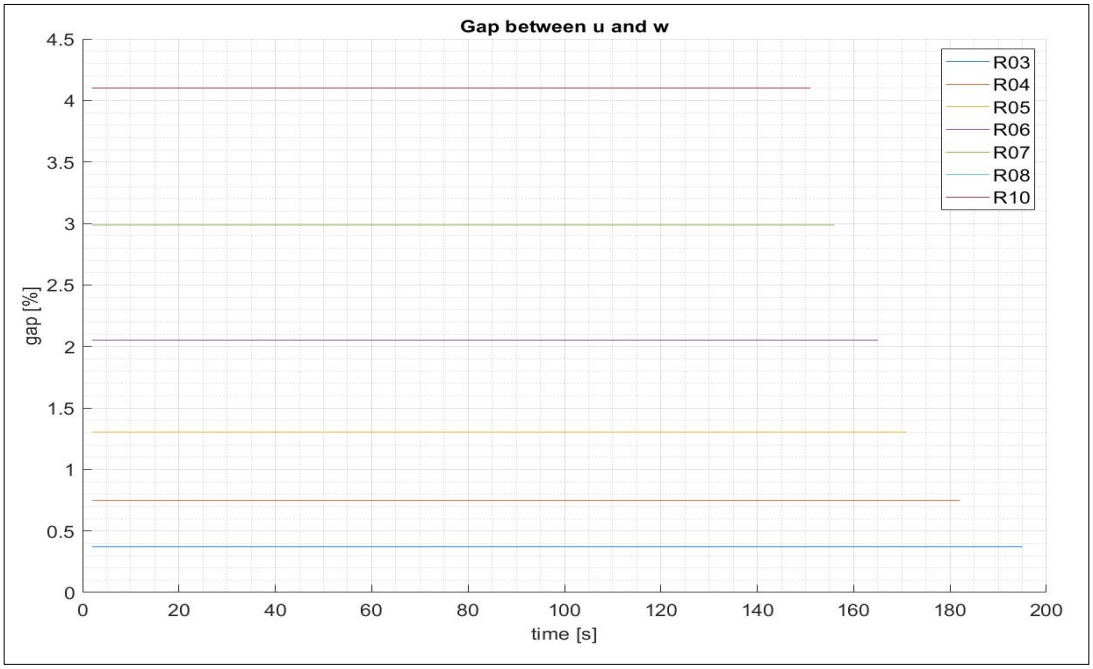

Figure 3.20 Percentage difference between horizontal and vertical velocities for all the simulated waves.

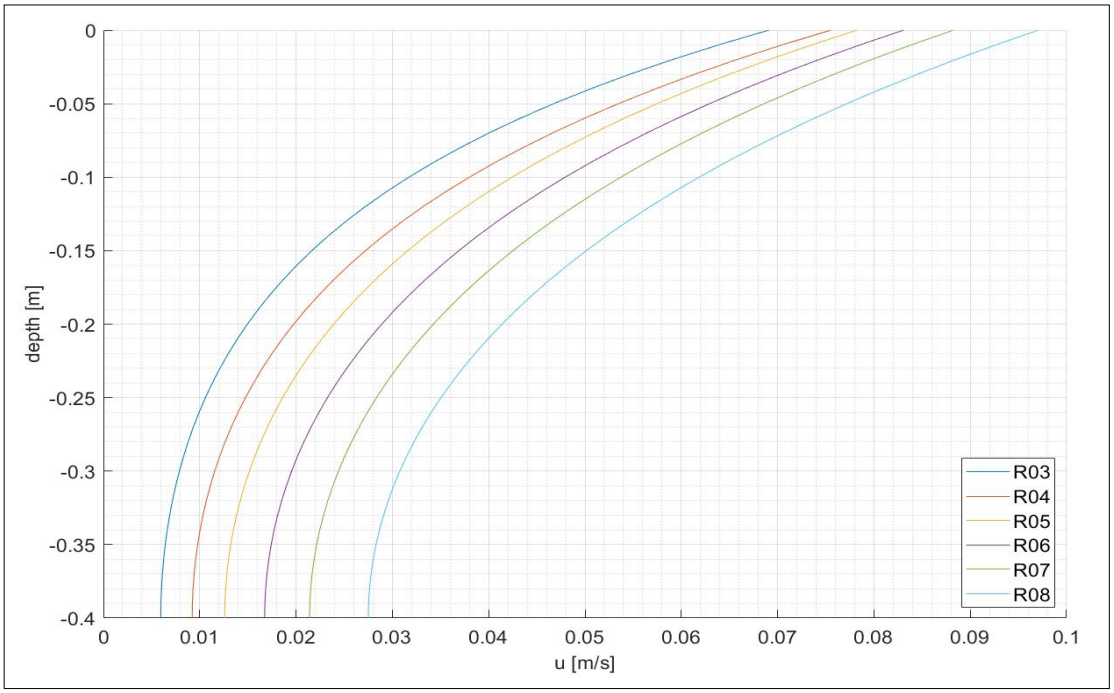

Figure 3.21 Horizontal velocity profile for all the tested waves.

4

Mathematical model

In this chapter, the numerical model used to solve the problem is presented, describing how all theoretical issues have been applied in order to obtain consistent results. A potential flow model has been implemented in the software Matlab with the purpose of modelling the buoy behavior under the action of different regular sea states, adopting 3 Degrees of Freedom: surge, heave and pitch.
The model consists of two main parts. The first one is related to the frequency domain, where hydrodynamic coefficients have been assessed through the use of specific Matlab functions that will be later discussed and the general behavior of the buoy is determined.
The second part of the model is related to the time domain, trying to represent in a more specific way how the buoy moves in time under the action of certain free surface conditions.
In order to understand this, all theoretical concepts expressed in the previous chapter will be discussed again describing their specific application to the case of a cylindrical buoy.
Primary importance on the application of the model is linked to the free surface behavior, that is, as already said, defined by regular waves. A sketch of the composition of the model and how it works is presented in Figure 4.01.

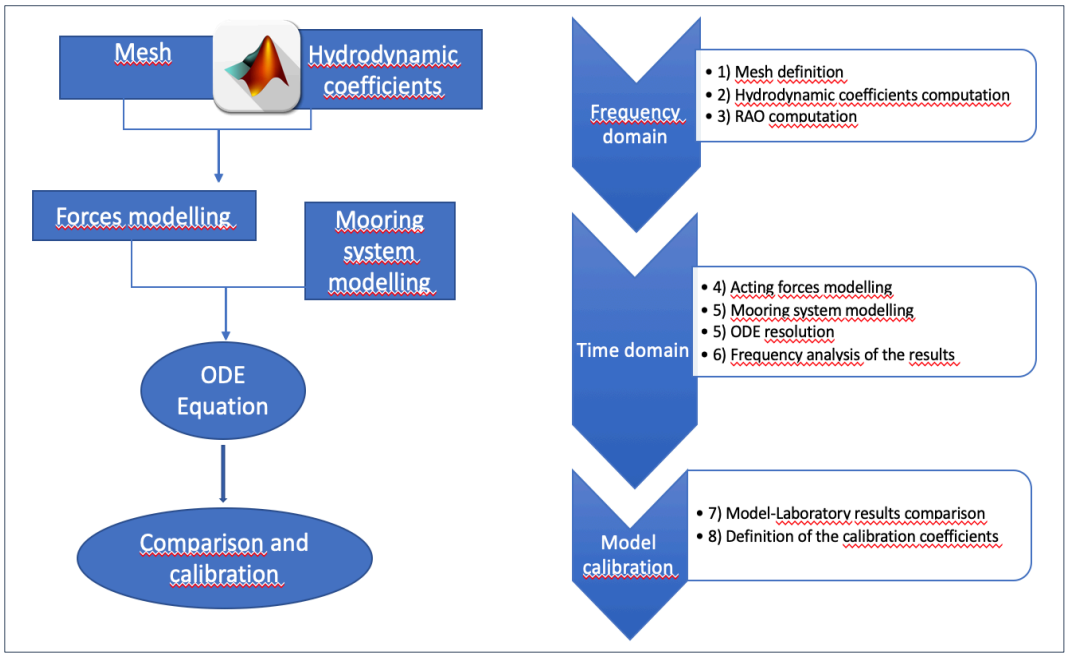

Figure 4.01 Mathematical model scheme.

4.1 Acting forces

Before describing in a precise way the equations constituting the code, it is necessary to clearly understand which are the forces between the ones exposed in chapter 2.2 that must be taken into account and, on the other hand, which can be neglected. In particular the influence of diffraction and drag forces has to be evaluated so as to understand if they must be considered in the calculations and hence if their influence on buoy motion is relevant or not.
First, Koulegan-Carpenter number has been computed. As already said in chapter 2.2, through this dimensionless quantity it is possible to evaluate the ratio between drag forces and inertia forces, hence understand if drag forces assume relevant importance or not in the specific work case. If $KC > 10$ drag forces are predominant over inertia ones, while if $KC \leq 2$ inertia forces are predominant with respect to drag forces and the latter can be neglected. If KC assumes intermediate values both inertia and drag forces are relevant and cannot be neglected, [10]. KC is computed as

$$KC = \frac{2\pi A}{L} \tag{4.01}$$

where:

- A represents the waves amplitude;
- L represents a characteristic dimension of the body (diameter).

WAVE	KC
R03	3.02
R04	3.39
R05	3.77
R06	4.14
R07	4.52
R08	4.90
R10	7.54

Table 4.01 Koulegan-Carpenter number for the simulated waves.

As shown in table 4.01, Koulegan-Carpenter numbers for the studied simulation waves takes intermediate values: in particular, KC gets bigger when wave height enhances. So, it is possible to conclude that drag forces have to be taken into account as much as inertia forces.

At this point the relative importance of diffraction forces has to be found out. The ratio between a relevant buoy dimension l (in this case diameter D) and the wave length λ has to be computed. If $\frac{l}{\lambda} \ll 1$, it means that the body is too small in order to produce relevant diffraction phenomena and hence diffraction forces can be neglected compared with the other acting forces, otherwise, if $\frac{l}{\lambda} \geq 1/5$, diffraction forces cannot be neglected.

The results for each wave case are presented in table 4.02:

WAVE	l/λ
R03	0.063
R04	0.056
R05	0.050
R06	0.046
R07	0.042
R08	0.039
R10	0.039

Table 4.02 l/λ ratio for the simulated waves.

So, the ratio $\frac{l}{\lambda} \ll 1$ and it is lower than 1/5 too. This means that buoy diameter is very small compared with the wave length, so diffraction phenomena are very small and then negligible.
Finally, a plot representing the relative importance of inertia, drag and diffraction forces is reported, highlighting this thesis buoy situation in red. In particular the plot is defined by the ratio between wave length and buoy diameter on abscissa axis and the ratio between wave height and buoy diameter on the ordinate axis. The latter is defined by a ratio which is similar and proportional to the Koulegan-Carpenter number.

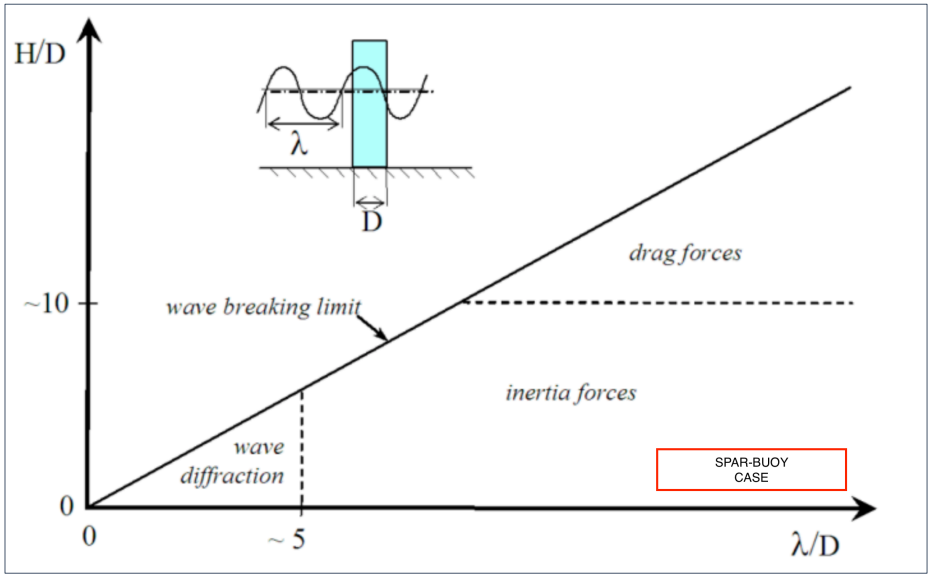

Figure 4.02 Acting forces and their influence domains with respect to H/D and λ/D ratios [11].

The dynamics of body motions is described by Newton's second law, which links internal and external forces as stated in equation (2.90). Internal forces are expressed by the right member of the equation and are only linked to the characteristics of the body, while external forces, represented by the left term, are defined as the sum of all the forces that are transferred from the external environment to the body. In this particular case, external forces are transferred to the buoy by water and by the mooring system.
In the next paragraph, it follows an explanation on how internal and external forces are computed.

4.1.1 Internal forces

Internal forces are expressed through the inertial terms

$$\begin{bmatrix}\vec{F}\\ \vec{M}\end{bmatrix}=\begin{bmatrix}\bar{\bar{P}} & \bar{\bar{T}}\\ -\bar{\bar{T}} & \bar{\bar{I}}\end{bmatrix}\cdot\begin{bmatrix}\vec{\ddot{\tau}}\\ \vec{\ddot{\theta}}\end{bmatrix}=\bar{\bar{M}}\begin{bmatrix}\vec{\ddot{\tau}}\\ \vec{\ddot{\theta}}\end{bmatrix} \tag{4.02}$$

where $\vec{F}$, $\vec{M}$, $\vec{\ddot{\tau}}$ and $\vec{\ddot{\theta}}$ are the vectors of forces, moments, linear acceleration and angular acceleration respectively. Matrix M is the so-called inertia tensor, representing the inertial properties of the buoy. In case of a single body, it is represented by a 6x6 matrix, where:

- $\bar{\bar{P}}$ is the mass matrix, regarding the first three DoFs described by the Cartesian reference system: the three translations surge, sway and heave. It is filled as shown in equation (4.03).

$$\bar{\bar{P}} = \begin{bmatrix} M & 0 & 0 \\ 0 & M & 0 \\ 0 & 0 & M \end{bmatrix} \tag{4.03}$$

- $\bar{\bar{I}}$ is the inertial matrix, concerning the rotation DoFs (roll, pitch, yaw), and it is filled with the buoy moments of inertia

$$\bar{\bar{I}} = \begin{bmatrix} I_{44} & I_{45} & I_{46} \\ I_{54} & I_{55} & I_{56} \\ I_{64} & I_{65} & I_{66} \end{bmatrix} \tag{4.04}$$

in which moments of inertia are computed as in expressions (4.05), taking X, Y and Z as the radians of rotation of the corresponding axis.

$$I_{44} = \int_M (Y^2+Z^2)\,dm \qquad I_{55} = \int_M (X^2+Z^2)\,dm \qquad I_{66} = \int_M (Y^2+X^2)\,dm$$

$$I_{45} = I_{54} = -\int_M XY\,dm \qquad I_{46} = I_{64} = -\int_M XZ\,dm \qquad I_{65} = I_{56} = -\int_M ZY\,dm \tag{4.05}$$

- $\bar{\bar{T}}$ is the coupling matrix, containing the terms that are linked both to translations and rotations

$$\bar{\bar{T}} = \begin{bmatrix} 0 & Mz_{G_0} & -My_{G_0} \\ -Mz_{G_0} & 0 & Mx_{G_0} \\ My_{G_0} & -Mx_{G_0} & 0 \end{bmatrix} \tag{4.06}$$

4.1.2 External forces

As already reported at the beginning of this chapter, external forces are the sum of all the forces which are transferred to the buoy from the external environment: in the case of this thesis, are considered to be part of this group the ones exerted on the body by water and the mooring system. External forces can be split into two main groups: hydrostatic, which are consequence of the balance between gravity forces, and hydrodynamic, due to dynamic pressure and viscous effects.

Hydrostatic

Reintroducing chapter 2 concepts, hydrostatic forces are the formalization of Archimede's principle, which states the relation between body weight and its buoyancy. A floating body at equilibrium must respect the following conditions:

$$Mg=\rho g V_0 \qquad X_{C0}=X_{G0} \qquad Y_{C0}=Y_{G0} \tag{4.07}$$

where

- V_0 is the body volume;
- C_0 is the hull centre;
- G_0 is the gravity centre.

As in the case of internal forces, it is necessary to introduce a 6x6 matrix which defines hydrostatic restoring force for all the 6 DoFs. This matrix is called hydrostatic restoring matrix (4.08). The positions of the matrix occupied by not null terms are only the ones linked to heave translation, roll and pitch rotations. The latter are computed as described in expressions (4.09). Surge, sway and yaw DoFs are not interested in this kind of force.

$$\bar{\bar{S}}=\begin{bmatrix} 0 & 0 & 0 & 0 & 0 & 0 \\ 0 & 0 & 0 & 0 & 0 & 0 \\ 0 & 0 & S_{33} & S_{34} & S_{35} & 0 \\ 0 & 0 & S_{43} & S_{44} & S_{45} & 0 \\ 0 & 0 & S_{53} & S_{54} & S_{55} & 0 \\ 0 & 0 & 0 & 0 & 0 & 0 \end{bmatrix} \tag{4.08}$$

$$S_{33}=\rho g \iint dS = \rho g V_0 \qquad S_{44}=\rho g \iint_{S_W} Y^2 dS + \rho g V_0 (Z_{C_0} - Z_{C_0})$$

$$S_{55}=\rho g \iint_{S_W} X^2 dS + \rho g V_0 (Z_{C_0} - Z_{C_0}) \qquad S_{34}=S_{43}=\rho g \iint_{S_W} Y\, dS \tag{4.09}$$

$$S_{35}=S_{53}=\rho g \iint_{S_W} X\, dS \qquad\qquad S_{45}=S_{54}=\rho g \iint_{S_W} XY\, dS$$

Once hydrostatic restoring matrix is known, it is possible to define the effective hydrostatic forces as the product between matrix (4.08) and the displacement vector:

$$\begin{bmatrix} \overrightarrow{F_{HD}} \\ \overrightarrow{M_{HD}} \end{bmatrix} = \bar{\bar{S}} \begin{bmatrix} \vec{\tau} \\ \vec{\theta} \end{bmatrix} \tag{4.10}$$

Hydrodynamic

Hydrodynamic forces are due to the wave field which the buoy is influenced by. As introduced at the beginning of paragraph 4.1, not all the hydrodynamic forces influence the buoy motion the same way, but it has been found that diffraction force can be neglected because of the small dimensions of the buoy with respect to wave length. Thus, hydrodynamic forces actually considered acting on the body are excitation force, radiation force and drag force.

For what excitation force F_e is concerned, it depends both on frequency ω and time t:

$$F_e(\omega,t) = \overline{f_e}(\omega) \cdot A(t) \tag{4.11}$$

where

- $\overline{f_e}(\omega)$ is a six elements vector of the excitation force coefficients (one coefficient for each DoF) and it depends on frequency only.
- A(t) is the wave amplitude, which is instead time dependent.

F_e results to be a six elements vector, representing the force linked to the incoming undisturbed wave for each DoF, concerning a single value of wave frequency. Coefficients $\overline{f_e}(\omega)$ derive from equation (2.92) and their calculation has practically been performed through the use of a particular matlab function called NEMOH, later explained in the following chapter 4.3. However, their value keeps being the same both in frequency and time domain. This is due to the fact that this work deals with linear regular waves. When this situation does not verify and, instead of regular waves a combination of linear waves happens, the coefficients take a slightly different expression which takes into account the convolution of all the several wave frequencies involved.

Reintroducing radiation contribute, it expresses the force computed considered a flat free surface, without waves perturbation, but only produced by the body motion. Practically, it represents a sort of loss of the body energy and hence it counteracts excitation force in order to reduce buoy motion. For this reason, radiation force has been modelled as described in equation (4.12), with $\overline{\overline{R_d}}$ matrix whose elements are the radiation damping coefficients and $\bar{u}$ the vector containing velocities that buoy assumes during its motion along each DoF.

$$F_r(\omega,t)=\overline{\overline{R_d}}(\omega)\cdot\bar{u}(t) \tag{4.12}$$

where:

- $\overline{\overline{R_d}}(\omega)$ is the radiation damping matrix (6x6), containing the radiation coefficients; the latter are frequency dependent as the excitation force coefficients.
- $\bar{u}(t)$ represents the buoy velocity assumed at each time instant during its motion.

Such as in case of excitation force, radiation force depends both on frequency, because of the fact that radiation coefficients are defined in frequency domain, and time, as it depends on buoy velocity too (which is function of time). The values of radiation damping coefficients are still valid in time domain due to the fact that this thesis deals with regular waves as well.

Last considered external hydrodynamic contribute is drag force. It is computed considering form drag only, being the buoy made of a very smooth material and hence viscous drag forces become negligible compared with the other contributes.
This kind of force will be included in translations only, because of the fact that in these cases it is possible to relate fluid velocity and body velocity in a simple way, having both the same measure unit and directions, while in rotations a complex procedure should be developed in order to be able to relate fluid velocity and buoy rotation velocity. For this reason, it has been decided to take into account drag force in translations only.
For sake of clarity, drag force expression is reported again below:

$$F_{drag}=-\frac{1}{2}\rho\bar{A}\bar{C}_d\cdot|\bar{u}(t)|\cdot\bar{u}(t) \tag{4.13}$$

- $\bar{C}_d$ is the vector of drag coefficients.
- A is the vector containing the values of the areas concerning the different DoFs.

The velocity considered in the drag force expression should be the relative velocity, namely the difference between water particles velocity and buoy velocity. As the aim of this thesis is to build a simplified model, velocity $\bar{u}(t)$, on which drag force depends, has been set into the ODE as the velocity of the buoy only. This is possible because of the fact that the two velocities are comparable at the MWL and within a little depth only, as particle velocity decreases exponentially according to vertical axis, from the MWL to the bottom. The variation of particles velocity along water depth is shown in Figure 3.21.
Studying the incident wave characteristics and in particular the ratio between water depth h and wave length it is possible to understand that according to the treated incident waves,

we are in cases representing both deep water and intermediate water, but very close to the deep water condition.
At the end, as described in section 3.2.1, not negligible water particles velocity values happens within a very small depth from the MWL, while the main part of the depth is interested by very small and negligible both horizontal and vertical velocity values. Besides, a very small buoy area is involved and then the resulting drag force due to particles velocity happens to be very small. Then, the sum of these reasons and the fact that the aim of this work is to build a predictive simplified model, brings to the decision of considering the effect of particles velocity negligible and hence velocity $\bar{u}(t)$ as the one related to the buoy only.
Having the spar buoy, unless for the very small crown in which catenaries are inserted, a perfect cylindrical form, its drag coefficient C_d can be found in literature, for example as results in [13, 33, 39], where, as well as in reported in the table of Figure 4.03, it is often linked to the ratio L/D between cylinder length and diameter.

Body	Laminar/Turbulent	Status	C_d
Cube	$Re > 10000$		1.05
Thin Circular Disc	$Re > 10000$		1.1
Cone ($\theta = 30°$)	$Re > 10000$		0.5
Sphere	Laminar $Re \leq 2 \times 10^5$		0.5
	Turbulent $Re \geq 2 \times 10^6$		0.2
Ellipsoid	Laminar $Re \leq 2 \times 10^5$		$0.3 - 0.5$
	Turbulent $Re \geq 2 \times 10^6$		$0.1 - 0.2$
Hemisphere	$Re > 10000$	Concave Face	0.4
		Flat Face	1.2
Rectangular Plate	$Re > 10000$	Normal to the flow	$1.1 - 1.3$
Vertical Cylinder	$Re \leq 2 \times 10^5$	$L/D = 1$	0.6
		$L/D = \infty$	1.2
Horizontal Cylinder	$Re > 10000$	$L/D = 0.5$	1.1
		$L/D = 8$	1
Parachute	Laminar Flow		1.3

Figure 4.03 Drag coefficients for common body geometries [33].

Furthermore, for the particular case of the cylindrical form, a more accurate definition of C_d, for what the two considered DoFs are concerned, is given in the following Figure 4.04.

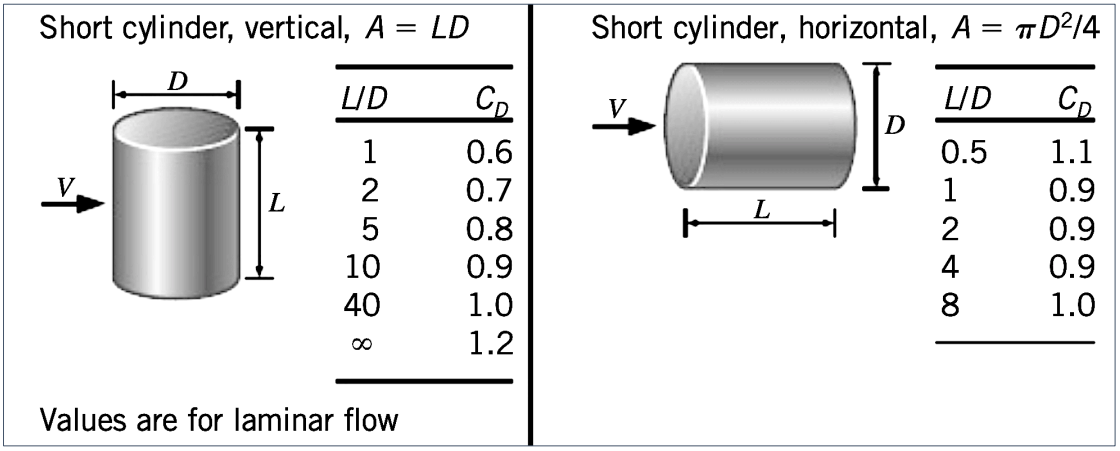

Figure 4.04 Cylinder drag coefficients for laminar flow and different L/D ratios [12].

In order to obtain the final results of the drag coefficients, a linear interpolation has been performed between the values contained in Figure 4.04, resulting in 0.84 and 0.98 for surge and heave drag coefficients respectively.

4.2 Equation of motion

With the assumptions introduced in section 4.1 it is possible to describe motion according to the Morrison's method. It allows to obtain water particles kinematic from the analytical solutions of different wave theories, assuming that the body does not disturb water particles motion. This brings to the fundamental advantage of reducing the complexity of the model and thus, the computational cost of the simulations.
Its applicability depends on the entity of body diameter D, wave height H and wave length λ, in order to define if the loads induced by the waves are dominated by inertia, drag or diffraction forces. Slender members with relative small diameter compared to the wave length and the wave height are dominated by drag forces, while for intermediate ranges are dominated by inertia forces. In both latter cases, Morrison's method is applicable, being more determinant the inertial or viscous term of the equation. As already reported, when $\frac{D}{\lambda} \geq 1/5$ diffraction forces cannot be neglected and potential flow theory is required to the computation of wave diffraction effects.
So, according to the results of section 4.1, where it is stated that buoy is slender enough to not create any disturb to wave particles kinematic and diffraction forces are negligible compared with inertia and drag ones, Morrison's method will be adopted.

The buoy has been modelled as a single body with three DoFs: horizontal translation along wave propagation direction defined through x axis in the Cartesian reference system

(surge), vertical translation along z axis (heave) and a rotation restrained in the vertical plane (x-z) defined by the two translations (pitch). Besides, each DoF is characterized by an index number in order to make practically simpler the understanding of the equations: surge mode has index 1, heave mode has index 3 and pitch mode has index 5.
Once that acting forces have all been introduced, it is possible to define buoy equation of motion in a complete manner. Through the application of this equation, it is possible to solve the problem of the buoy motion under the effect of incident waves in time domain and the result consists in the description of buoy behavior with respect to time.
Before writing the final form of the equation, a summary of forces expressions is developed:

- Excitation force

$$F_{exc} = \bar{f}_{exc} \cdot \eta(t) \tag{4.14}$$

- Radiation damping force

$$F_r = \overline{\overline{R_d}}(\omega) \cdot \dot{\bar{x}}(t) \tag{4.15}$$

- Hydrostatic restoring force

$$F_{hyd} = -\overline{\overline{KH}} \cdot \bar{x}(t) \tag{4.16}$$

- Drag force

$$F_{drag} = -\frac{1}{2} \rho \overline{A} \overline{C}_d \cdot |\dot{\bar{x}}(t)| \cdot \dot{\bar{x}}(t) \tag{4.17}$$

where f_{exc}, R_d and KH are the hydrodynamic coefficients whose calculation will be later explained, and C_d is drag coefficient. Terms $x(t)$ and $\dot{x}(t)$ represent generic position and velocity of the buoy respectively. Having to deal with linear regular waves, hydrodynamic coefficients maintain the same value both in frequency and in time domain, so that the ones computed as function of frequency keeps being the same without any modifications in motion equation too.
Remembering Newton's second law (2.90) and considering the previously defined acting forces, it is possible to write down motion equation, [40, 41]. Equations for all three involved DoFs, surge (4.18), heave (4.19) and pitch (4.20) respectively are reported for clarity:

$$(M_1 + C_{a1}) \cdot \ddot{x}(t) = F^1_{exc}(t) + F^1_r(t) + F^1_{hyd}(t) + F^1_{drag}(t) \tag{4.18}$$

$$(M_3+C_{a3}) \cdot \ddot{z}(t) = F^3_{exc}(t)+F^3_r(t)+F^3_{hyd}(t)+F^3_{drag}(t) \quad (4.19)$$

$$(M_5+C_{a5}) \cdot \ddot{\theta}(t) = F^5_{exc}(t)+F^5_r(t)+F^5_{hyd}(t) \quad (4.20)$$

Substituting the forces with expressions (4.18), (4.19) and (4.20), and writing buoy displacements as x (surge), z (heave) and θ (pitch), they become

$$(M_1+C_{a1})\cdot\ddot{x}(t)=f^1_{exc}\cdot\eta(t)-(R^{11}_d+R^{13}_d+R^{15}_d)\cdot\dot{x}(t)-(KH^{11}+KH^{13}+KH^{15})\cdot x(t)-\frac{1}{2}\rho AC^1_d\cdot|\dot{x}(t)|\cdot\dot{x}(t) \quad (4.21)$$

$$(M_3+C_{a3})\cdot\ddot{z}(t)=f^3_{exc}\cdot\eta(t)-(R^{31}_d+R^{33}_d+R^{35}_d)\cdot\dot{z}(t) - (KH^{31}+KH^{33}+KH^{35})\cdot z(t) - \frac{1}{2}\rho AC^3_d\cdot|\dot{z}(t)|\cdot\dot{z}(t) \quad (4.22)$$

$$(M_5+C_{a5})\cdot\ddot{\theta}(t) = f^5_{exc}\cdot\eta(t) - (R^{51}_d+R^{53}_d+R^{55}_d)\cdot\dot{\theta}(t) - (KH^{51}+KH^{53}+KH^{55}) \cdot \theta(t) \quad (4.23)$$

where M_i and C_{ai} are the summation of the picked DoF Inertia and added mass elements.

So, from these equations it is clear that excitation force is responsible for enhancing buoy motion, making the body oscillating far from its balance position, while all the others contributes as radiation, buoyancy and drag forces act as restoring ones, which try to bring buoy back to equilibrium.
Considering now all the three DoFs together, it is possible to write down the motion equation in a matrix form, where single hydrodynamic coefficients are replaced by matrices introduced in chapter 4.1 and $\bar{x}$ stands as total displacements vector ($\bar{x} = [x\ z\ \theta]$):

$$(\bar{\bar{M}}+\bar{\bar{C_a}}(\omega))\cdot\ddot{\bar{x}}(t) = \bar{f_{exc}}(\omega)\cdot\eta(t) - \bar{\bar{R_d}}(\omega)\cdot\dot{\bar{x}}(t) - \bar{\bar{KH}}\cdot\bar{x}(t) - \frac{1}{2}\rho\ A\ \bar{C_d}\cdot|\dot{\bar{x}}(t)|\cdot\dot{\bar{x}}(t) \quad (4.24)$$

Added mass coefficient C_a and radiation force coefficient R_d computation will be explained in the following section. Like excitation force and radiation coefficients, C_a is frequency dependent as well. It has the unit of measure of a mass [kg] and represents the mass of fluid volume that the body moves during its own motion through the fluid itself. It is summed to Inertia matrix in order to consider in motion equation both mass coming from the body and the one associate with the displaced fluid.

4.3 Frequency domain

The first part of the code is developed in frequency domain, first of all because of the fact that hydrodynamic coefficients needed to evaluate acting forces are frequency dependent, so, it results useful to calculate them in frequency domain before passing to time domain. Besides, it is very interesting to get a first understanding of the buoy behavior at different frequencies. For example, in the design of a wave energy converter, principal importance is taken by the definition of the resonance frequency of the body in order to produce as much energy as possible, tuning the device at the most energetic frequency band of the wave field, as introduced in [23]. Design is not this thesis aim, not having to deal with a WEC but with a simple buoy. Nevertheless, a preliminary understanding of the effect that regular waves created by the wave generator have on the buoy is very important in order to create an expectation about the frequency and the amplitude of the buoy motion.

The aim of this part of the code is to determine the elements that the equation of motion needs to be solved: inertia matrix, containing mass for translation DoFs, moments of inertia for rotation DoFs and added mass matrix, buoyancy matrix, coefficients of excitation force, coefficients of radiation force.
As showed in section 4.1, internal forces expressed by inertia, added mass matrixes and hydrostatic ones do not need any potential integration because they are independent from the incident wave. Then, dimensions and weight of the body are enough, and for their computation a mesh definition is required only, in order to be able to perform the numerical integration on the body surface. In order to do that, a function called Mesh is used: it allows both the grid construction and the calculation of the specified elements. The latter function is going to be better explained in next paragraph.

For what the computation of the excitation force and radiation coefficient is concerned, a different kind of integration has to be performed.
Being the general expressions of excitation and radiation forces written as (4.25) and (4.26) respectively, again reported for clarity, the aim of this part is the resolution of the potential $\hat{\phi}$ and its integration on the buoy surface in order to get to the hydrodynamic coefficients values.

$$F_{exc,i} = i\omega\rho \int\int_S \left(\hat{\phi}_0 + \hat{\phi}_d\right) n_i dS \tag{4.25}$$

$$F_{e,i} = i\omega\rho \int\int_S \hat{\phi}_r \, n_i dS \tag{4.26}$$

This operation is performed numerically by the use of BEM (boundary element method) integration. Software offering the capability of performing this kind of integration are several and the most widely used are WAMIT ® [34], developed by the Massachussetts

Institute of Technology (MIT) and AQWA, part of the workbench package of ANSYS ®, [28].
In this case, however, the open-source code Nemoh has been adopted in order to perform the calculation of the hydrodynamic coefficients. It has been developed by the Laboratoire d'Hydrodynamique, Énergétique et Environnement (LHEEA) laboratory at the Ecole Centrale de Nantes, France, over the past 30 years. It does not offer the only calculation code, but it comes in a package with a Matlab toolbox to control Nemoh and the already introduced meshing tool Mesh too. The latter has to be ran before the computation performed by Nemoh, in such a way to give Nemoh itself the meshing grid upon which integrate the potential, [14].

BEM method solves the fluid velocity potential integration on the body surface applying the following hypothesis:

1) Fluid continuity;

2) Strains proportional to deformations velocity (Newtonian fluid);

3) Fluid homogeneity and isotropy;

4) Inviscid fluid;

5) Fluid initially at rest (only gravity and external forces);

6) Atmospheric pressure assumed above free surface and surface tension neglected.

Application of the first three hypothesis enables the derivation of the Navier-Stokes equations, while through hypothesis 4) perfect fluid equations are obtained. Hypothesis 5) allows the definition of velocity potential $\vec{V} = \vec{\nabla}\phi$. The problem is then solved thanks to the application of an additional BC (boundary condition), assuming body surface as impermeable and thus forcing fluid velocity to be equal to the normal velocity of the body in the normal direction of the structure surface. Latter BC mathematical expression is given by equation (4.27) where C and E represent body surface and centre of gravity respectively.

$$\vec{V}_{\vec{n}|_C} = \left.\frac{\partial \phi}{\partial n}\right|_C = \vec{V}_{E\vec{n}_C} \tag{4.27}$$

Surface need to be discretized in elements as the integration is performed at each element composing the surface.

To solve the BC on the body, the free surface and the bottom the Green's functions are used. The solutions of the problem are the velocities and then the potential is obtained through the influence coefficients. These, need to be discretized and then integrated on the surface panel. In the general form, they are expressed as:

$$C=C_1+C_2 \tag{4.28}$$

$$C_1=\iint_S \; f\left(\frac{1}{MM_1^{'}}\right) dS(M_1^{'}); \qquad \text{for } M_1^{'}(x^{'}, y^{'}, z^{'}) \tag{4.29}$$

$$C_2=\iint_S \; \int_{-\pi/2}^{\pi/2} \ddot{g}(\eta)\, d\theta dS(M^{'}) \tag{4.30}$$

The terms C1 are computed by an approximation to the analytical Hess formula as in [30]. For the terms C2 first the θ integral is calculated and then the double integral S is obtained numerically. Due to the slow variation of the integration term on the panel, integration in S can be achieved by using the approximation of the one point formula. For the computation of the integral in θ, the analytical formula proposed by [32] are used. Through the discretization of the integral equations the following linear systems are derived:

$$\left.\frac{\partial\tilde{\phi}}{\partial n}\right|_{Mi} = \frac{\tilde{\sigma_i}}{2} + \sum_{i=1}^{N} \tilde{\sigma_j}\tilde{K}_{ij} \tag{4.31}$$

$$\left.\tilde{\phi}\right|_{Mi} = -\sum_{i=1}^{N} \tilde{\sigma_j}\tilde{S}_{ij} \tag{4.32}$$

$$\tilde{S}_{ij}=\frac{1}{4\pi}\iint_S \; \tilde{S}(M_i, M^{'})dS(M^{'}) \tag{4.33}$$

$$\tilde{K}_{ij}=\frac{1}{4\pi}\left.\frac{\partial}{\partial n}\right|_{M'}\iint_S \; \tilde{S}(M_i, M^{'})dS(M^{'}) \tag{4.34}$$

Where $\tilde{S}$ is the Green's function of the problem and N stands for the number of bodies considered. The element " ˜ " indicates a complex term. At this point, the elemental radiation and diffraction problems are respectively expressed as follows:

$$\left.\frac{\partial\tilde{\phi}_e}{\partial n}\right|_{\Sigma_i} = \sigma_i^q \tag{4.35}$$

$$\left.\frac{\partial\tilde{\phi}_e}{\partial n}\right|_{\Sigma_i} = -\left.\frac{\partial\tilde{\phi}_I}{\partial n}\right|_{\Sigma_i} \tag{4.36}$$

Where $\sigma_i^q = \vec{e}_q \cdot \vec{n}$ for q = 1,2,3 and $\sigma_i^q = (\vec{e}_{q-3} \wedge \mathrm{O}\vec{P})$ for q = 4,5,6 which are the modes corresponding to translational and rotational modes respectively. The term $\vec{e}_q$ represents the unit vector of the axis q. The adoption of complex numbers is not only due to the easier writing, but to the fact that it allows to save computational time. Calculations could be done in real numbers but the unknowns would then be twice as much as with complex numbers, having computation times of the order of $8M^3$ instead of $4M^3$ for a complex system of order M, being M the number of panels, [8]. The radiation problem is stated by a body forced with a sinusoidal motion in completely calm water, whereas the diffraction problem is stated by the still body in the presence of monochromatic waves. The pressure integral of the diffraction restitutes the excitation force coefficients. The results are the hydrodynamic coefficients shown in Figure 5.02, which are obtained in complex numbers, but are expressed in real numbers. In particular, the real part of the radiation coefficient is referred to as the added mass coefficient, its imaginary part represents the radiation damping coefficient and, at last, the module of the excitation force influence is the excitation force coefficient.

4.3.1 Mesh

Before the BEM integration performed by NEMOH ([22, 36]), the meshing tool MESH is used in order to subdivide buoy surface in elements, defining a grid and allowing the following numerical integration itself. MESH is provided as a folder in which two sub-codes are present: the first one is called Mesh.m which is useful in order to build a grid around the surface of bodies having any shape while the second one, axiMesh.m, is a meshing tool particularly created for axisymmetric bodies. Having to deal with a cylindrical and hence axisymmetric buoy, axiMesh.m has been used in order to build the grid.
Implementation of axiMesh.m needs the definition of a plane which coincides with the one containing the axis of the cylinder and cutting the buoy in 2 parts. Then, in a 2D reference system the coordinates of the vertices of half the object have to be written as an input argument in the form of a vector, supposed the object to be axisymmetric. This part has to be done already considering the object in its equilibrium position with respect to the flat free surface, setting the null vertical coordinate at the free surface.
At this point axiMesh.m code is ready to be run. During code running other input parameters are requested in order to define the mesh. In particular, the number of angular elements in which the base of the cylinder is discretized and the number of total elements, with a maximum of 2000 total ones need to be defined once the code ask them in the command window.
Once all the input arguments are defined, the code returns a plot of the grid built all around the object as it is possible to see in the example of Figure 4.05. Furthermore, inertia and hydrostatic restoring matrixes are given. This is possible because the latter two matrixes

depend on the characteristic of the object, once water density is known, so data are enough to compute them.

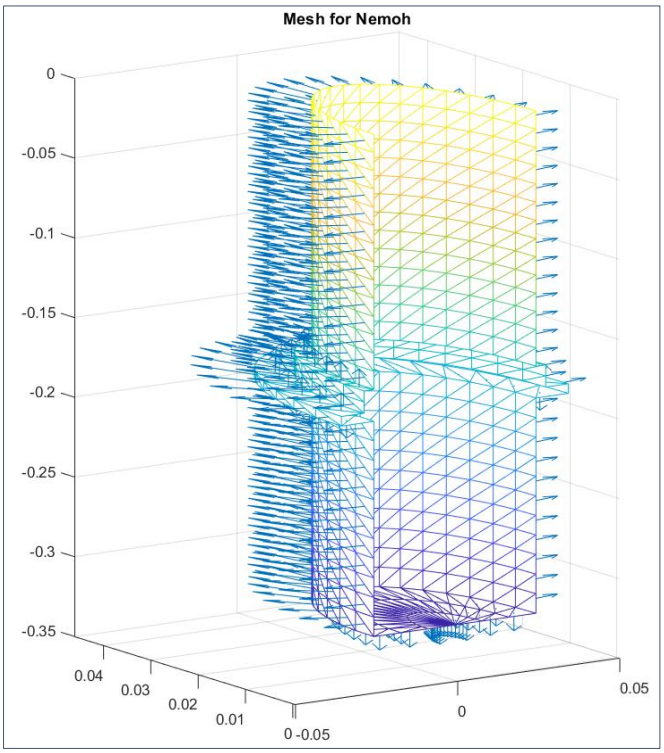

Figure 4.05 Computation mesh built by mesh.m function for BEM coefficients calculation.

4.3.2 Nemoh

After the mesh construction, enough data are available in order to run Nemoh. Frequencies vector is the only input argument that Nemoh needs, being the hydrodynamic coefficients function of ω. Frequencies have been chosen in such a way that both the wave frequency and resonance one (determined by the computation of RAO operator) would be inside the interval: the first one is defined by the wave period T, varying for each experimental wave, while resonance frequency is a body characteristics which depends on both buoy mass and dimensions and can roughly be computed at this step as

$$\omega = \sqrt{\frac{\rho g S}{m + A}} \tag{4.37}$$

After BEM integration, added mass coefficients matrix, radiation damping coefficients matrix and excitation force coefficients vectors are completely filled up. Plots and values of the resulting coefficients will be shown at the end of this section.

Last section of the frequency domain part is aimed at computing RAO (Response Amplitude Operator). It represents a significant quantity which is able to give first informations about the motion amplitude according to different incident wave frequencies. RAO computation starts applying the Fourier Transform to the linearized equation of motion and the following equation is achieved:

$$F_e = X_0 \left(- \omega^2 \left(m+A\right) + i\omega B + KH\right) \tag{4.38}$$

where ω is the frequency of monochromatic regular wave exciting the buoy, m is the mass matrix of the system and hence it coincides with Inertia matrix, A represents the added mass matrix previously computed with Nemoh function, and then B represents the radiation damping matrix. Furthermore, KH takes the role of the hydrostatic restoring matrix and F_e is the excitation force coefficient. At the end, X_0 represents the RAO and it is also the only unknown term of the equation, while all other terms have been found as explained in paragraph 4.3.1, [10]. So, RAO operator can be easily assessed by inverting previous equation, obtaining

$$X_0 = \frac{F_e}{- \omega^2 \left(\text{Inertia}+m_{ad}\right) + i\omega Rd + KH} \tag{4.39}$$

To RAO coefficient a particular meaning belongs. In facts, it is a dimensionless quantity (for translations motions), but it can also be defined in [m/m] in case of translations and in [rad/m] for rotations, as it represents how much the body moves compared with the wave height, along each DoF. For example, considering heave mode, it has to be interpreted as the ratio between the vertical oscillation of the buoy and the wave height, [20]. This is the reason why RAO is a very important parameter, capable of giving a first view of the principal characteristics of the body motion: it is possible to define a first approximated value of resonance frequency and it gives a preliminary understanding of the oscillation amplitude of the object.
Nevertheless, frequency approach lacks of a little bit of precision, not being possible to consider the nonlinear terms acting in the equation of motion. This is drag force case, whose expression contains squared velocity, which brings an accentuated nonlinearity: then, it cannot be included in the RAO computation.

Furthermore, RAO has been useful in mesh definition as well. In facts, finding hydrodynamic coefficients needs working with a good enough mesh for the representation of the body external surface, as the integration method (BEM) works on the single elements of the grid. Working with the right mesh means both having little elements enough to catch acting forces variations the best way possible and, on the other hand, avoiding the presence of too many elements in order to maintaining fair computation costs.

So, a sensitivity analysis has been performed varying the size of mesh elements through a variation of the number of total panels (input of the function axiMesh) and comparing RAO plots for different configurations.
In particular, angular discretization has been fixed to a number of "slices" equal to 20. Besides, an increasing number of total panels in which the grid is subdivided has been implemented. Eight different grids, from a coarse one to a more refined one have been defined, and RAO operator has been computed for each configuration. Finally, different mesh configurations are reported in table 4.03:

	Angular discretization	**Total number of panels**	**Cell dimension [cm^2]**
B1	20	100	0.92x7.00
B2	20	200	0.92x3.11
B3	20	300	0.92x2.15
B4	20	400	0.92x1.65
B5	20	500	0.92x1.33
B6	20	600	0.92x1.12
B7	20	700	0.92x0.96
B8	20	800	0.92x0.82

Table 4.03 Different meshes characteristics considered for sensitivity analysis.

Figure 4.06, Figure 4.07 and Figure 4.08 show surge, heave and pitch RAO respectively for different number of elements within the frequency range [3 - 9 rad/s].
With an increasing number of total panels a much more precise solution is achieved, and the gap between progressive RAO curves grows smaller. In chapter 5 the final choice is presented, taking into account the gap between different configurations for what RAO computation is concerned.

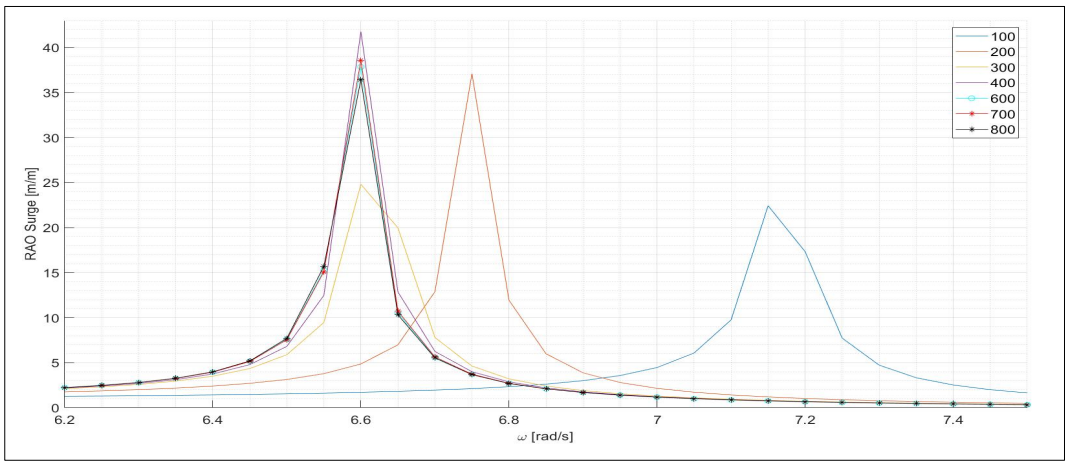

Figure 4.06 Comparison of surge RAOs for sensitivity analysis.

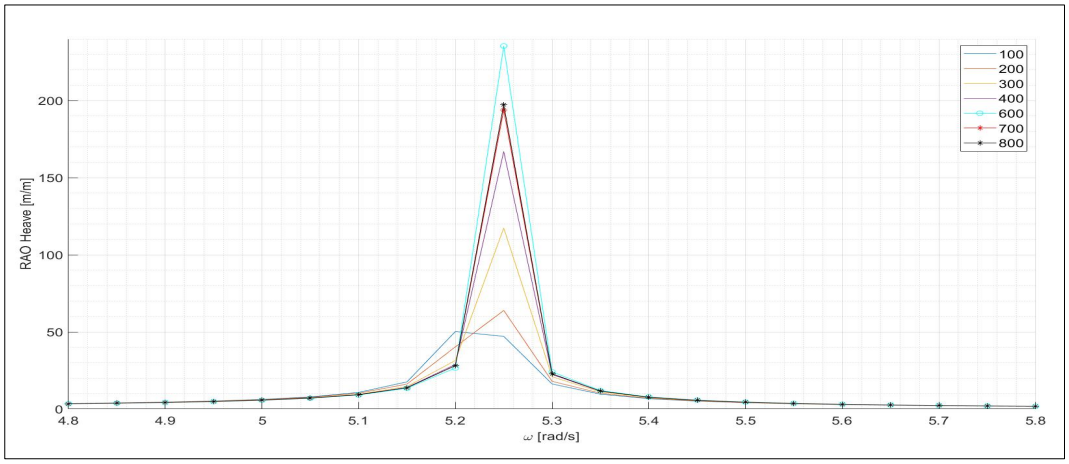

Figure 4.07 Comparison of heave RAOs for sensitivity analysis.

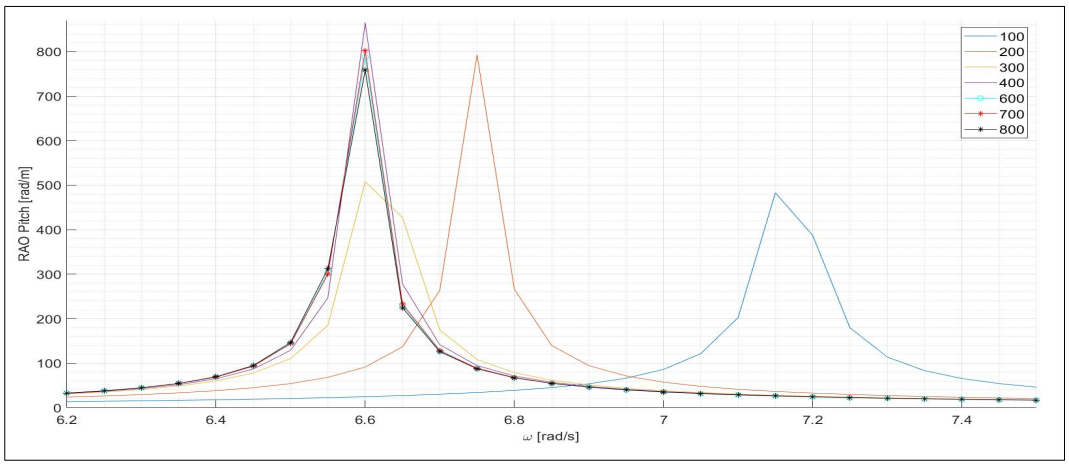

Figure 4.08 Comparison of pitch RAOs for sensitivity analysis.

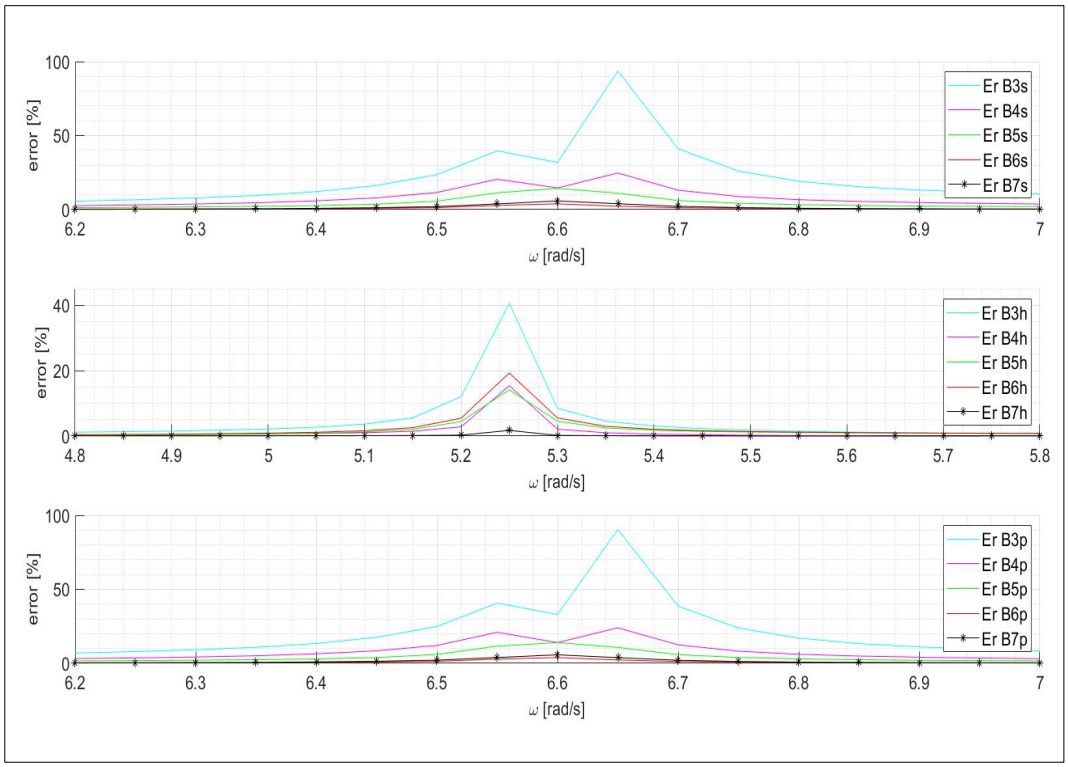

Figure 4.09 Comparison of each DoF RAOs percentage relative error.

4.4 Time domain

Up to now, the buoy motion has been described as frequency dependent, which certainly is a useful procedure, but it lacks of some important aspects: it is not possible to include nonlinear contributes (in this particular case drag force). In addition, frequency domain consists in a general description of the phenomenon associating to each frequency value, describing it according to the computation of RAO coefficient. The latter guarantees the definition of a mean value of how much the body moves under certain conditions of frequency only. For this reason, time domain is a more accurate way to describe the buoy motion, which goes further on what it is possible to understand with RAO computation. It is like opening the box and studying the evolution of the buoy motion for each singular frequency along a certain time span.

In order to describe the buoy behavior in time it is necessary to solve equation (4.24). Unfortunately, the derived motion equation is a second order one, but available time integration algorithms are usually implemented for first order differential equations (ODEs)

only. So, as to make the integration possible, (4.24) has to be transformed into an ODE. This is possible through the definition of the so-called state vector X, [21]:

$$X=\begin{pmatrix} X \\ \dot{X} \end{pmatrix} \tag{4.40}$$

Thus, equation (4.24) can be rewritten as

$$\dot{X}=\left[X(2)\ ;\ \left(\overline{f_{exc}}(\omega)\cdot\eta(t) - \overline{\overline{R_d}}\cdot X(2) - \overline{\overline{KH}}\cdot X(1) - \frac{1}{2}\rho A\overline{C_d}\cdot|X(2)|\cdot X(2)\right)/(\text{Inertia}+C_a(\omega))\right] \tag{4.41}$$

This is finally an ODE solvable through the use of usual Matlab integration algorithms such as ode15s, ode23, ode45 etc, being its general expression

$$\frac{dx}{dt}=F(x,t) \tag{4.42}$$

Note that, as already mentioned in previous chapter, hydrodynamic coefficients depend on frequency. Nevertheless, when passing from frequency domain to time domain they need sometimes an adjustment. In particular this happens when dealing with irregular waves, where sea state is defined through a so-called wave spectrum, a relationship between the distribution of energy or wave heights and frequency within the extension of sea surface considered. In the latter case both added mass coefficients and radiation force vary from frequency to time domain, because of the fact that coefficients linked to different frequencies have to be taken into account. Then, memory function K(t) related to radiation phenomenon has to be evaluated as a convolution computed taking into account all frequencies [40, 42], and at the end it can be computed as written in expression (4.43). Added mass coefficients could then be computed as expression (4.44) and equation of motion would become expression (4.45).

$$[K_{rad}](t)=\frac{2}{\pi}\int_0^{\infty}[B(\omega)]\cos(\omega\tau)d\omega \tag{4.43}$$

$$[\mu_{\infty}]=[A(\omega)]+\frac{1}{\omega}\int_0^{\infty}[K_{rad}](\tau)\sin(\omega\tau)d\tau \tag{4.44}$$

$$(M+\mu_{\infty})\ddot{X} = F_e - \int_0^t K(t-\tau)\,\dot{X}(\tau)\,d\tau - K_H X + F_{drag} + F_{others} \tag{4.45}$$

Nevertheless, this is not this thesis case, where regular waves are taken into account only. Thus, a singular frequency value is defined for each simulation. So, hydrodynamic coefficients values keep being the same in the two different domains: for this reason, used coefficients are the one related to the frequency defined by current sea state as $\omega = 2\pi/T$.

Unfortunately, it is not easy to catch the exact value of frequency, because of the fact that frequency vector has been built with a 0.05 rad/s interval. Despite this, immediately following value to the one of interest has been selected and maintained through the entire simulation time. This kind of procedure represents obviously a little approximation.

In spite of having reduced the equation in an easier to handle one, not all mentioned algorithms are useful in order to get consistent solutions. In facts, integration has to be performed taking into account that wave heights are given as elements of a vector, in which each recorded value is related to a time instant, as described in chapter 3. Thus, some problems arise according to time integration, as they define a time vector in which the solution is computed, which is different from the instants where wave heights are defined. To circumvent this limit, a different integration algorithm has been used: ode4. It is based on the widely known fourth order Runge-Kutta method, an iterative and discretized way through which a numerical approximation of ODEs solution is computed. It is applied to equations with defined initial conditions values (Cauchy's problem), [15]. In particular, initial conditions are represented by buoy position and velocity, defined for each DoF. Cauchy's problem is presented as follows:

$$\begin{cases} x(t_0)=x_0 \\ \dot{x}(t_0)=\dot{x}_0 \end{cases} \tag{4.46}$$

where x_0 and $\dot{x}_0$ values are known and put equal to zero, because of the fact that they refer to a situation in which there is no perturbation of the free surface and hence spar buoy is still at its balance position.

Time integration range is then defined, assuming a small enough Δt in order to get a fine resolution, but not too small to avoid useless increments in computation costs. Once Δt is defined, the integration process can start in order to define solution x. It follows a description of the integration algorithm performed to find the solution at a single time interval.

Working in a discretized domain, equation (4.42) becomes:

$$\frac{\Delta x}{\Delta t}=F(x,t) \tag{4.47}$$

First, each time interval Δt is divided into two further subintervals of same length. Supposing to deal with a single time step, solution at t_n is known and its value at $t_n+\Delta t$ has to be evaluated. This is done calculating a first solution increment at time t_n:

$$\Delta x_1=F(x_n,t_n)\cdot\Delta t \tag{4.48}$$

Then, second and third increments of the solution are computed at time $t_n+\Delta t/2$, including first and second increments respectively:

$$\Delta x_2 = F\left(x_n + \frac{\Delta x_1}{2}, t_n + \frac{\Delta t}{2}\right)\cdot\Delta t \tag{4.49}$$

$$\Delta x_3 = F\left(x_n + \frac{\Delta x_2}{2}, t_n + \frac{\Delta t}{2}\right)\cdot\Delta t \tag{4.50}$$

Finally, one more increment is evaluated at the end of the interval, especially at $t_n+\Delta t$ as

$$\Delta x_4 = F(x_n + \Delta x_3,\ t_n + \Delta t)\cdot\Delta t \tag{4.51}$$

At the end, solution is defined as a weighted average of the four increments, where the central ones Δx_2 and Δx_3, computed at $t_n+\Delta t/2$, influence final solution in a higher way:

$$\begin{cases} t_{n+1} = t_n + \Delta t \\ x_{n+1} = x_n + \frac{1}{6}\left[\Delta x_1 + 2\Delta x_2 + 2\Delta x_3 + \Delta x_4\right] \end{cases} \tag{4.52}$$

This way of integrating motion equation allows to make instants at which wave height is recorded coincide with the integration instants, avoiding any kind of problem related to the not perfect match between the two when using other integration algorithms. In this case, being wave heights defined any 0.001s, integration time step length has been fixed to 0.01s, corresponding to almost 100 points per period in which solution is evaluated.
Of course, solution is computed at half of each time step too, but those values are not returned in solution vector by ode4. Figure 4.12 gives a graphical representation of how the algorithm works.

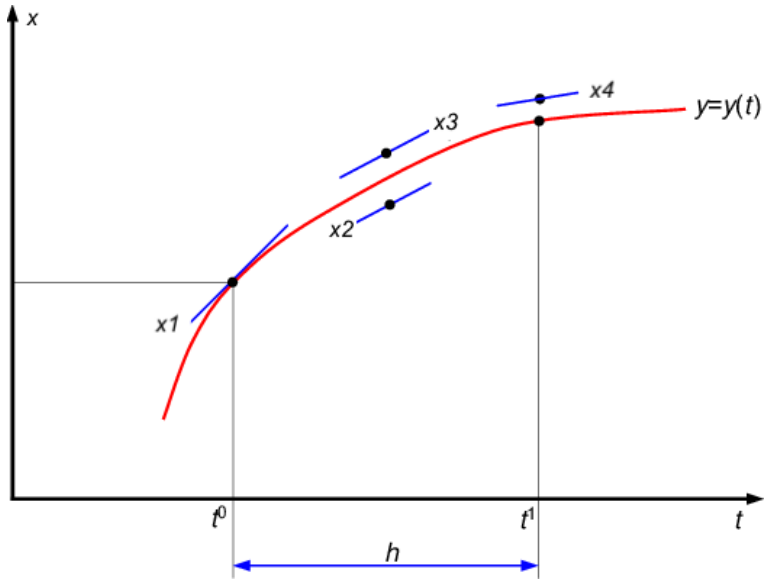

Figure 4.12 Graphic representation of Runge-Kutta discrete method of 4th order [16].

4.4.1 Mooring system

As already presented in chapter 3, a mooring system is added to the set-up. It consists of four metal chains, linked to the cylindrical buoy through a circular plastic ring applied on the body itself, and fixed to the bottom. As shown in Figure 3.03 and Figure 3.04, the catenaries are anchored at the four nodes of a rectangular base.
The latter are applied in order to reduce oscillations and to maintain the body around its prescribed position, bringing in new forces due to the chains tensions that arise at the moment in which the chain itself experiences a displacement from its initial position. This represents the principal goal of this catenary mooring system, and its action has possibly to be performed avoiding the situation in which catenaries are pulled to their maximum length. If this happens, the mooring system is normally well designed.
Considering the three DoFs that have been taken into account (surge, heave, pitch), it is easy to understand that buoy motion can happen in the (x-z) plane only: this leads to the conclusion that mooring could be modelled considering two chains in the prescribed plane only, one upstream and one at the wake of the buoy.
Despite the possibility of this simplification, accurately modelling this kind of mooring system is still a very difficult matter to have to deal with and its development goes beyond this work purposes, as this mathematical model has the aim of understand from a preliminary point of view the specific laboratory setup and buoy movement under the action of a certain sea state.
For these reasons, the mooring system has been modelled as follows, through the use of two calibration coefficients defined while comparing the buoy motion coming from laboratory video analysis and the results coming from the mathematical model implemented on Matlab.

Mooring system influence on the buoy motion can be of two different sorts depending on the solicitation characteristics. Catenaries can be stretched through their whole length when solicitation is high enough or not be stretched at all but working in such a way that they influence the buoy motion as well, because they experience a displacement from their initial position and they are so put in tension anyway. It follows the description of how these two different mechanisms have been modelled.

When incident wave is high enough to stretch catenaries to their whole length (this happens in the case R10), since they are characterized by negligible weight compared with the buoy, they have been modelled taking into account their action at the moment in which buoy position is far enough from the initial one to tight the chains. Since the latter stiffness when they are totally stretched, they make the buoy immediately stop avoiding any further movement further from that position. In order to model this situation, an *end-stop mechanism* has been implemented. Through this mechanism a very high stiffness is associated to the chains when they get tight, while a null one is associated to any other situation. In mathematical terms, the mooring system is represented by the F_{moor} function (4.53), created separately in a dedicated Matlab script. As F_{moor} depends on the buoy position at each instant of simulation, it is function of time too.

$$F_{moor}(t)=\begin{cases} -K_{moor}\,[y(t)-Y_{lim}], & \text{when } |y(t)|\geq Y_{lim} \\ 0, & \text{otherwise} \end{cases} \tag{4.53}$$

where:

- K_{moor} is constant representing mooring stiffness;
- Y_{lim} represents the length of a single chain and acts as a limit for buoy position (35cm);
- $y(t)$ is the distance of the buoy from the point in which the chain is anchored.

Relative position of the buoy y(t) has been computed considering both position as function of time, and the relative distance between the anchored point and the initial buoy position. In this way, it is possible to compare the chain length and the effective position of the buoy, in order to apply condition (4.53). In particular, distance y(t) has been defined as

$$y(t)=\sqrt{(x(t)+x_0-x_1+d_1\cdot\sin\theta(t))^2+(z(t)+z_0)^2+(d_0)^2} \quad (4.54)$$

where x(t) and z(t) represent buoy position as function of time, respectively along horizontal and vertical direction, referred to the initial position in surge and heave mode respectively, while x_0, z_0 and d_0 takes the role of the coordinates of the buoy with respect to the anchored point of the chain: in particular d_0 is the horizontal distance from the anchored point of the chain at the bottom to the buoy. The distance d_1 represents the length measured from the centre of rotation of the object and the point in which catenaries are hooked to the body. Parameter x1 represents the difference between the centre of gravity horizontal coordinate and the chain end, and it is evaluated as buoy radius.

The value of stiffness constant K_{moor} has been selected through a calibration process as to find the correct value of stiffness that best represents the real effect that mooring has on the buoy.

When the incident wave happens to be small enough to avoid previous situation, mooring system cannot be modelled through the same function because of the fact that it is not totally stretched and the condition about *y(t)* would always get to a value of K_{moor} equal to zero and then catenaries effect would not be represented by the model.
So, when this happens, mooring system is modelled representing its effect as a sum of two contributions: a damping and a stiffness.
The damping term has been modelled in the same way as the damping contribution due to the radiation phenomena, so through the coefficient K_{damp} multiplied by a velocity, which in particular is the velocity of the buoy for each DoF, as follows:

$$\bar{F}_{damp}(t) = \bar{K}_{damp}\cdot\bar{u}(t) \quad (4.55)$$

where u(t) is a 3x1 vector containing the three components of velocity along each DoF. Being velocity function of time, the whole damping term will be defined at each instant as well.
Damping force exerted by the chains is in particular responsible for a motion amplitude reduction or increase with respect to the member sign.

The stiffness member has a similar structure as the one of the damping term, with the constant K_{stiff} that multiplies a position:

$$\bar{F}_{stiff}(t) = \bar{K}_{stiff}\cdot\bar{x}(t) \quad (4.56)$$

where x(t) is a 3x1 vector containing the three components of position along each DoF. Being position function of time, the whole stiffness term will be defined at each instant as well.

The mooring effect is then modelled as the sum of the latter two contributes with the addition of the end-stop mechanism that works anytime catenaries are stretched. The following equation recalls the final total force F_{MS} through which mooring system is modelled at any situation:

$$\bar{F}_{\mathrm{MS}} = \overline{K}_{\mathrm{stiff}} \cdot \bar{x}(\mathrm{t}) + \overline{K}_{\mathrm{damp}} \cdot \bar{u}(\mathrm{t}) + \bar{F}_{\mathrm{moor}} \tag{4.57}$$

All the previous expressions concerning mooring system are expressed taking into account one single DoF.
At the end, the final version of the ordinary differential equation (ODE) representing buoy motion along the three considered DoFs, including mooring system effect, is defined in the following expression:

$$\left(\overline{\overline{\mathrm{M}}}+\overline{\overline{\mathrm{C_a}}}(\omega)\right)\cdot\ddot{\mathrm{x}}(\mathrm{t}) = \overline{\mathrm{f_{exc}}}(\omega)\cdot\eta(\mathrm{t}) - \overline{\overline{\mathrm{R_d}}}(\omega)\cdot\dot{\mathrm{x}}(\mathrm{t}) - \overline{\mathrm{K_{damp}}}\cdot\dot{\mathrm{x}}(\mathrm{t}) - \overline{\mathrm{K_{stiff}}}\cdot\mathrm{x}(\mathrm{t}) - \overline{\overline{\mathrm{KH}}}\cdot\mathrm{x}(\mathrm{t}) - \bar{F}_{\mathrm{moor}} - \frac{1}{2}\rho\mathrm{A}\overline{\mathrm{C_d}}\cdot|\dot{\mathrm{x}}(\mathrm{t})|\cdot\dot{\mathrm{x}}(\mathrm{t}) \tag{4.58}$$

As for coefficient K_{moor}, K_{damp} and K_{stiff} are evaluated through a calibration process too. Final values of the coefficients are reached for each test, hence for each experimental wave, and along every DoF too. In particular the calibration process consists of imposing different values of the calibration coefficients at each wave and DoF until the model results, both in time and frequency domain, best fit the laboratory ones. Acting with different coefficients at each wave and DoF, allows to define the trend taken by the coefficients against wave height.
While K_{moor} is related to all the DoFs and maintains the same value due to the fact that its action has to practically reply the effect that catenaries have on the buoy once they reach their maximum extension, K_{damp} and K_{stiff} do not keep being the same at each DoF. The reason why this happens is related to the forces that the mooring system has to fight against and to the different resistance that the catenaries exert along different directions. In fact, the forces exploited by the catenaries are related to the displacements experienced by the chains. When the displacement grows, and the chain becomes more stretched, the exploited force grows as well. In chapter 5, where results will be presented, the values assumed by these coefficients will be discussed in a more precise way according to the other simulation characteristics.

4.4.2 Outputs of time domain model running

The model simulation returns as result a series of vectors gathered in two matrixes: $\bar{x}$ contains the position vectors, the ones which contains the position that the buoy occupies at each simulation instant along each DoF while $\dot{\bar{x}}$ is formed by the buoy velocitiy vectors along each DoF. Both have dimension 3xTspan, where Tspan stands for the number of simulation instants. The result expressed in this form is then split in six different vector of dimensions 1xTspan, as to achieve an easier handling:

- x_buoy: position of the buoy along surge motion;
- z_buoy: position of the buoy along heave motion;
- r_buoy: rotation of the buoy along pitch motion;
- vx_buoy: velocity of the buoy along surge motion;
- vz_buoy: velocity of the buoy along heave motion;
- vr_buoy: angular velocity of the buoy along pitch motion;

4.5 Post-processing in frequency domain

After the obtained results are compared with the laboratory ones, a frequency analysis on the position vector has been performed on order to compare the oscillation frequency of the model motion and the one related to laboratory one.
The passage from time domain to frequency domain is performed through the application of the Matlab function "Fast Fourier Transformed" (fft), directly applied to the vectors themselves. Having to deal with vectors resulting from the resolution of the equation of motion in time domain, nonlinear forces effect is not cut out and it is possible to define a more precise frequency behaviour of the body than the one obtained through the computation of the RAO, performed in section 4.3.2, [17], [18].

The vector resulting from Fast Fourier Transformed application is then modified in order to obtain a function of frequency representing the real signal amplitude called P1, expressed in [m].
This requires the definition of a vector of frequencies f inside which motion amplitude is observed. Then, as to reach the real motion amplitude, vector P2 is first computed and hence vector P1 expression is derived:

$$P_2 = \mathrm{abs}\left(\frac{X}{L}\right) \tag{4.59}$$

$$P_1 = P_2(1{:}L/2) \rightarrow \quad P_1 = 2{*}P_1 \tag{4.60}$$

where X represent the Fourier transformed of the original vector, L is the length of the vector itself and P_1 is the final result, so the vector of real motion amplitudes along frequency. P_1 is described in an interval of length L/2 because of the fact that Fourier transformed X is symmetric with respect to half the domain length L.
At the end, both X and P1 are plotted against frequency vector to better understand their behaviour in frequency domain.

This kind of analysis, after the resolution of the equation of motion in time domain, represents a quite precise way to describe frequency behaviour of the body because of the fact that it includes nonlinear effects too.
The peak frequency that is expected to assess in this section is very similar to the wave frequency: in fact, unless the solicitation has a too high frequency, it always occurs that the body moves with the same frequency of the wave.

4.6 Free decay test

Free decay tests are particular kind of simulation in which no incident wave is present and hence none kind of excitation force is provided to the body. The free surface is flat and the only perturbation it undergoes is due to the motion of the body (radiation contribution), moving from an initial position which is different from its balance one. Once the body itself is released it tends to oscillate until equilibrium is reached. Free decay test is useful in order both to assess a body natural frequency and study the amplitude of oscillations of its own motion while moving searching its balance configuration, [19, 24].

A free decay test has been performed in order to assess natural frequency of the buoy for what heave DoF is concerned and, being the aim of this work the construction of a model representing a buoy motion, to compare the model free decay results with the experimental simulation performed in laboratory as well in order to evaluate the reliability of the model itself.
Free decay test has been conducted imposing flat free surface along the entire simulation time, in particular a null wave height (H=0) has been set in order to represent this condition. Furthermore, a long enough test time has been imposed as to catch motion decay the best way possible and hydrodynamic coefficients for a very low frequency have been computed with the use of function Nemoh, starting from the same mesh defined through the sensitivity analysis. It is not actually fundamental to compute every hydrodynamic coefficient for null frequencies because most of them already assume an asymptotical behavior when approaching low frequencies. Nevertheless, in this case, not every coefficient has an asymptotical behavior, so they have been again computed assuming a frequency range

equal to [0.05 : 0.05 : 4.00], which trend is plotted in chapter 5 Figure 5.57, with all the other results of the model.

Finally, initial conditions have been introduced in order to define an initial state representing a starting position of the buoy which is different from its balance configuration. Initial state has been defined through the following condition:

$$z_0 = -0.04 \text{ m (heave)} \tag{4.61}$$

It does not make sense to impose a different initial condition from the null one for what surge motion is concerned, because any surge oscillation arises when no excitation force due to the waves is provided.
When simulation begins the buoy starts oscillating along the vertical direction. The amplitude of the oscillation decreases until the balance configuration is assessed according to a particular frequency: the natural one. Each DoF has its own motion natural frequency which is assessed through a frequency analysis performed the same way as described in section 4.5.
Frequency analysis is very useful in free decay as well, because, as already said, on one hand it is possible to compare model and laboratory results both in time and frequency domain. On the other hand, it enables to catch natural frequencies considering the whole amount of acting forces, both linear and nonlinear, and this brings to a more precise result than the one achieved through the computation of RAO coefficient. It is then worth to compare the two latter natural frequency values results.

As for all the other wave cases, laboratory tests have been recorded and analyzed. The comparison between model and laboratory results will be developed in chapter 5.

5

Results

In this chapter, all the results of the model concerning both frequency and time domain will be presented, paying particular attention to the comparison between the model and the laboratory results, in order to verify the reliability of the model itself.
Furthermore, the values of the calibration coefficients inserted in the mathematical model in order to obtain such results will be reported and their values plotted against wave height. In this way, the trend taken by the coefficients against wave height can be easily understood.

5.1 Frequency domain results

The aim of the frequency domain part of the code is to compute consistent values for the hydrodynamic coefficients that are later used in the time domain part.
As already explain in chapter 4, this is done through the application of a sensitivity analysis on the mesh elements. Taking into account Figure 4.06, Figure 4.07, Figure 4.08 and Figure 4.09, although in surge case 20x600 grid represents a good mesh solution, in heave and pitch cases this is not as precise as well. Hence, it has been chosen to proceed with the adoption of 20x700 mesh for all three DoFs. Once the choice of the mesh is made, final RAO and hydrodynamic coefficients can be definitely assessed. Their plots are shown in Figure 5.01 and Figure 5.02 respectively.

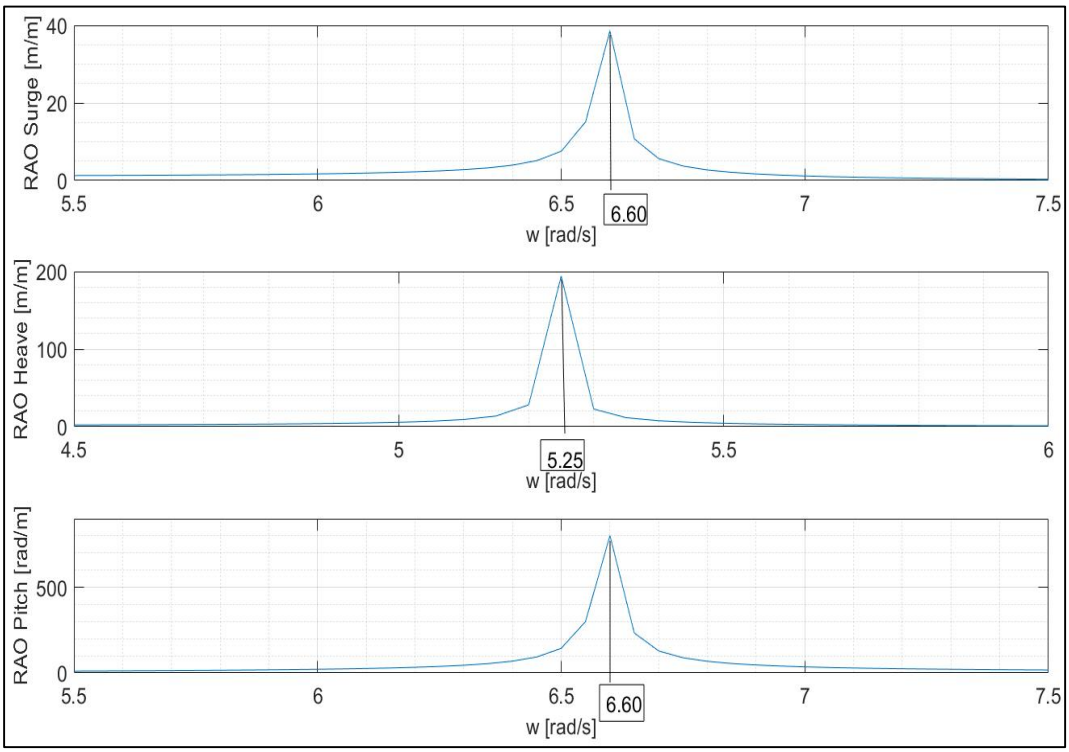

Figure 5.01 RAOs after the choice of the final mesh (20x700).

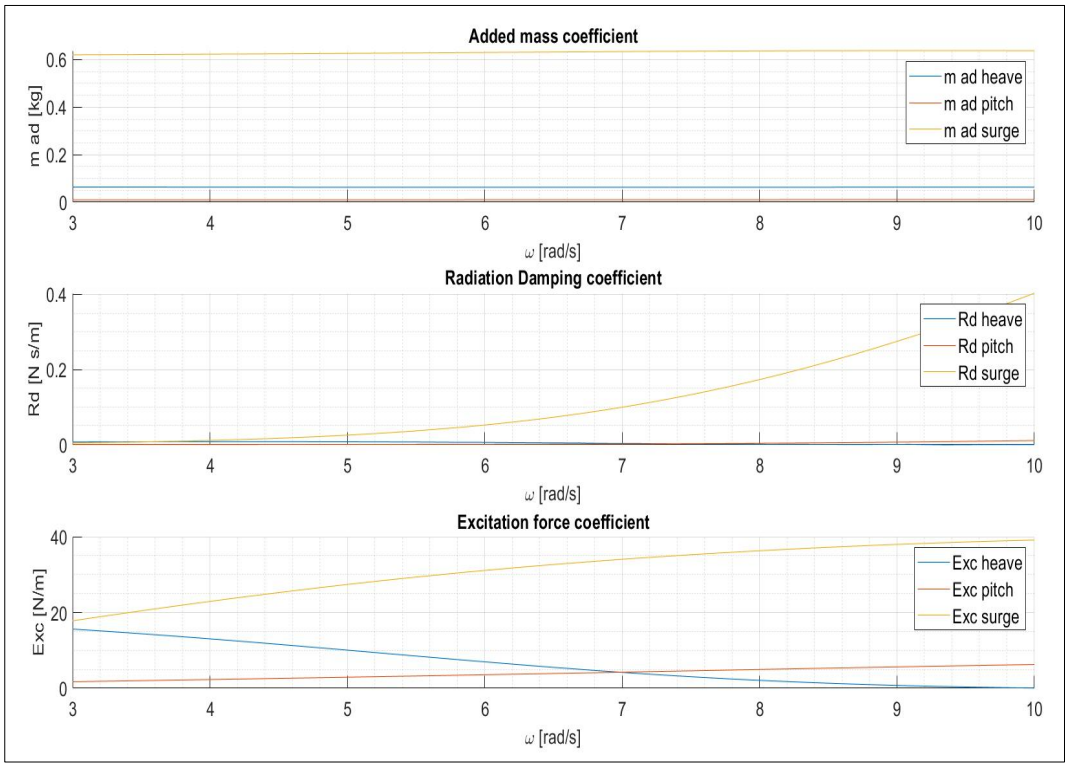

Figure 5.02 Added mass, radiation and excitation force coefficients for each DoF and for 3-10 rad/s frequency interval.

Hydrodynamic coefficients plot shows that added mass coefficients tend to maintain constant values throughout the frequency domain. Radiation coefficients tend to a very small value at low frequencies, but, while heave and pitch ones keep being small, the surge coefficient increases. This could be explained because of the fact that, being the buoy a slender body, influence areas are different if we consider vertical or horizontal section, and the vertical one is bigger than the other. Being vertical section linked to surge motion bigger than the horizontal one, it is then possible to understand that it can have a bigger influence on free surface while perturbing it, during the object motion. Excitation force coefficients do not reach constant values inside the frequency interval. This is the reason why smaller frequency value will be adopted in order to compute once again the coefficients for what the free decay test is concerned. All the coefficients values are quite low because of the small dimensions of both waves and buoy.

From RAO plots it is possible to assess the value of the resonance frequency, the one corresponding to the peak of function RAO itself. Resonance frequency represents buoy natural frequency too, and it should be the same value determined performing a free decay test. Nevertheless, as already considered, RAO is not a very accurate instrument in order to investigate body motion characteristic, for the reason exposed in section 4.3.2. Hence, real resonance frequency values could be a little bit different, but RAO still keeps being a useful tool for a preliminary analysis. The same thing can be said for the amplitude that RAO indicates, as it represents the ratio between wave oscillation amplitude and the wave amplitude. In fact, not being all the real acting forces involved brings to a not meticulous evaluation, but again, still valid for a first overview.

5.2 Time domain results

As explained in chapter 4, the part of the model concerning the mooring system needs a calibration process. In particular, the calibration process consists in finding the values of the coefficients K_{stiff} and K_{damp} through which the cylindrical buoy oscillation matches quite accurately the oscillation recorded by the laboratory video analysis. This procedure has been carried out for each wave test and for each of the three DoFs too. In this section, the plots of the results will be shown in time domain and the values of the calibration coefficients will be reported for each wave and DoF case. Together with the time domain plots, a frequency analysis of the results has been carried out, in order to better understand the comparison.
Before introducing the results, a clarification on the calibration coefficients must be done. The role of the calibration coefficients is to complete the part of the model related to the mooring system, modelled as the sum of a stiffness and a damping term. The catenaries

weight has been taken as negligible, and hence little oscillations along vertical direction produce very small forces exploited by the chains. The action of the mooring system is particularly evident along horizontal direction, due to the slightly asymmetrical form of the generated waves, phenomenon that induce the cylindrical buoy to experience a shift from its initial position (as better described in chapter 3). Consequently, catenaries exploit not negligible forces in order to avoid this shift. For these reasons, the only calibration coefficients that produce evident effects on the model are the one associated to the surge motion.
Then, from now on, K_{damp} and K_{stiff} will only be referred to as the calibration coefficients acting on surge direction and hence occupying the surge spot in the (1x3) vectors defined by $\overline{K_{damp}}$ and $\overline{K_{stiff}}$, while all the other spots are supposed to host null values, as represented in expressions (5.01) and (5.02):

$$\overline{K_{damp}} = [K_{damp} \quad 0 \quad 0] \tag{5.01}$$

$$\overline{K_{stiff}} = [K_{stiff} \quad 0 \quad 0] \tag{5.02}$$

In the next paragraphs, the results will be presented for each wave test separately, and inside each wave test every DoF will be discussed on its own. While from wave R03 to wave R08, including R05, R06 and R07, the wave characteristics allow to keep the mooring system working in normal conditions (catenaries are not totally tight), wave R10 presents very high wave height compared with the other ones, with consequent pulling of the catenaries. So, for what the first group of waves is concerned, the calibration coefficients are determined in such a way to prevent buoy shift along surge direction and that the end-stop mechanism (introduced in equation (4.53)) is not activated, while in R10 its effect plays a very important role.

5.2.1 Free decay results

Free decay test is the first one to be performed. As introduced in chapter 4, in this kind of test no perturbation of the free surface comes from the wave generator, but the only one that is created is due to the radiation phenomenon. The test is conducted making the cylinder oscillating from the starting configuration in which the upper surface of the body is placed at free surface level. During the laboratory test, it is clearly visible that the catenaries are not stressed for what surge DoF is concerned because of the fact that there are no active waves contributing to buoy horizontal shift, and the only oscillation verifies along vertical direction. So, according to what has been written in the previous paragraphs, most of the mooring action is not present in this test, being that no surge forces take place. For what vertical direction is concerned, very little forces are exploited by the mooring

system, also considering its negligible weight. For this reason, all the coefficients are inserted in the model as null values, as shown in Table 5.08.
Furthermore, the results are assessed through the application of the particular hydrodynamic coefficients described in section 4.6. They have to represent the situation of static free surface, practically intended as a wave with infinite period and hence they are captured at very low frequency, near to 0 rad/s. The one linked to a frequency equal to 0.05 rad/s have been taken into account for the calculations of the results. Figure 5.03 represents the trend of the hydrodynamic coefficients inside the interval 0.05 – 4.05 rad/s.

Figure 5.04 and figure 5.05 show the results of the model compared to the laboratory one, and in particular the free decay of the cylindrical buoy along vertical direction. The very low incidence of the catenaries makes it possible to put the values of the calibration coefficients as null, avoiding the forces due to the mooring system. The model performs in a quite good way, especially considering the frequency of the oscillation.

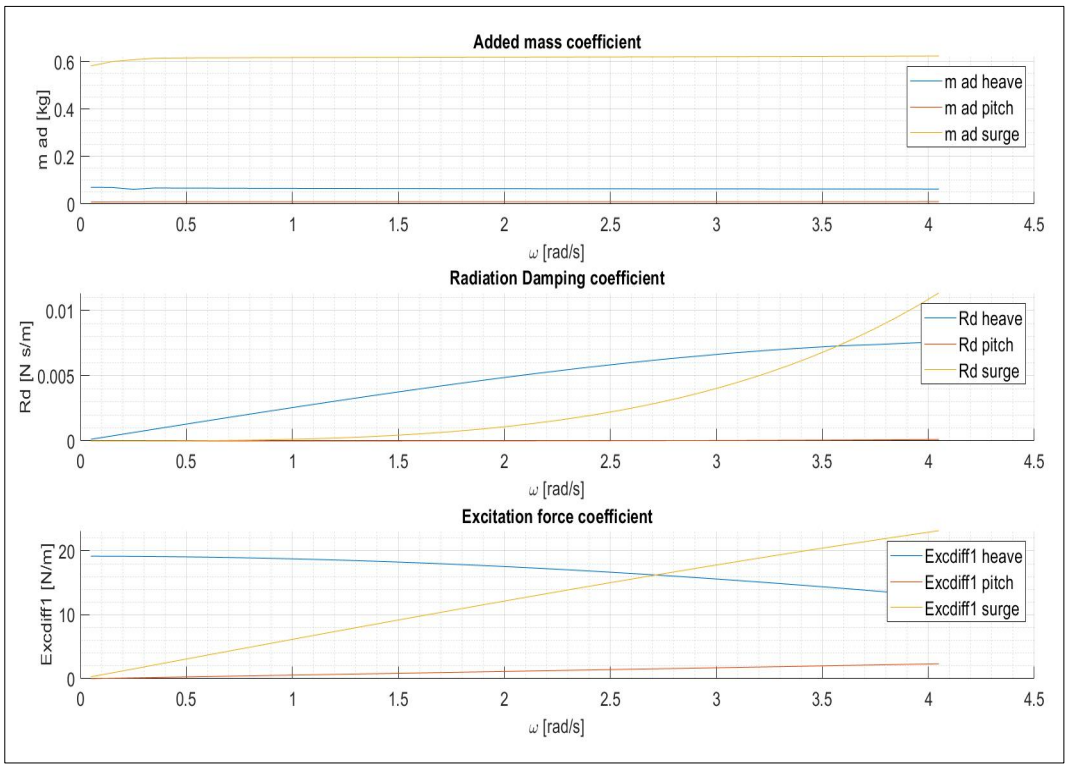

Figure 5.03 Hydrodynamic coefficients for free decay test (frequency interval 0-4 rad/s).

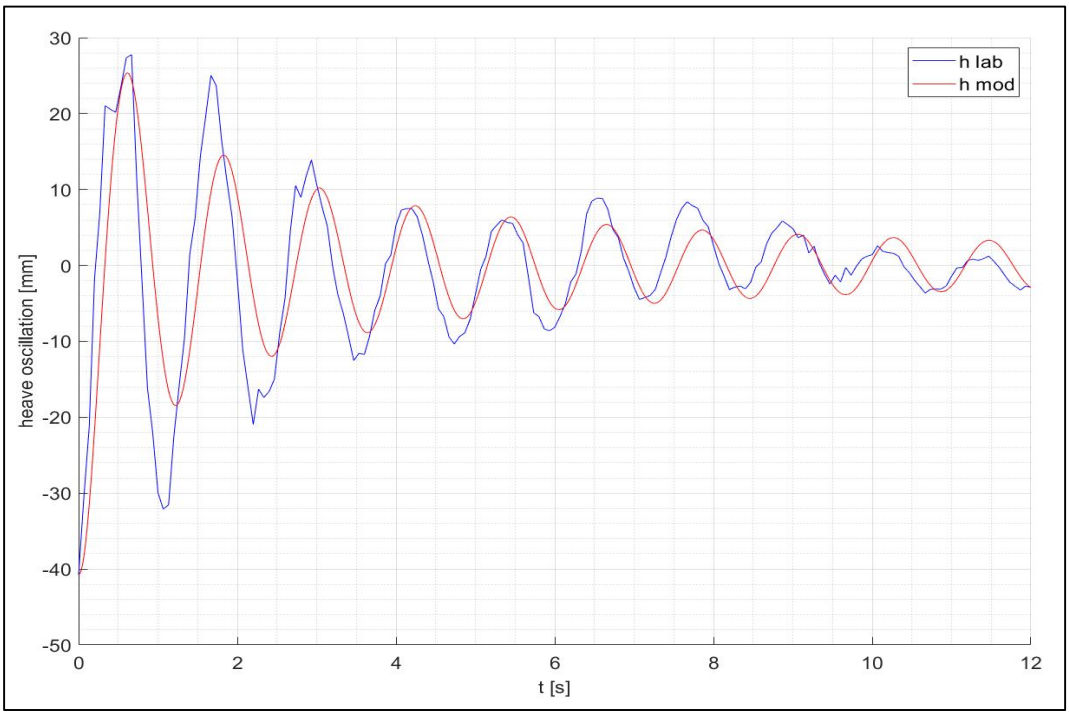

Figure 5.04 Free decay HEAVE oscillation along with simulation time (starting configuration: z=-40 mm).

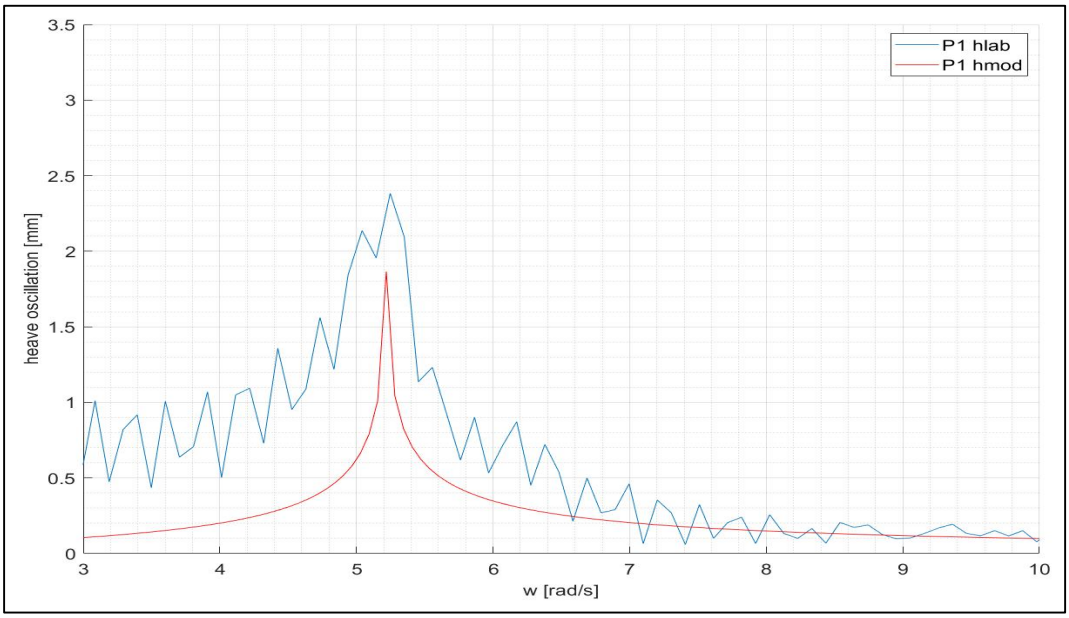

Figure 5.05 Frequency analysis of the comparison between model and laboratory HEAVE results for free decay test.

	surge	heave	pitch
K_{damp}	0	0	0
K_{stiff}	0	0	0

Table 5.08 Calibration coefficients for free decay test.

A particular result coming from the free decay test is the value of the frequency of oscillation, which correspond to the natural oscillation frequency of the body. The natural frequency derived from this free decay test is equal to 5.29 rad/s, as it is possible catch from Figure 5.61. This important value of frequency is related to the concept of resonance: as introduced while talking about RAO, the resonance condition is achieved when the wave frequency matches the body natural frequency and produces the higher oscillation possible. Considering RAO operator of Figure 5.01, heave resonance frequency is equal to 5.25 rad/s, very similar to the natural frequency detected during free decay test. This agreement between the two values of natural frequency figured out from both the frequency (with RAO operator) and time domain represents a good result for what model reliability is concerned. The small difference between the two frequency values is due to the fact that drag force is not taken into account while performing the RAO calculation, being it a nonlinear term.

5.2.2 Wave R03

As introduced in section 3.3.1, this wave is the smaller among the tested ones, both in wave height and length, with correspondent relatively small buoy motion. Heave motion is particularly small and noise is very evident in the signal coming from the video analysis. For this reason, it has been chosen neither to perform any calibration for what this DoF is concerned nor to report the results. Despite this, both surge and pitch results are reported in this section.

Surge motion (R03)

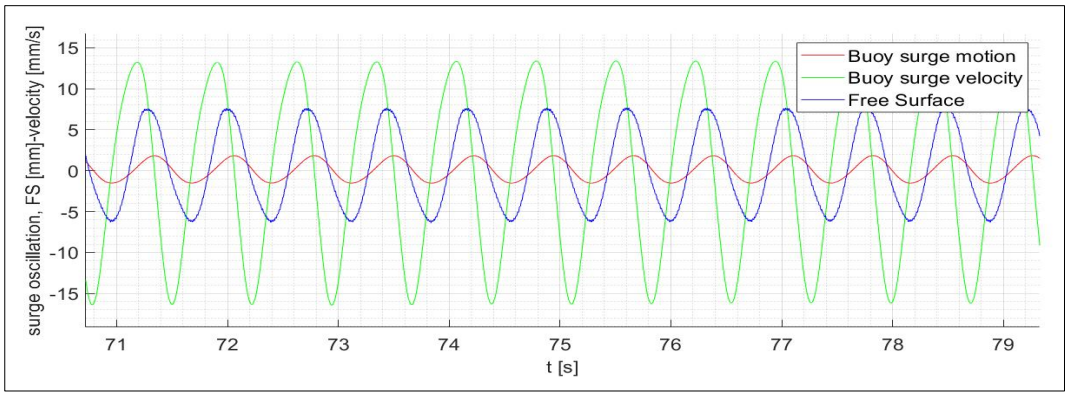

Figure 5.06 SURGE model oscillation, velocity and free surface deformation against time for wave R03.

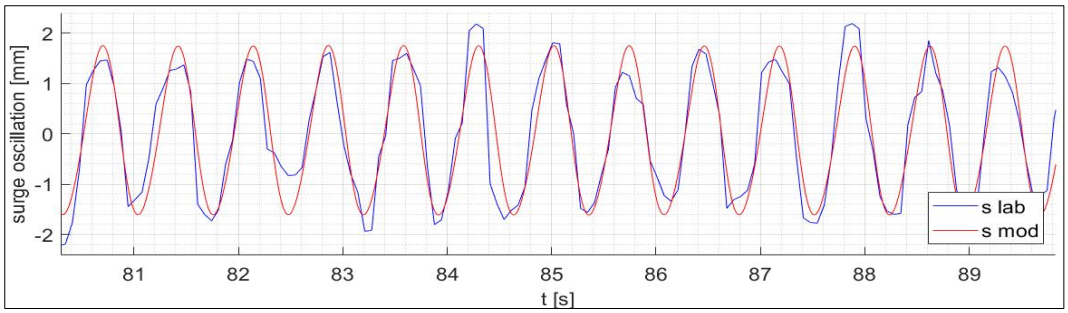

Figure 5.07 Comparison between model and laboratory SURGE results for wave R03.

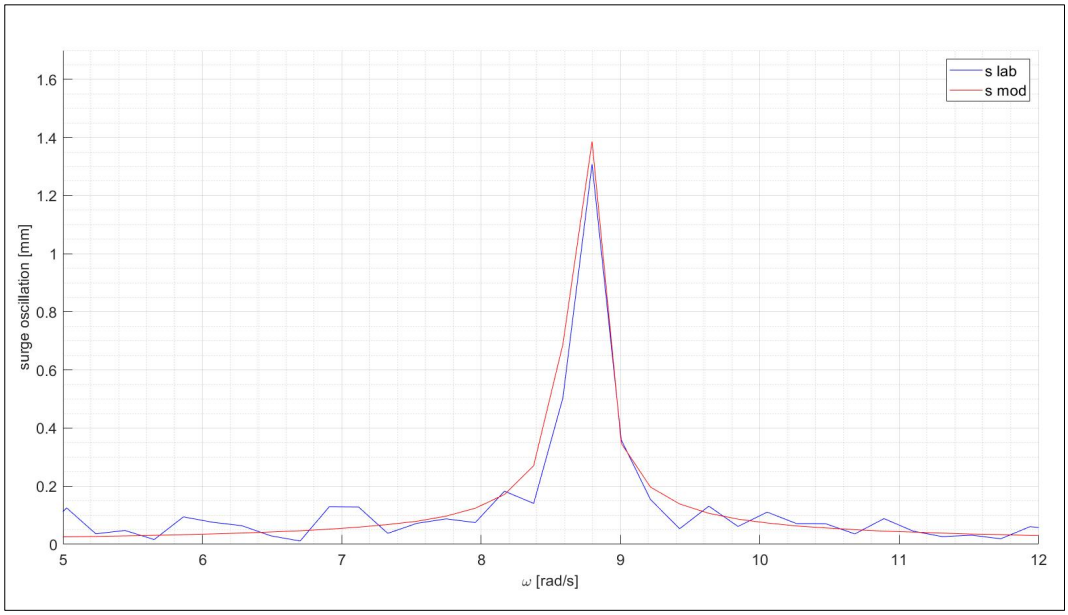

Figure 5.08 Frequency analysis of the comparison between model and laboratory SURGE results for wave R03.

Pitch motion (R03)

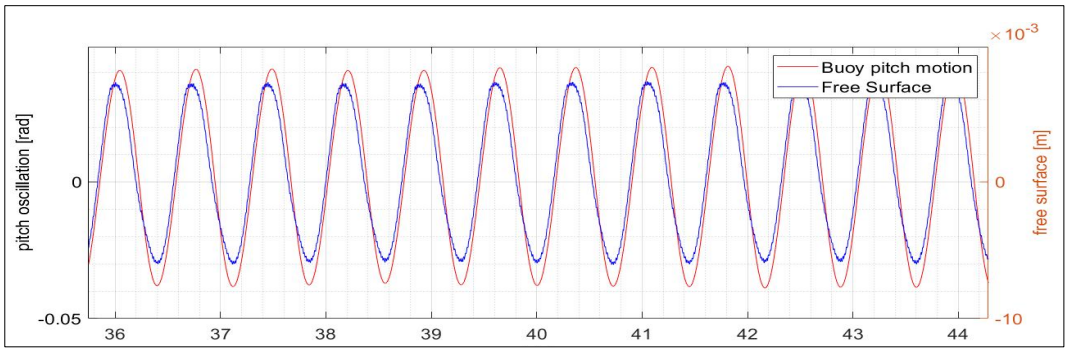

Figure 5.09 PITCH oscillation and free surface deformation against time for wave R03.

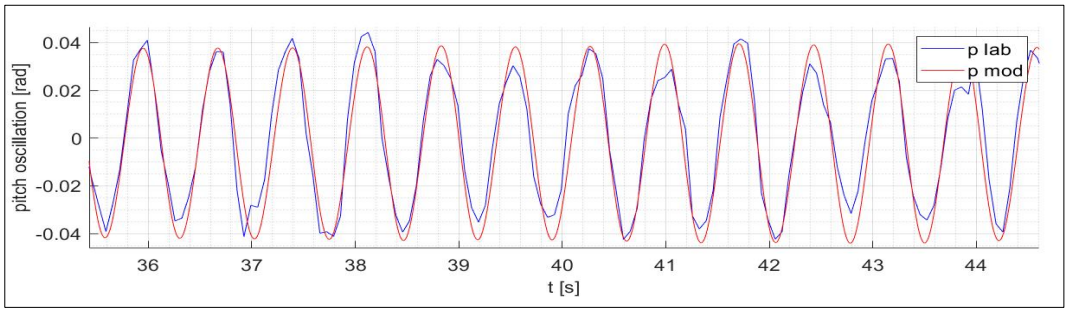

Figure 5.10 Comparison between model and laboratory PITCH results for wave R03.

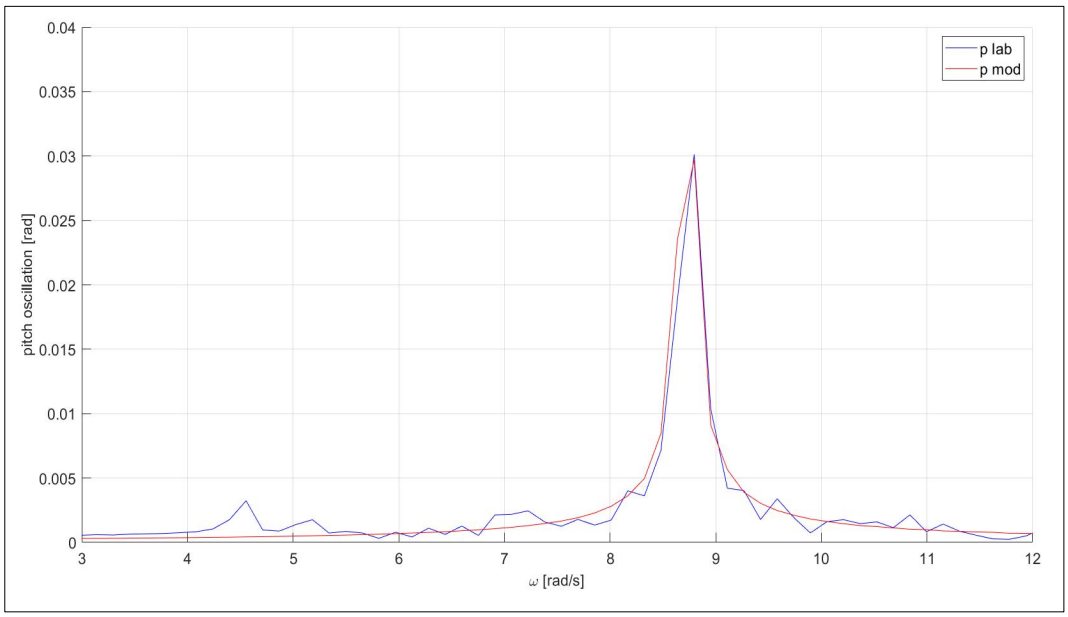

Figure 5.11 Frequency analysis of the comparison between model and laboratory PITCH results for wave R03.

The calibration coefficients inserted in the model in order to obtain previous results are shown in Table 5.01.

	surge	heave	pitch
K_{damp}	4.5	/	0
K_{stiff}	245	/	1.05

Table 5.01 Calibration coefficients for wave R03.

5.2.3 Wave R05

Wave R05 is the second wave that has been recorded by the GoPro cameras and the signal coming from the video analysis are not too much influenced by noise. Once again, surge and pitch motion laboratory results are quite regular, while heave ones present some noise disturbing the signal. Although this disturbance takes place, the amplitude of the oscillation is higher than the one related to R03, then its effect is not as big as in the previous case. From now onward, the calibration process is applied on heave motion as well as on surge and pitch ones.

Surge motion (R05)

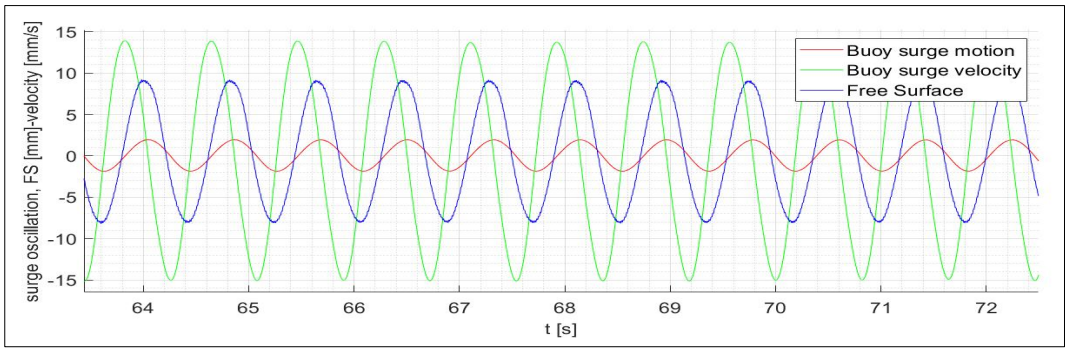

Figure 5.12 SURGE model oscillation, velocity and free surface deformation against time for wave R05.

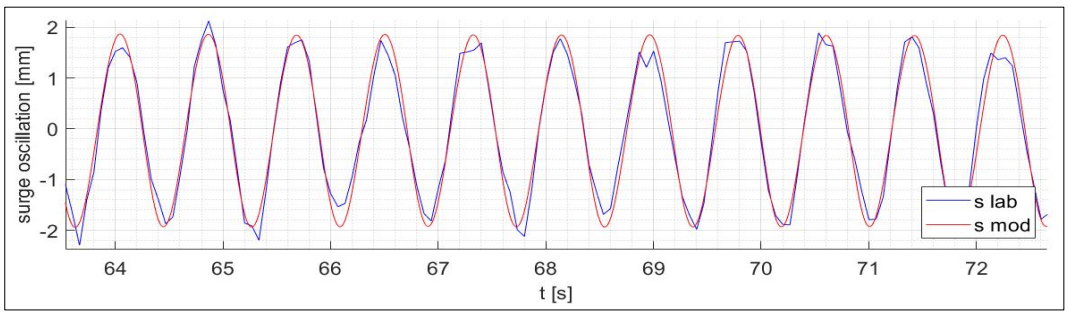

Figure 5.13 Comparison between model and laboratory SURGE results for wave R05.

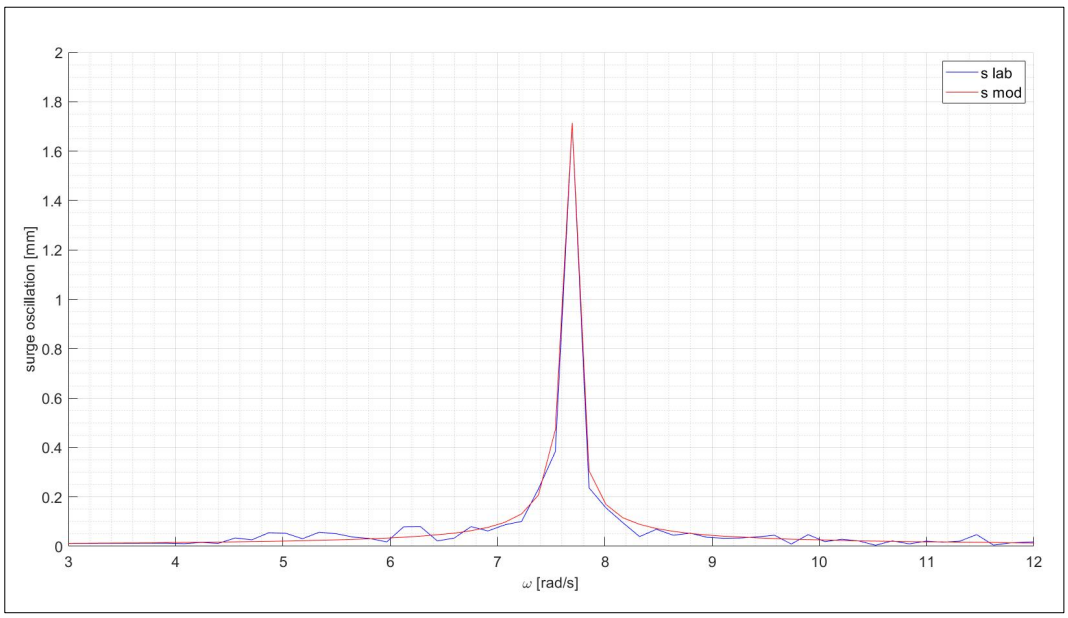

Figure 5.14 Frequency analysis of the comparison between model and laboratory SURGE results for wave R05.

Heave motion (R05)

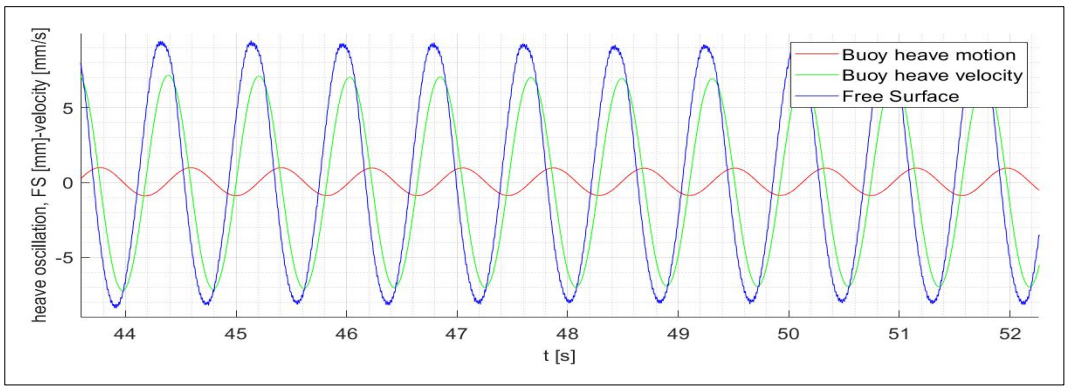

Figure 5.15 HEAVE model oscillation, velocity and free surface deformation against time for wave R05.

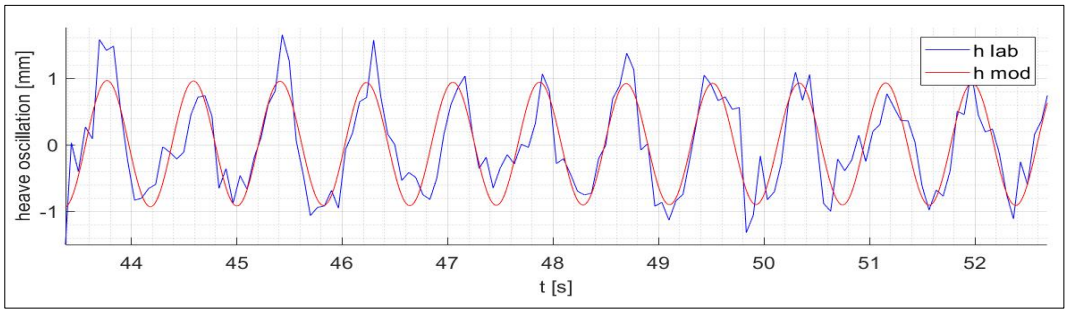

Figure 5.16 Comparison between model and laboratory HEAVE results for wave R05.

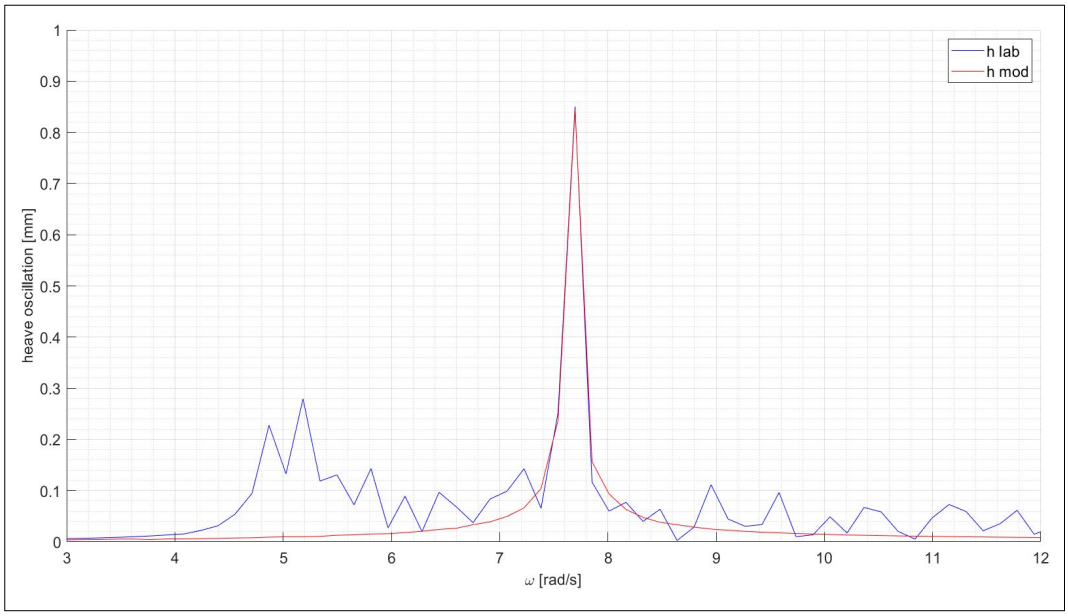

Figure 5.17 Frequency analysis of the comparison between model and laboratory HEAVE results for wave R05.

Pitch motion (R05)

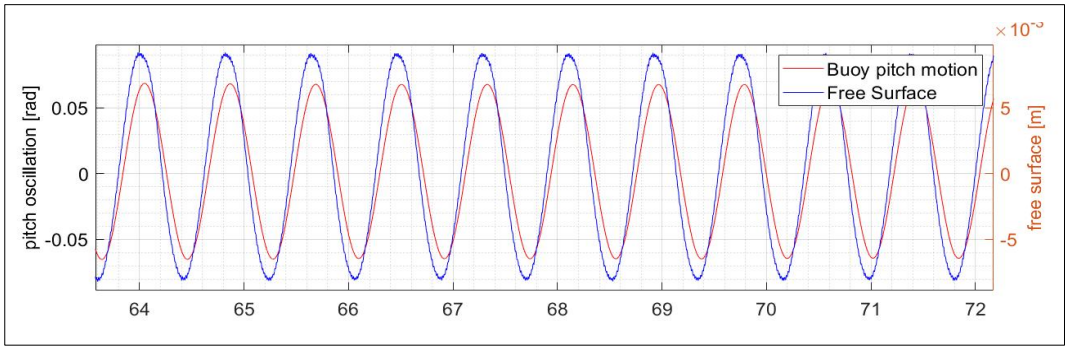

Figure 5.18 PITCH oscillation and free surface deformation against time for wave R05.

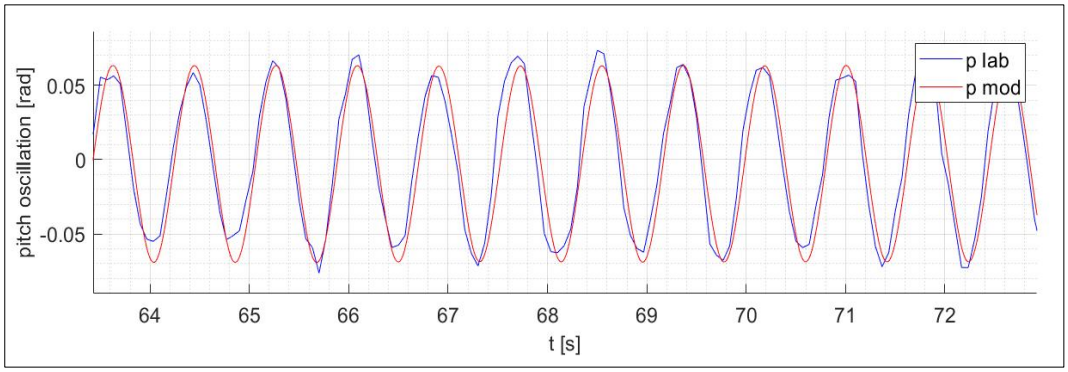

Figure 5.19 Comparison between model and laboratory PITCH results for wave R05.

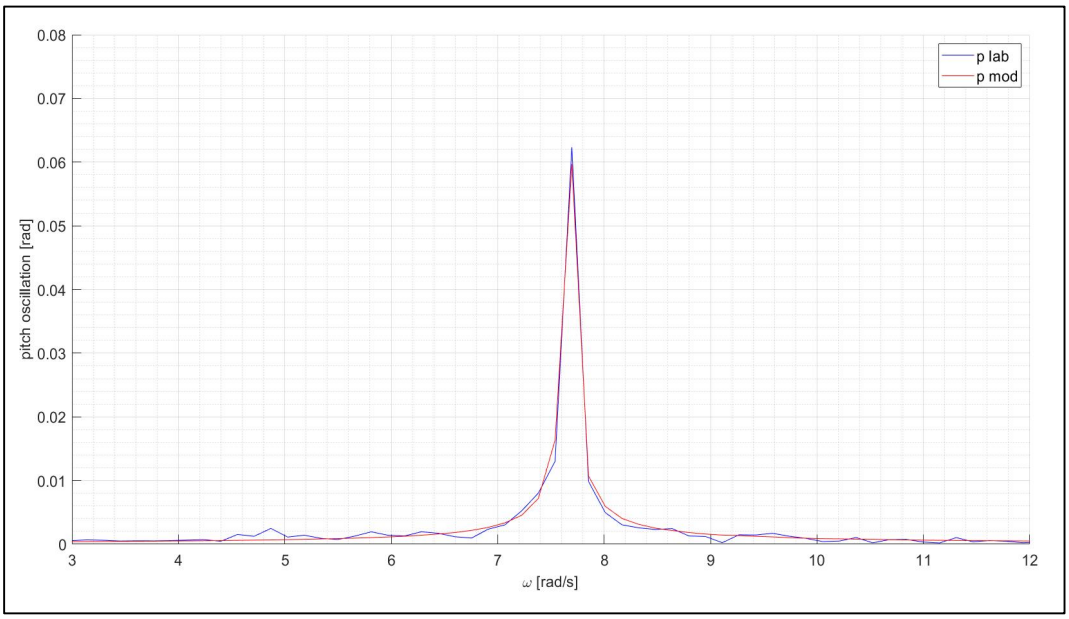

Figure 5.20 Frequency analysis of the comparison between model and laboratory PITCH results for wave R05.

The calibration coefficients inserted in the model in order to obtain previous results are shown in Table 5.02.

	surge	heave	pitch
K_{damp}	4.4	2.8	0
K_{stiff}	233	10	0.63

Table 5.02 Calibration coefficients for wave R05.

5.2.4 Wave R06

Surge motion (R06)

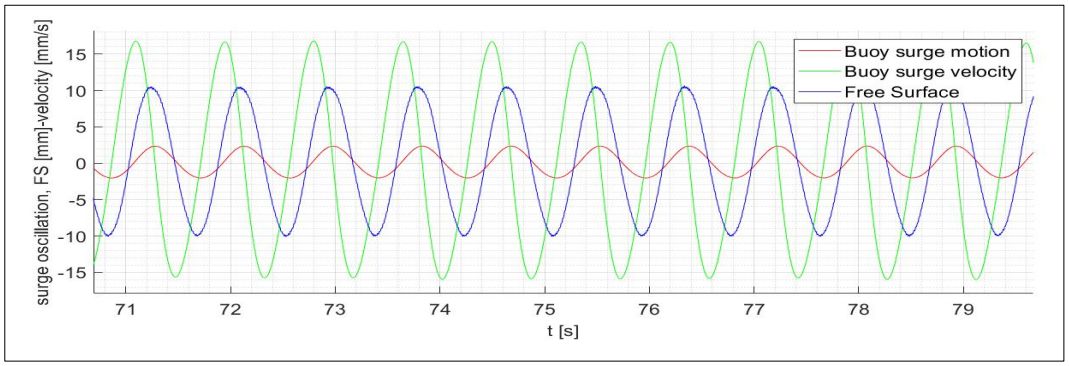

Figure 5.21 SURGE model oscillation, velocity and free surface deformation against time for wave R06.

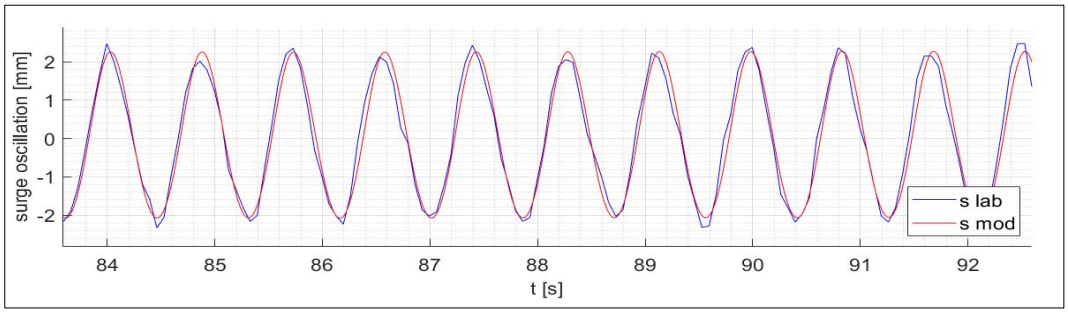

Figure 5.22 Comparison between model and laboratory SURGE results for wave R06.

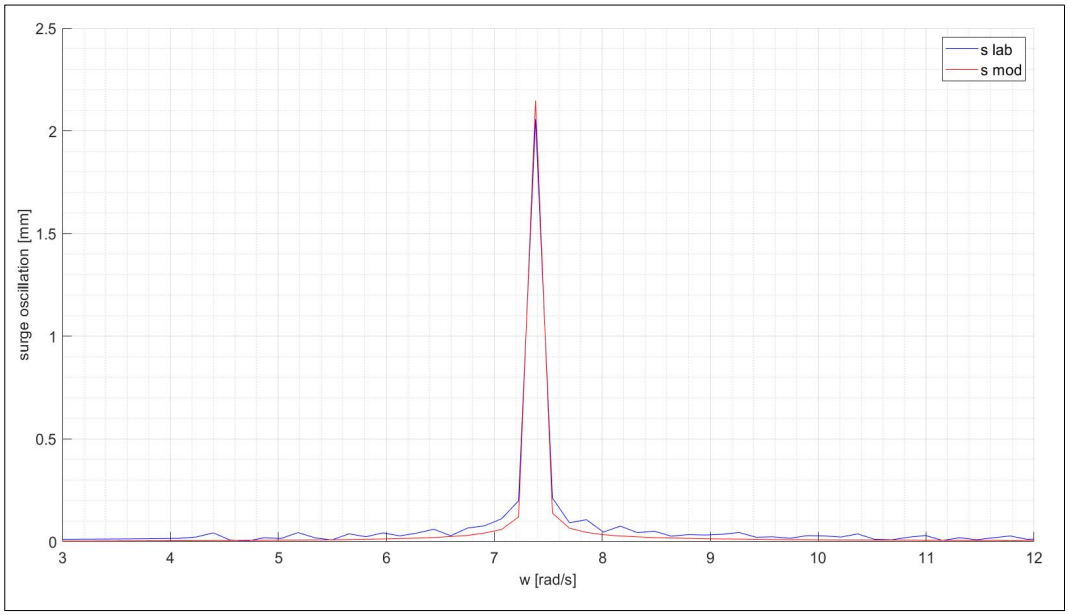

Figure 5.23 Frequency analysis of the comparison between model and laboratory SURGE results for wave R06.

Heave motion (R06)

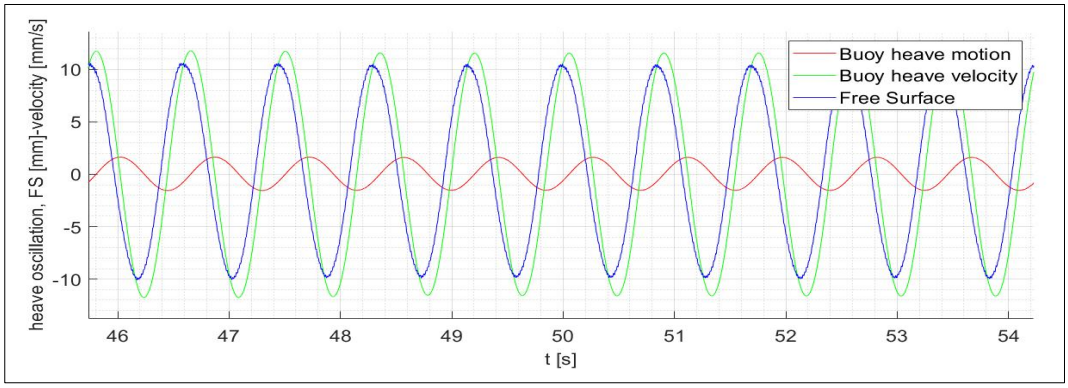

Figure 5.24 HEAVE model oscillation, velocity and free surface deformation against time for wave R06.

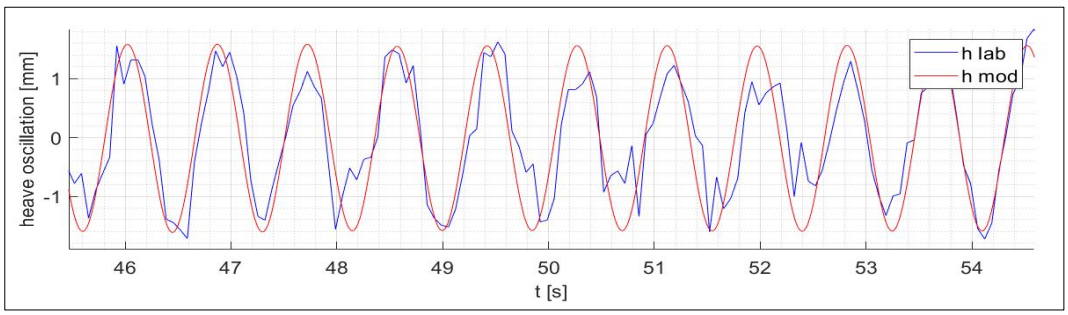

Figure 5.25 Comparison between model and laboratory HEAVE results for wave R06.

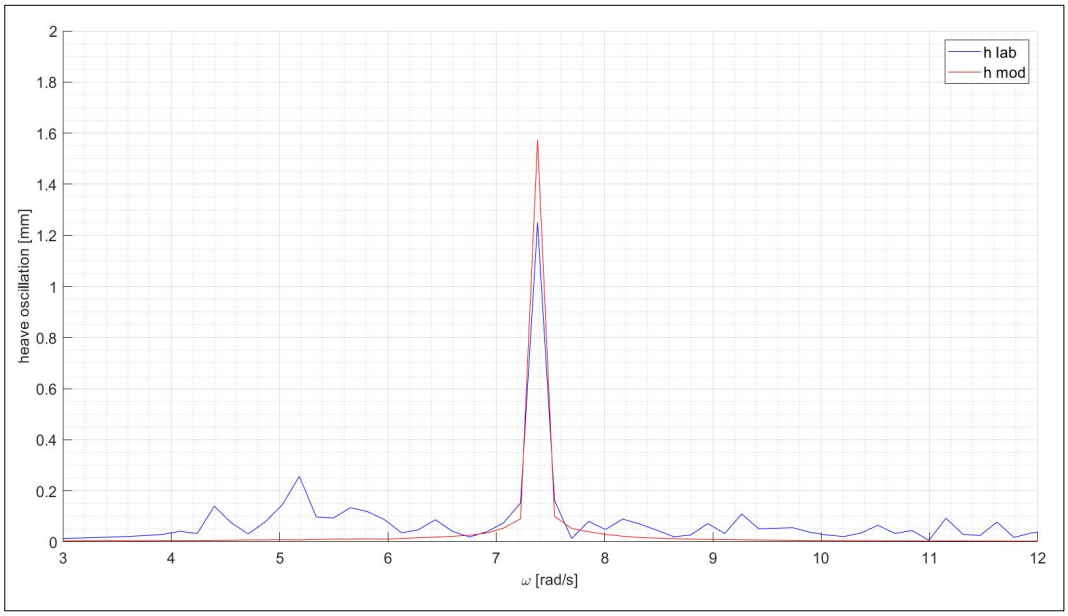

Figure 5.26 Frequency analysis of the comparison between model and laboratory HEAVE results for wave R06.

Pitch motion (R06)

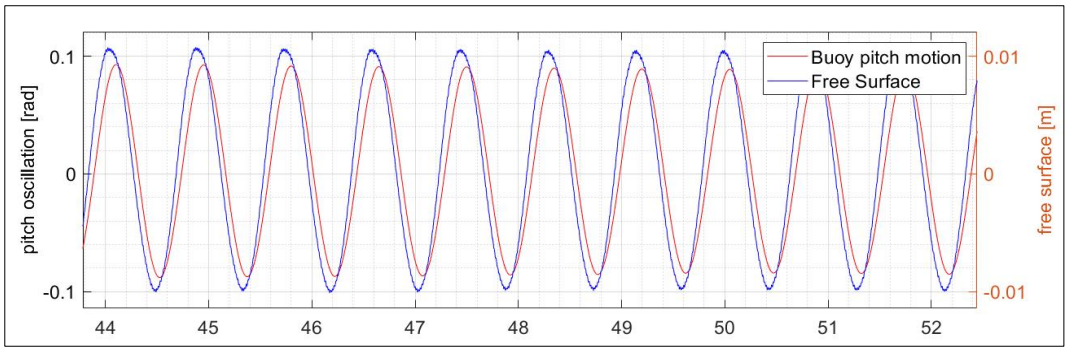

Figure 5.27 PITCH oscillation and free surface deformation against time for wave R06.

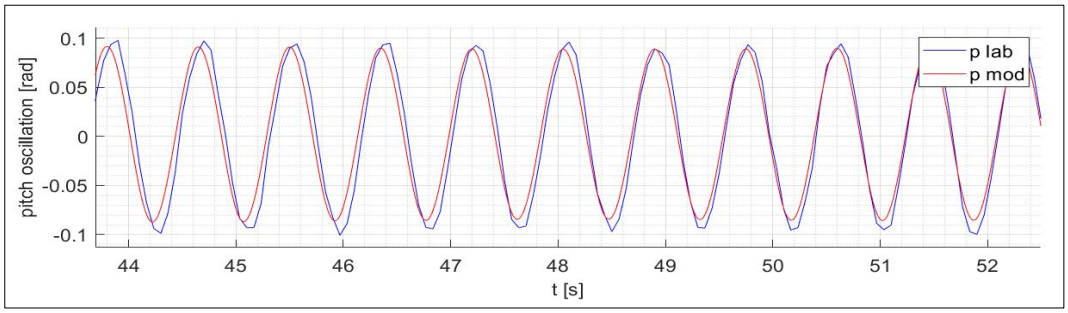

Figure 5.28 Comparison between model and laboratory PITCH results for wave R06.

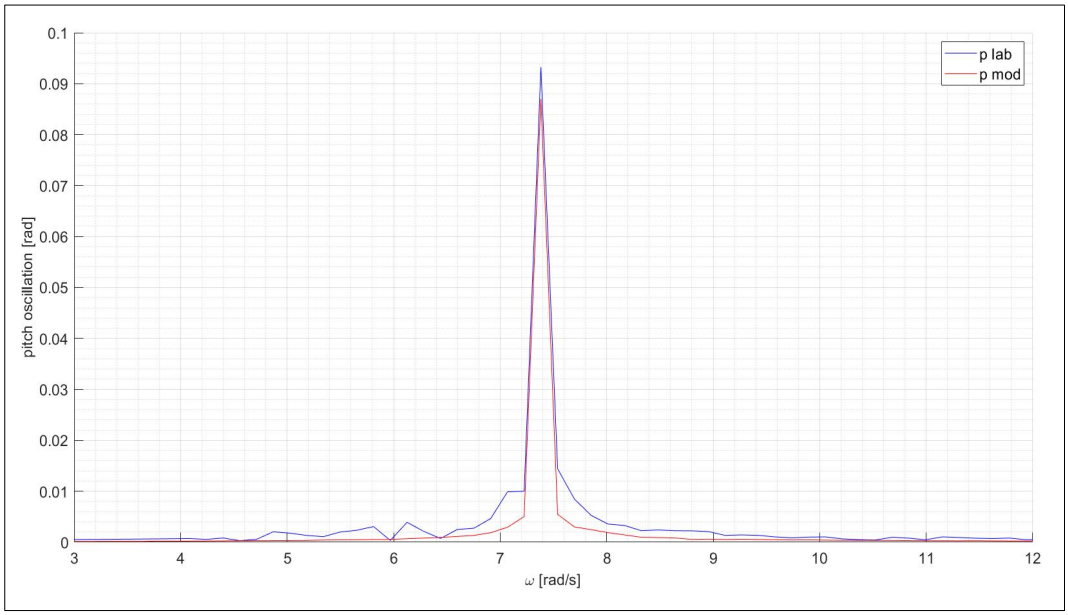

Figure 5.29 Frequency analysis of the comparison between model and laboratory PITCH results for wave R06.

The calibration coefficients inserted in the model in order to obtain previous results are shown in Table 5.03.

	surge	heave	pitch
K_{damp}	4.4	2.5	0
K_{stiff}	230	10	0.53

Table 5.03 Calibration coefficients for wave R06.

5.2.5 Wave R07

Surge motion (R07)

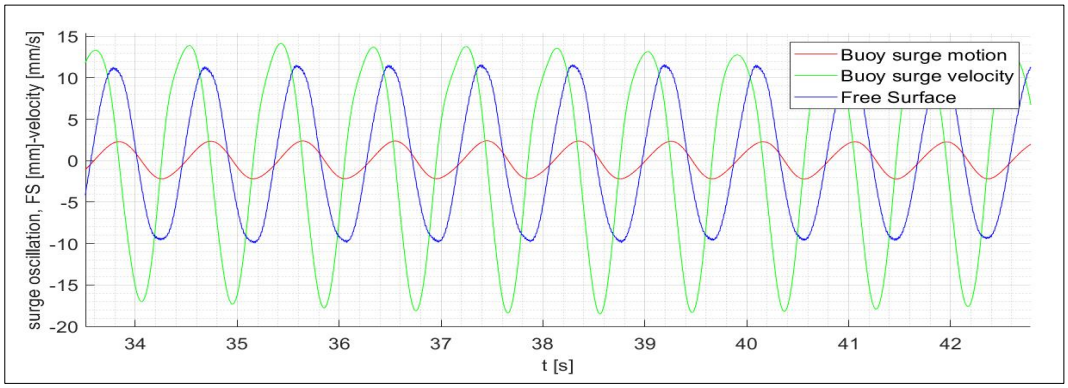

Figure 5.30 SURGE model oscillation, velocity and free surface deformation against time for wave R07.

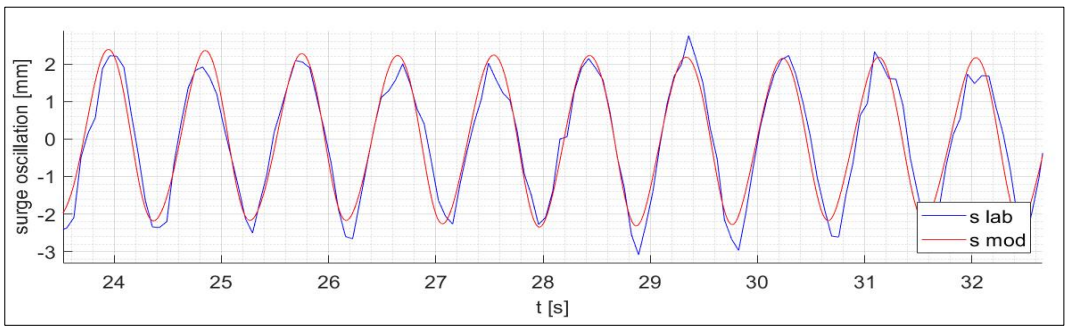

Figure 5.31 Comparison between model and laboratory SURGE results for wave R07.

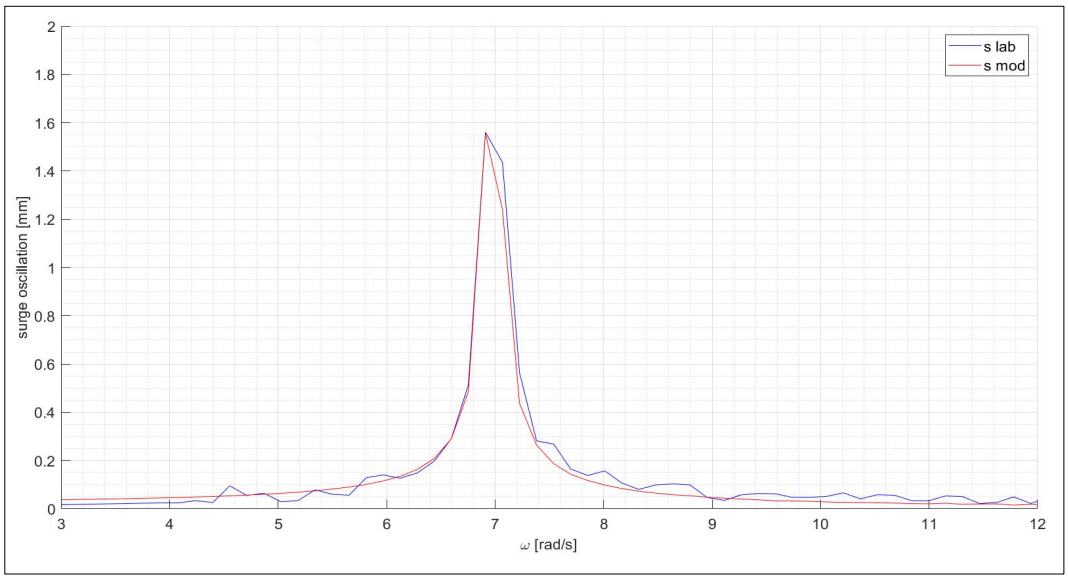

Figure 5.32 Frequency analysis of the comparison between model and laboratory SURGE results for wave R07.

Heave motion (R07)

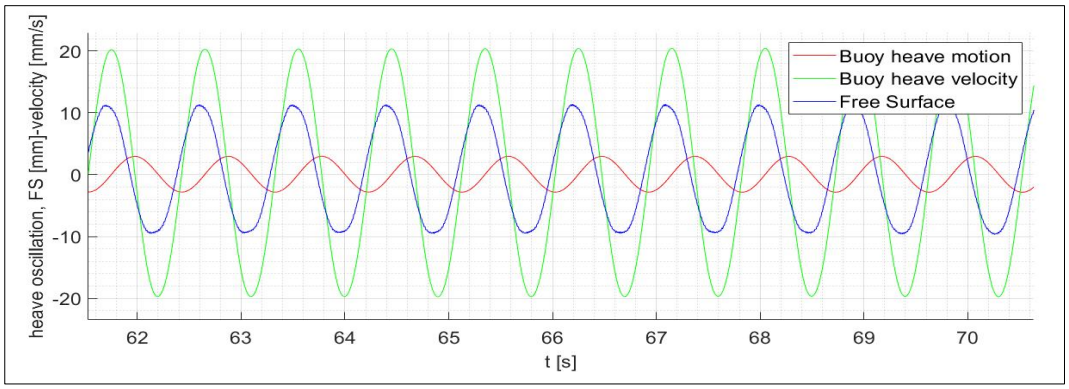

Figure 5.33 HEAVE model oscillation, velocity and free surface deformation against time for wave R07.

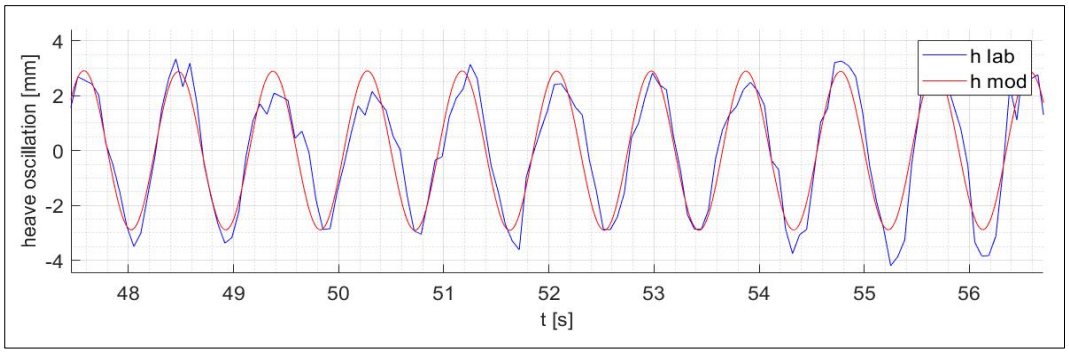

Figure 5.34 Comparison between model and laboratory HEAVE results for wave R07.

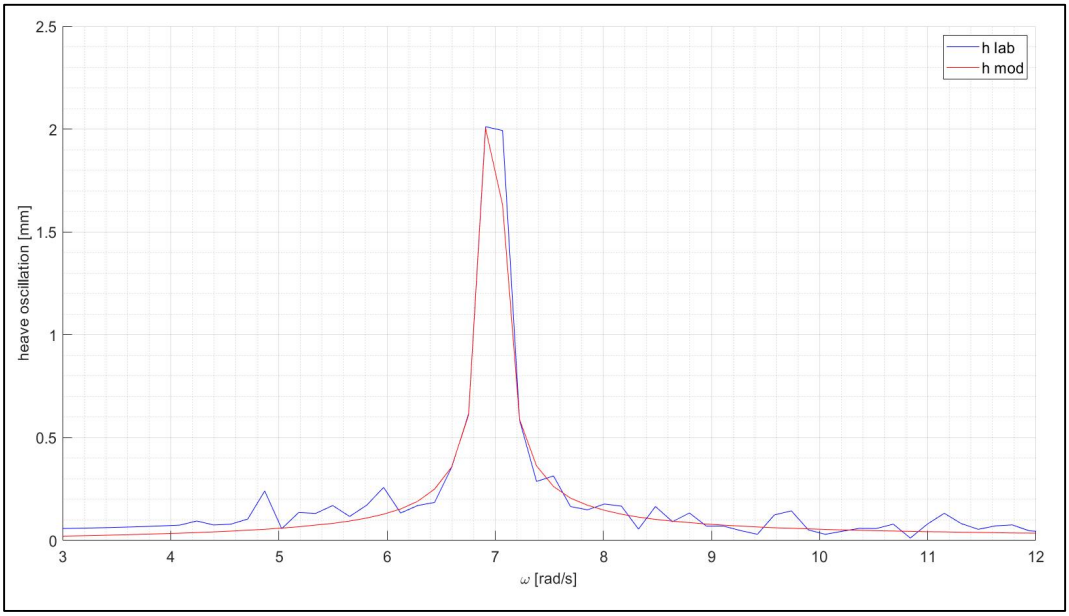

Figure 5.35 Frequency analysis of the comparison between model and laboratory HEAVE results for wave R07.

Pitch motion (R07)

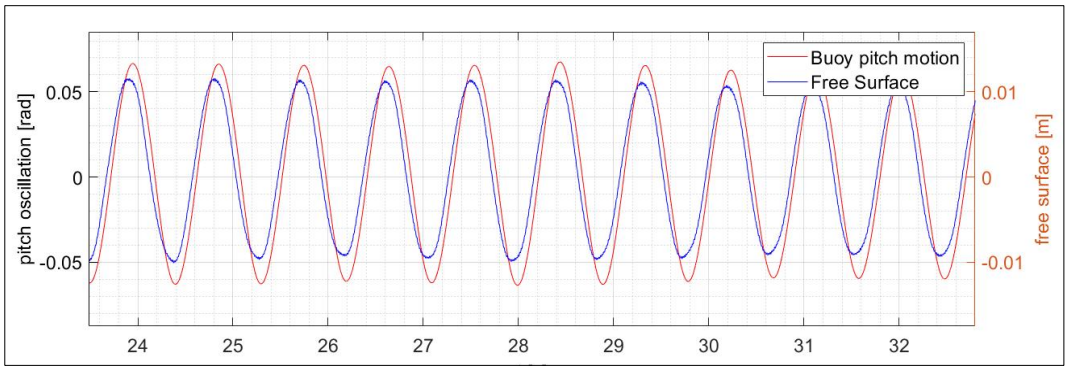

Figure 5.36 PITCH oscillation and free surface deformation against time for wave R07.

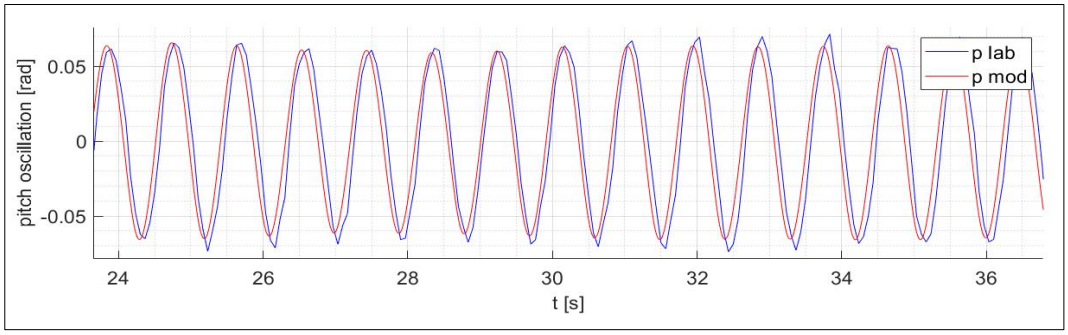

Figure 5.37 Comparison between model and laboratory PITCH results for wave R07.

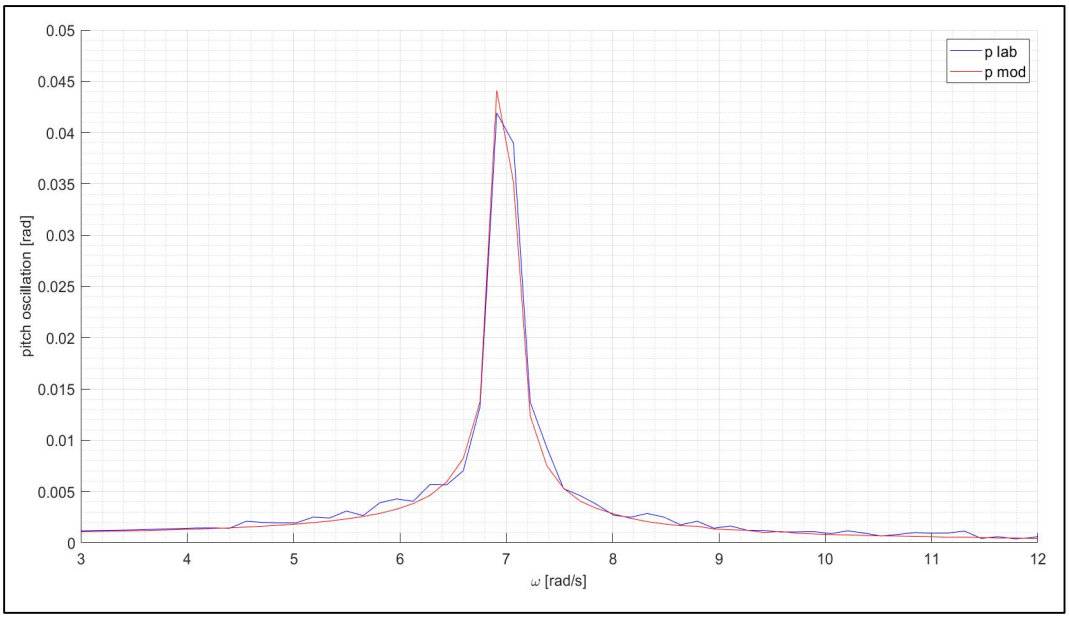

Figure 5.38 Frequency analysis of the comparison between model and laboratory PITCH results for wave R07.

The calibration coefficients inserted in the model in order to obtain previous results are shown in Table 5.04.

	surge	heave	pitch
K_{damp}	4.3	1.95	0
K_{stiff}	221	10	0.57

Table 5.04 Calibration coefficients for wave R07.

5.2.6 Wave R08

Surge motion (R08)

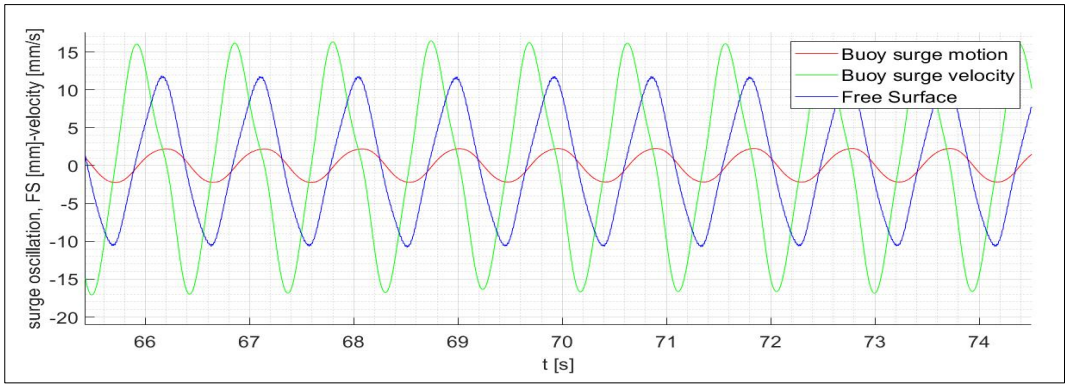

Figure 5.39 SURGE model oscillation, velocity and free surface deformation against time for wave R08.

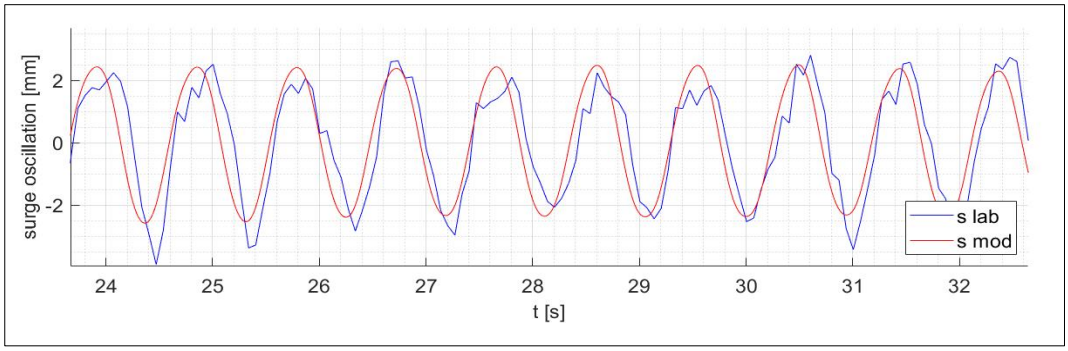

Figure 5.40 Comparison between model and laboratory SURGE results for wave R08.

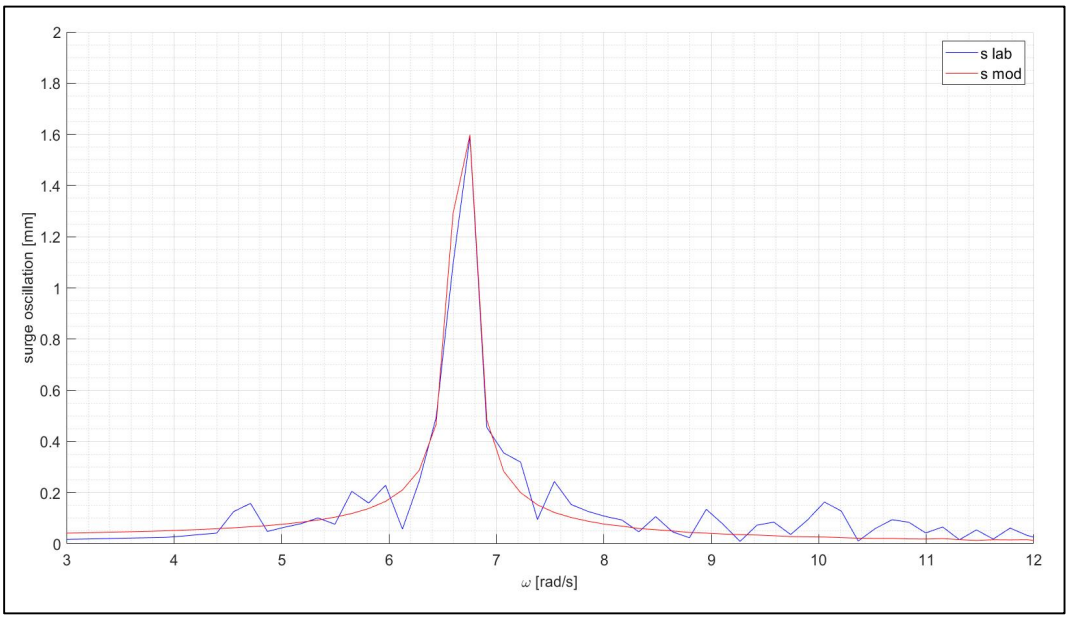

Figure 5.41 Frequency analysis of the comparison between model and laboratory SURGE results for wave R08.

Heave motion (R08)

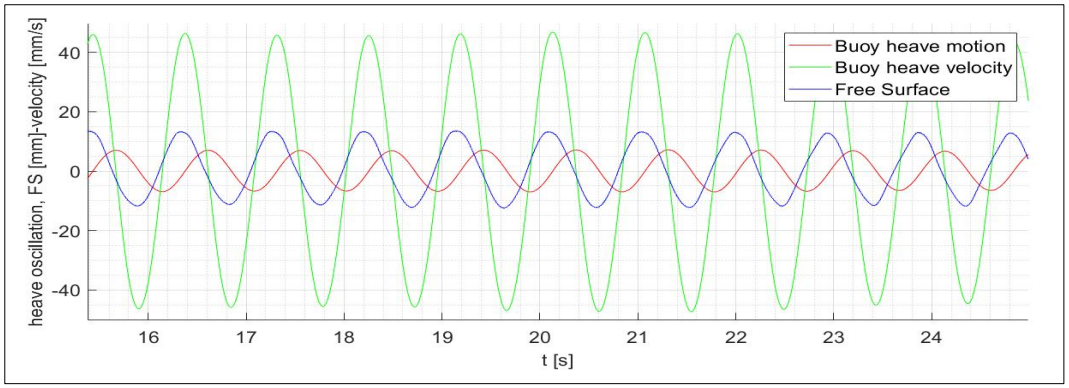

Figure 5.42 HEAVE model oscillation, velocity and free surface deformation against time for wave R08.

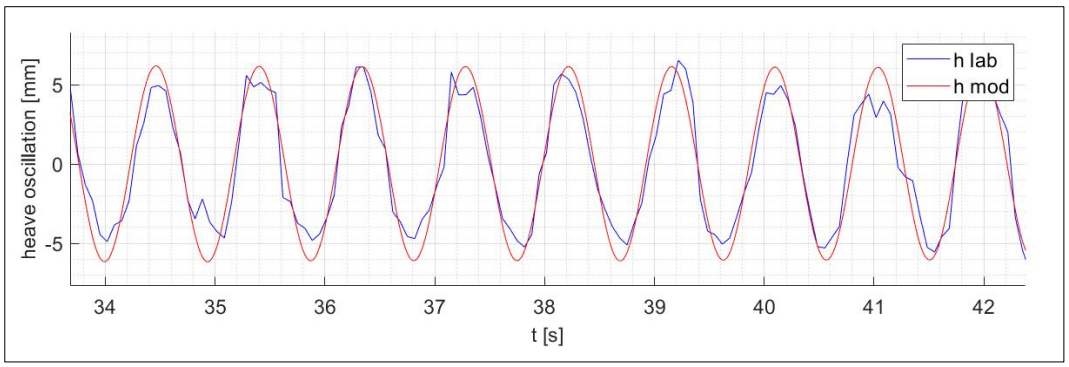

Figure 5.43 Comparison between model and laboratory HEAVE results for wave R08.

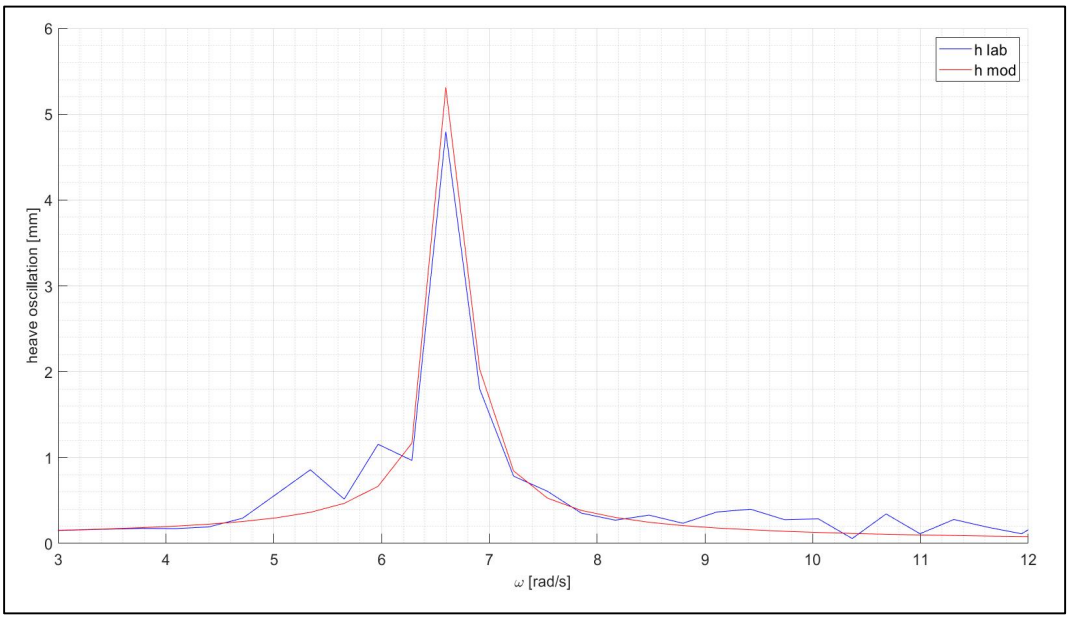

Figure 5.44 Frequency analysis of the comparison between model and laboratory HEAVE results for wave R08.

Pitch motion (R08)

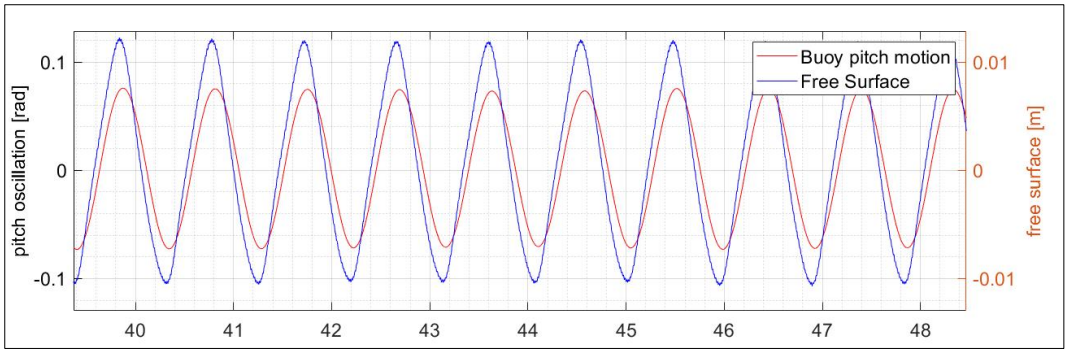

Figure 5.45 PITCH oscillation and free surface deformation against time for wave R08.

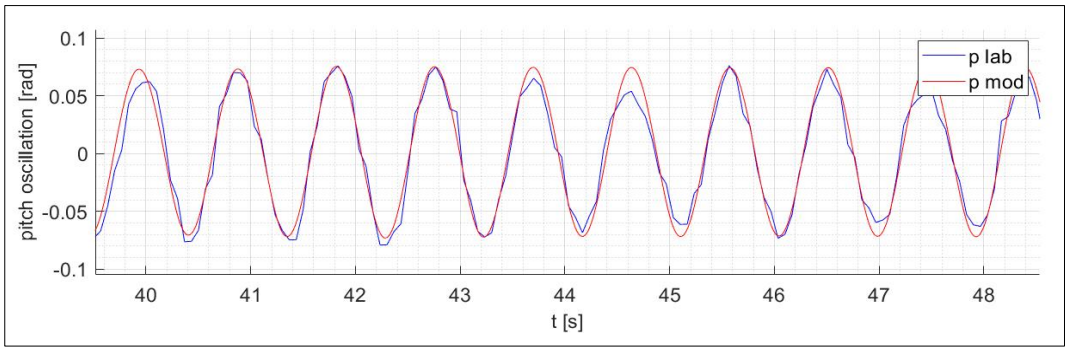

Figure 5.46 Comparison between model and laboratory PITCH results for wave R08.

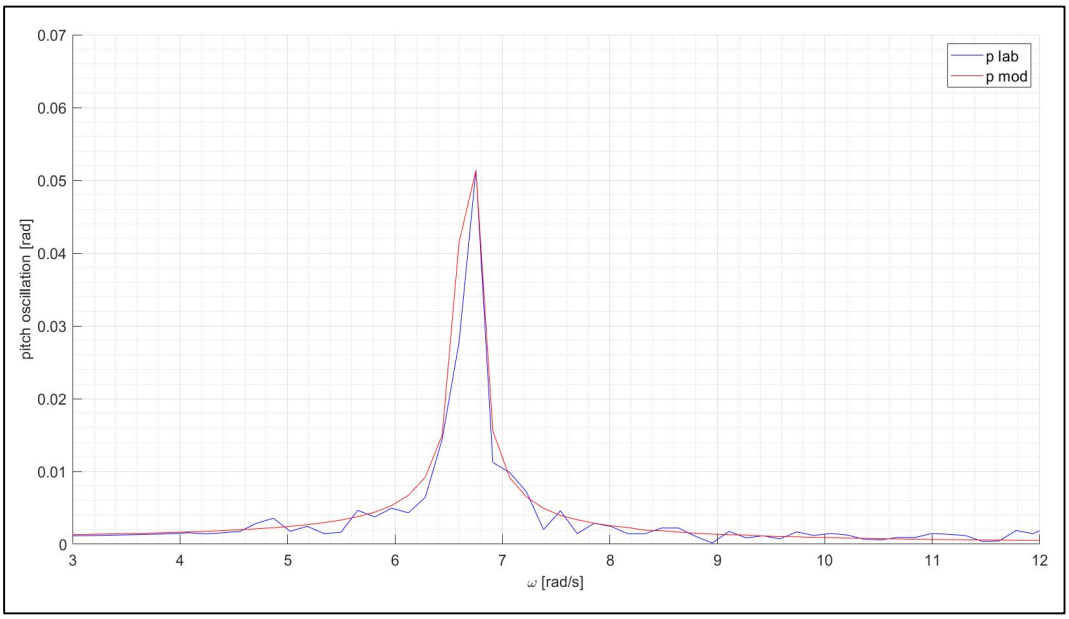

Figure 5.47 Frequency analysis of the comparison between model and laboratory PITCH results for wave R08.

The calibration coefficients inserted in the model in order to obtain previous results are shown in Table 5.05.

	surge	heave	pitch
K_{damp}	4.3	0.90	0
K_{stiff}	207	10	0.43

Table 5.05 Calibration coefficients for wave R08.

5.2.7 Wave R10

Wave R10 is the bigger among the tested ones, and, when it is generated, the situation in which catenaries are pulled to their maximum length takes place. As already explained in chapter 4, when this condition happens, the end-stop mechanism starts working in order to represent the mooring system effect. Being this mechanism function of the buoy position through the constant K_{moor}, a similar calibration process to the one previously described is necessary.

This wave case is more difficult to describe by the model than the previous ones. The most important reason why this happens is linked to the fact that, as explained in chapter 3, higher the wave height is, bigger are the reflection phenomena which arise during the test, and with them also transversal free surface displacements grow up. The latter effects bring the buoy to experience a different motion compared to the one that it would take without transversal effects. In particular, after the first seconds of test, the cylinder motion comes out from the plane described by the three DoFs considered for the development of this

work: a three dimensions model concerning also sway, roll and yaw DoFs could better represent the situation.

Surge motion (R10)

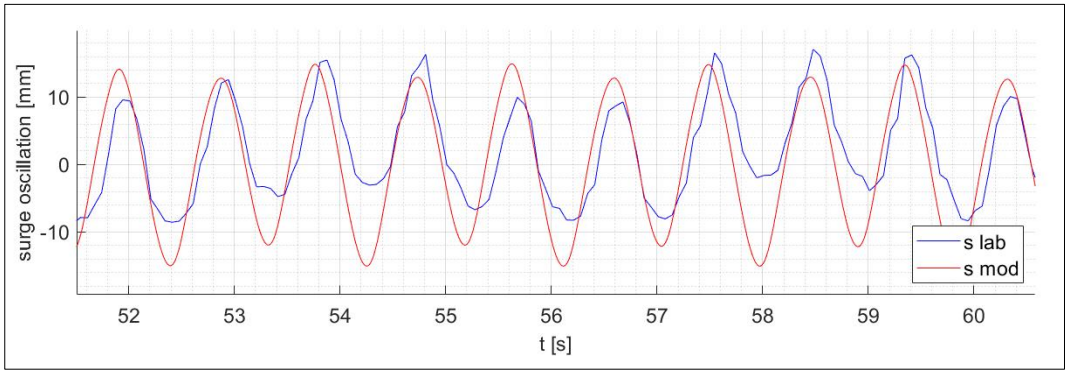

Figure 5.48 Comparison between model and laboratory SURGE results for wave R10.

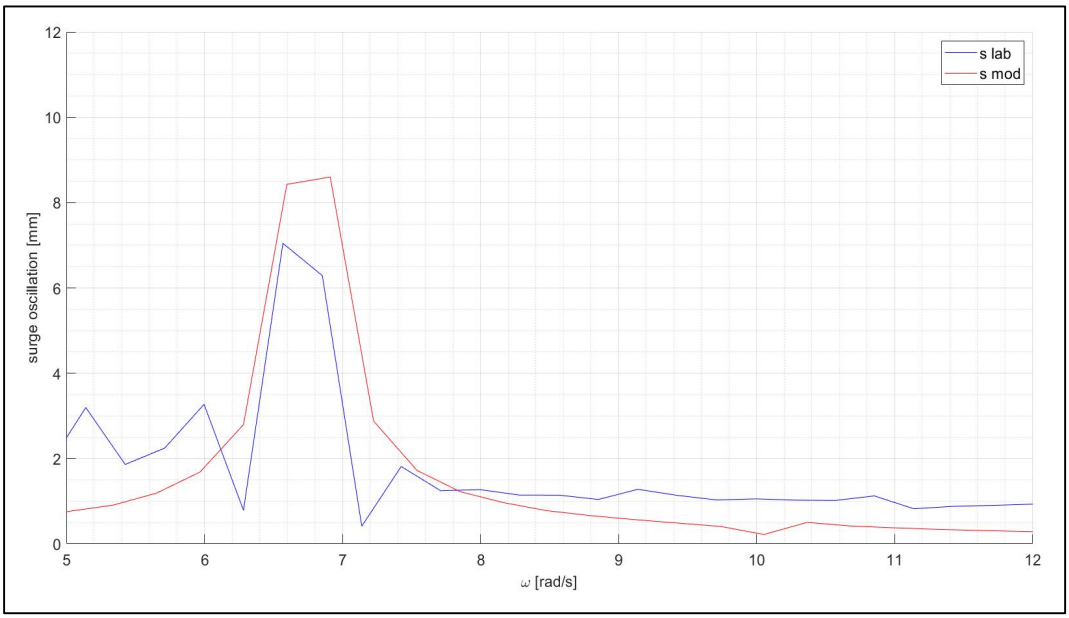

Figure 5.49 Frequency analysis of the comparison between model and laboratory SURGE results for wave R10.

Heave motion (R10)

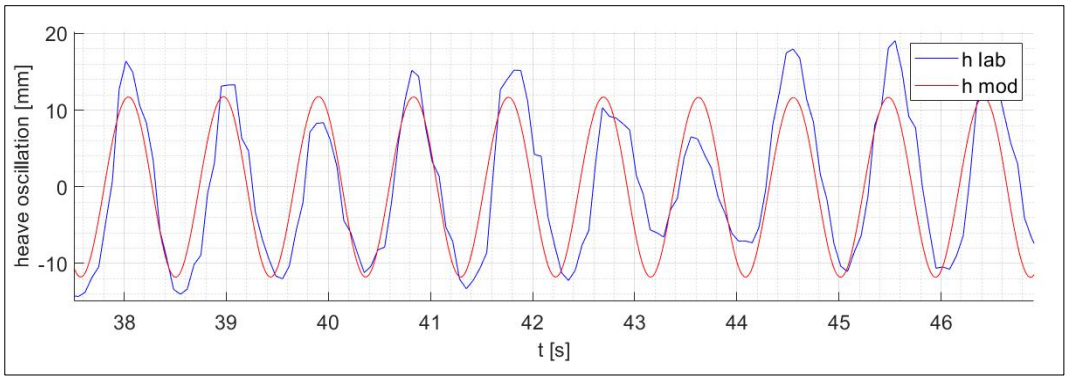

Figure 5.50 Comparison between model and laboratory HEAVE results for wave R10.

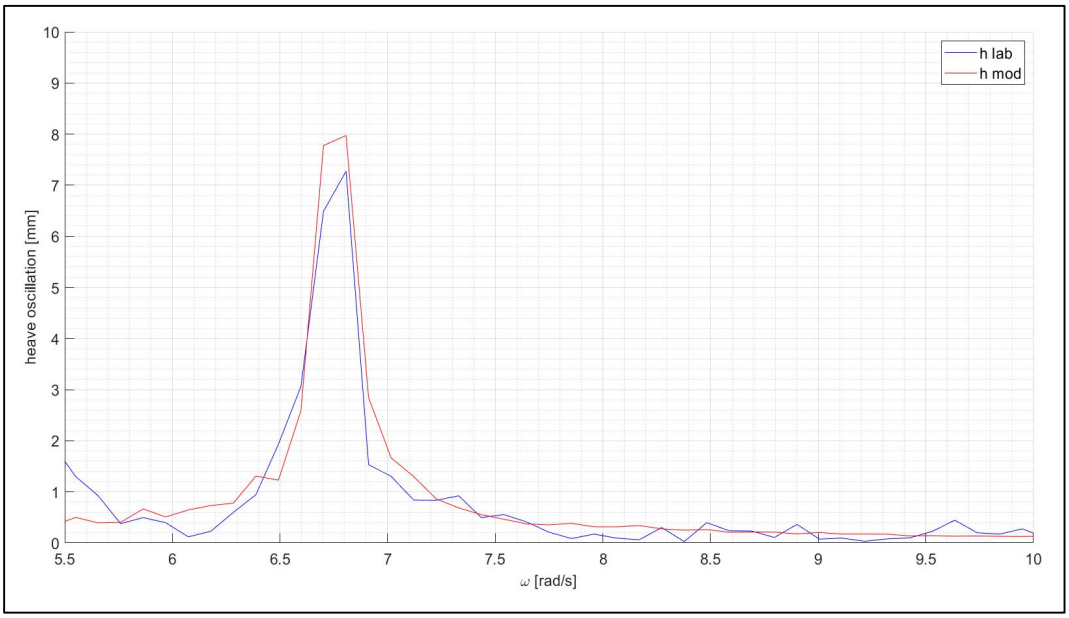

Figure 5.51 Frequency analysis of the comparison between model and laboratory HEAVE results for wave R10.

Pitch motion (R10)

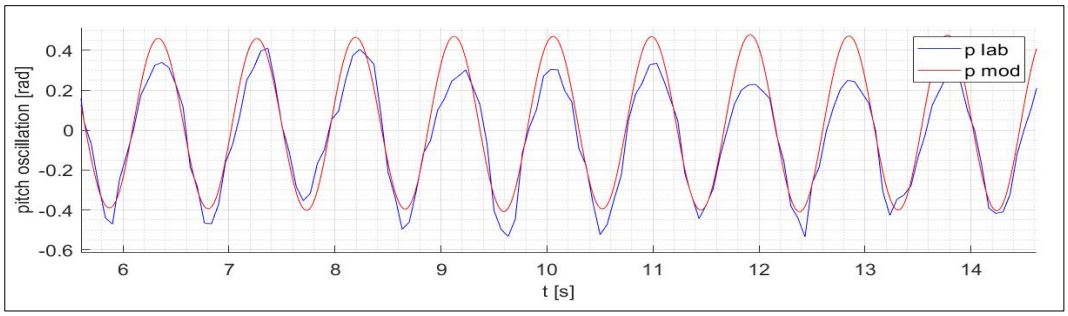

Figure 5.52 Comparison between model and laboratory PITCH results for wave R10.

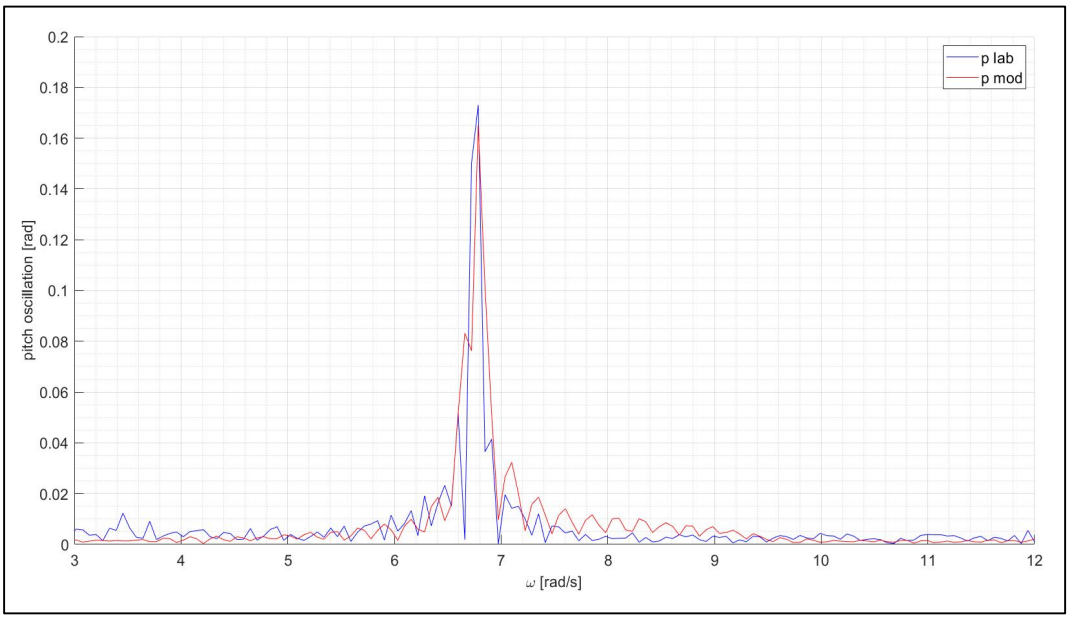

Figure 5.53 Frequency analysis of the comparison between model and laboratory PITCH results for wave R10.

The calibration coefficients inserted in the model in order to obtain previous results are shown in Table 5.06.

	surge	heave	pitch
K_{damp}	3	0	0.02
K_{stiff}	0	0	0
K_{moor}	4	4	4

Table 5.06 Calibration coefficients for wave R10.

5.2.8 Calibration of the coefficients

In this section, the trend of the calibration coefficients is determined for waves from R03 to R08.

In this situation, where the end-stop mechanism is not involved, the coefficients take a certain trend that is going to be discussed. The calibration process is influenced by a particular choice: since there can be several couples of K_{damp} and K_{stiff} capable of giving similar results, it has been chosen to maximize as much as possible the values assumed by K_{damp}, and consequently choosing the values of K_{stiff}. In particular, this decision is the consequence of the different effect that the two coefficients can bring to the solution. In fact, K_{damp} is multiplied, inside the motion equation, by the buoy velocity and together constitute the damping term which is responsible for a variation of the oscillation amplitude. On the other hand, K_{stiff} acts in the term of stiffness, where it is multiplied by

the buoy position. The stiffness term is then both responsible for reducing or enhancing the oscillation amplitude but is also able to produce a variation of the motion frequency.
In the following plots, different colours and symbols are used to represent the coefficients tendency. Blue is associated to waves R03, R05, R07 and R08 and red is related to R06. This particular subdivision is due to the fact that R06 and the other waves are characterised by different wave height-length ratio, as reported in Table 5.07.

WAVE	H/L
R03	0.0086
R05	0.0086
R06	0.0093
R07	0.0086
R08	0.0086

Table 5.07 H/L ratio of the tested waves.

Surge DoF

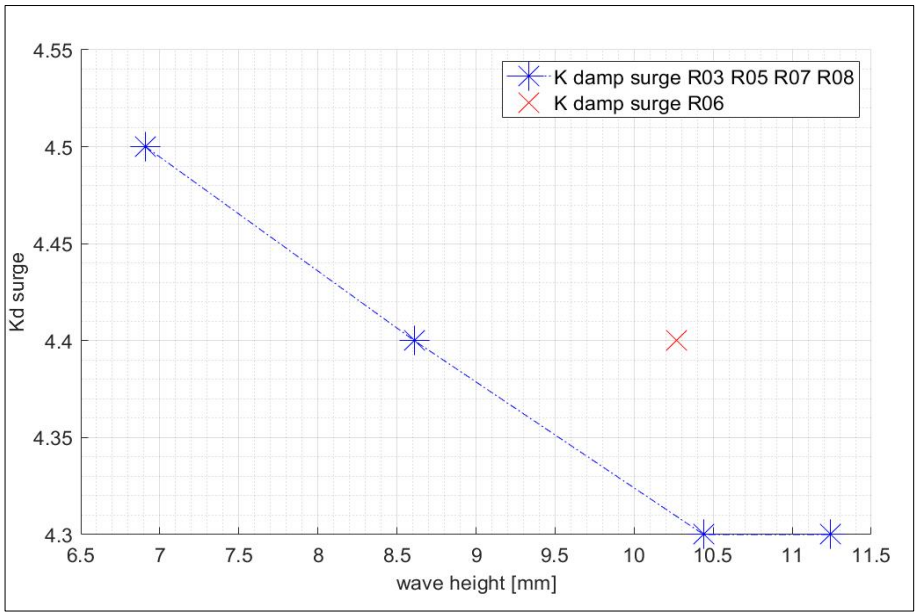

Figure 5.54 Trend of calibration coefficient K_{damp} against wave height along SURGE DoF.

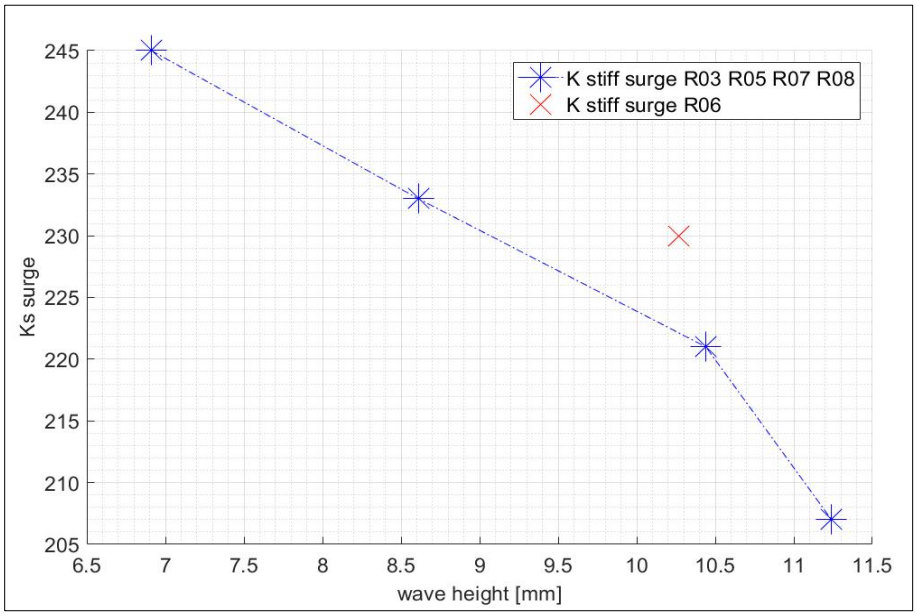

Figure 5.55 Trend of calibration coefficient K_{stiff} against wave height along SURGE DoF.

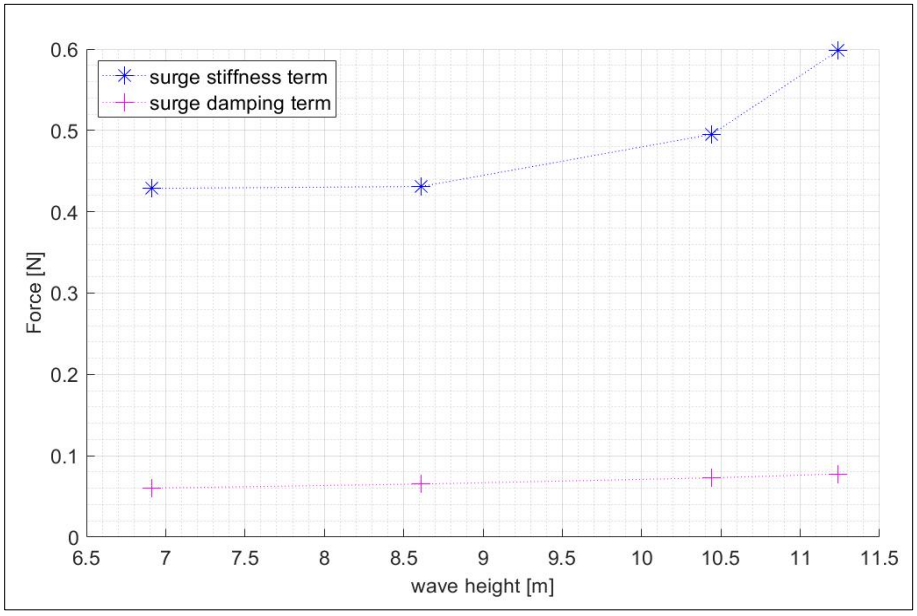

Figure 5.56 Peak values of stiffness and damping terms exploited by the mooring system along surge direction.

The calibration coefficients involved in the surge motion case define an evident trend. When wave height increase, both damping and stiffness coefficients decrease inside the interval described by the wave heights tested in this thesis. Nevertheless, not all the waves follow the same trend. As it is possible to see both in Figure 5.52 and Figure 5.51, the red points corresponding to wave R06 are positioned slightly away from the line described by the blue ones.

Although such decrease happens, it does not mean that the whole damping and stiffness terms grow lower with wave height. On the contrary, they tend to increase due to the correspondent enhancing of buoy displacements and velocities. This kind of behavior of the damping and stiffness terms, expressed as forces, is plotted in Figure 5.53. The values reported in the plot are obtained by multiplying the calibration coefficients and the amplitude of the oscillations of position and velocity functions derived from the model.

Heave DoF

A different trend is denoted in the case of heave motion. K_d keeps growing lower against wave height, but according to a more extended spot than in surge case. R06 keeps maintaining a slightly higher value of K_d compared with the waves of the same height, but H/L ratio as the other ones.
On the other hand, K_s varies a lot its tendency taken along surge motion: it becomes lower and constant throughout the entire wave height interval. The reason why it takes small values has to be linked to the smaller effect produced by the mooring system along this direction, as reported at the beginning of this section.

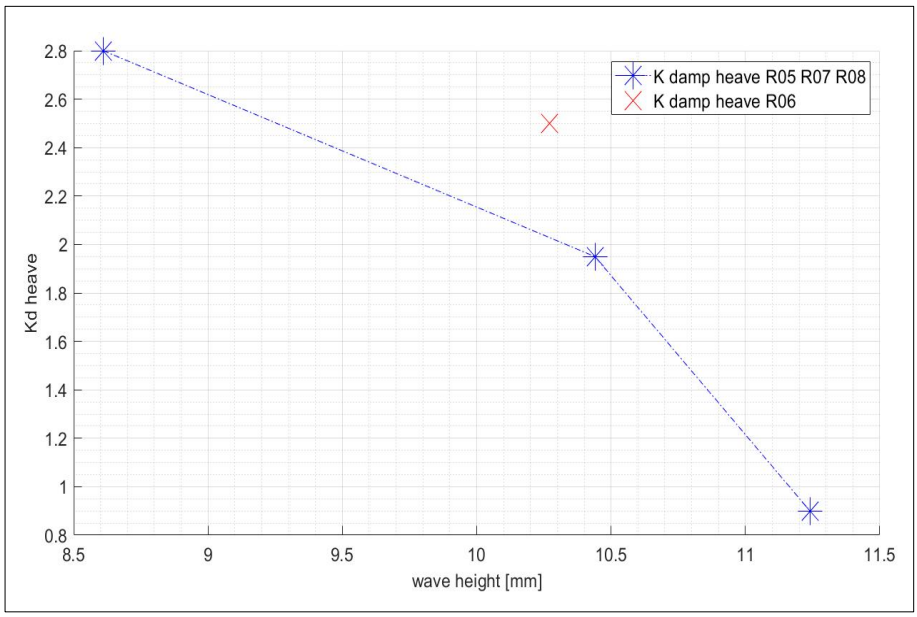

Figure 5.57 Trend of calibration coefficient K_{damp} with respect to wave height along HEAVE DoF.

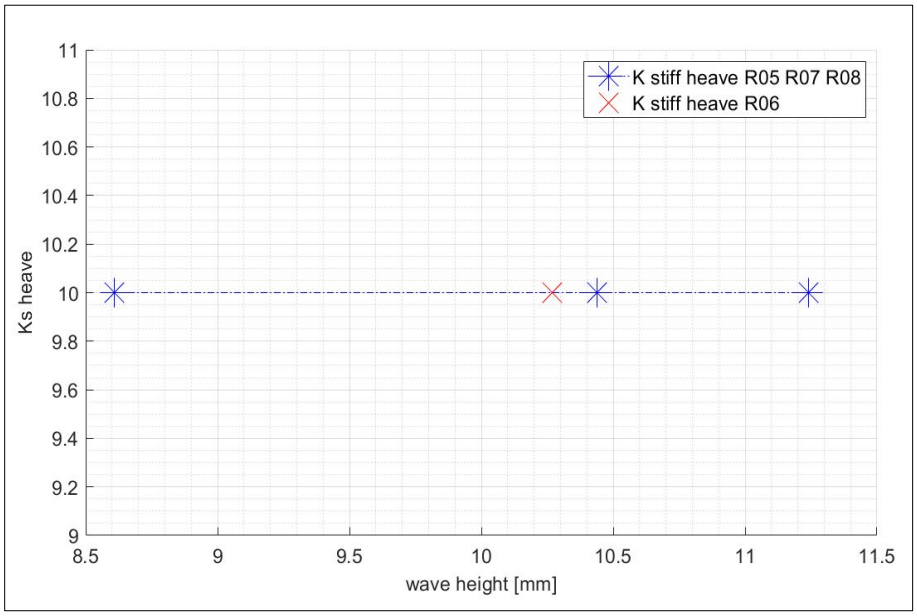

Figure 5.58 Trend of calibration coefficient K_{stiff} with respect to wave height along HEAVE DoF.

Pitch DoF

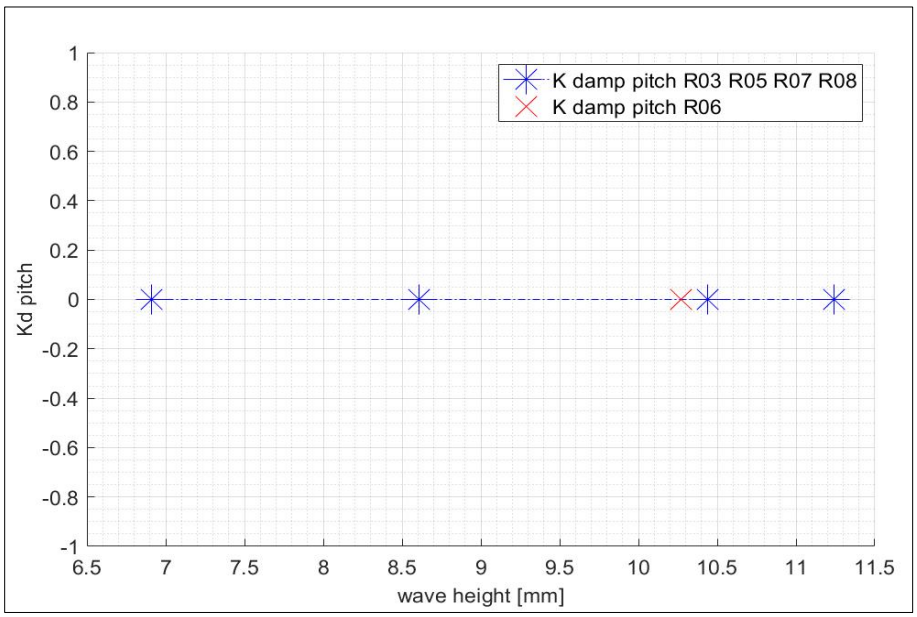

Figure 5.59 Trend of calibration coefficient K_{damp} with respect to wave height along PITCH DoF.

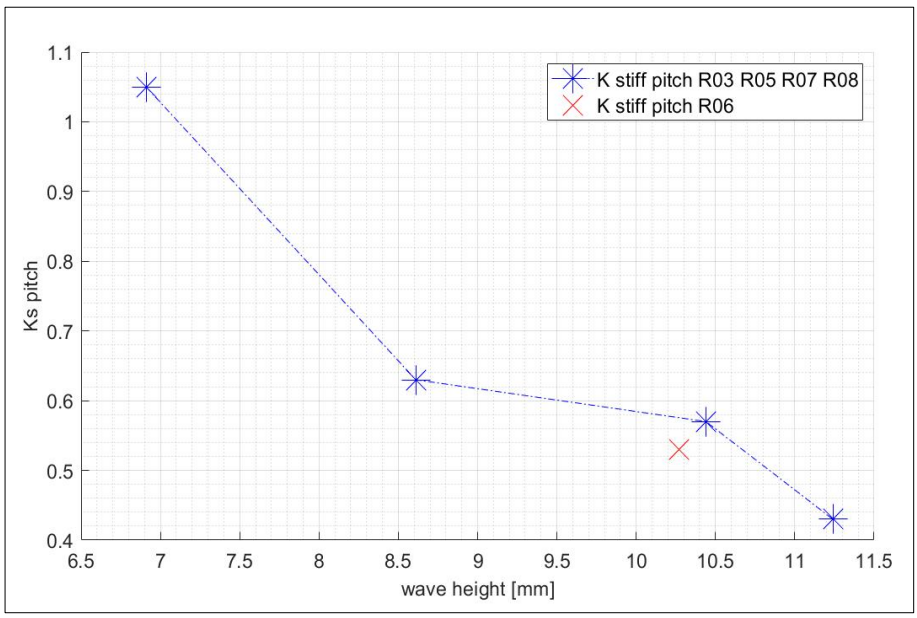

Figure 5.60 Trend of calibration coefficient K_{stiff} with respect to wave height along PITCH DoF.

Pitch rotation is not as influenced as surge and heave translations by the mooring system action, and this characteristic is reflected in the calibration coefficients values. As stiffness coefficients for the heave motion case, K_d used for the pitch motion is constant and assumes the null value, both for blue and red waves independently from the H/L ratio.
Stiffness coefficient K_{stiff} experiences instead a similar variation as it happens in surge case. Despite this similarity, a difference is clearly visible: the coefficient linked to wave R06 does not reply surge and heave examples but seems to follow the tendency expressed by blue points.
At the end, due to the conditions defined by the set up and the characteristics of the body, it is clear that the force exploited by the mooring system is different along the three DoFs, and in particular it is higher for the surge direction, and then it grows lower from heave case, reaching the smallest values for what pitch is concerned.

6

Conclusions

In this thesis, a numerical model based on the potential flow theory has been developed to describe the main dynamics characteristics of a floating body which undergoes a solicitation given by a regular sea state.
The main feature of the model is represented by its simplicity, and its implementation is based on some assumptions and hypothesis: diffraction effect has been considered negligible on the basis of the Koulegan-Carpenter number and on the dimensions of the buoy diameter compared to the wave length. Then, the drag force has been taken into account for translations only (surge and heave), neglecting it for the pitch. Furthermore, due to the water particles velocities along with water depth, it has been decided to discard the idea of involving it in the computation of the drag forces, considering the buoy velocity the only one that compares in the drag force formula. One more little approximation is found in the definition of a discrete frequency interval which the hydrodynamic coefficients are defined on. In particular, when the wave frequency does not perfectly match a value contained in the frequency vector, the coefficients selected are a little bit different from the correct one. At the end, the forces involved are modelled in a simple way, maintaining them linear ones, except for drag force.
In this thesis, the dynamics of a cylinder moored at the bottom with catenaries type mooring system has been considered. The new terms given by the presence of the mooring systems have been represented by linear terms, which need a calibration process.
Laboratory tests measuring the dynamics of a floating cylinder carried out at LIDR (Laboratory of Hydraulic Engineering of Alma Mater Studiorum University of Bologna) were used to calibrate the numerical tests.
The cylinder was 355 mm high, with a 25 mm radius and a total mass of 600 g, while the catenaries were 350 mm long. An image processing analysis of the videos was carried out in order to detect the main dynamics of the experimental floating body. Both frequency domain and time domain analysis were performed. The calibration of the mooring stiffness (K_S) and damping (K_D) coefficients was performed by comparing laboratory analysis and model results of both the time series of surge, heave and pitch DoF and their frequency behavior.
The involvement of calibration coefficients makes the model lost a general validity, being the coefficients related to the particular body, mooring system and other laboratory set-up characteristics. The trend taken by the calibration coefficients allows to run the model and obtain consistent results for this particular set-up in a wide range of wave conditions.

We have observed a linear trend of the calibration coefficients along with the wave heights, maintaining a certain H/L ratio. If some differences with the current set-up, in terms of mooring system and body characteristics, arise, it is clear that the calibration coefficients should be determined once again. Despite this, all the other parts of the model keep being applicable to any other floating body. The determination of the computation mesh is, in fact, possible on every body shape due to the versatility of the Mesh tool that is able to create both symmetric and asymmetric grids. Besides, the final computation of the hydrodynamic coefficients through the function Nemoh is possible on every previously defined mesh.

The results show that the model performs well both in frequency and time, in the case of waves that do not provoke the chains to be pulled at their maximum length. This condition verifies for test waves R03 (H=6.91mm, T=0.72 s), R05 (H=8.23 mm, T=0.82 s), R06 (H=10.27 mm, T=0.85 s), R07 (H=10.44 mm, T=0.90 s) and R08 (H=11.23 mm, T=0.94 s). This is important because it means that the model is useful for the situations in which the system should work.

During the test with wave R10 (H=33.50 mm, T=0.93 s), with the maximum simulated wave height, the catenaries become tight at most of the time. In this case the results are not as good as in the previous cases, because of the presence of transversal forces that make the model to slightly overestimate the oscillation. For this reason, when wave height takes such high values as in wave R10 case, the consideration of the reflection phenomenon could be taken into account. There are several methods devoted to the quantification of the reflection phenomenon, such as the one described by [31], where only two wave gauges were used and noise cancellation was not possible. It works both in case of regular and irregular waves. The model works in a good way concerning frequency determination.

Free decay test results show a good agreement between model and laboratory as well. Since in this situation the catenaries effect is practically negligible, it confirms that the code works well to simulate the free floating bodies dynamics.

In conclusion, the model represents a valid and quick tool in order to have an overview of the body dynamics both in frequency and time domain. In order to obtain more precise and accurate results, more complicate models or CFD methods should be taken into account, allowing better results but with a lot higher computation costs.

In the future, some model improvements could be performed especially for what the mooring system is concerned. Some models able to represent the effect of the mooring system in a precise way have already been developed (see [8, 25]), but they are very complicated and it would have no sense to insert them into a simple model like the one treated in this thesis, both for the simplicity of the rest of the code and for the aim that this model is supposed to have. More simplified mooring system model than the cited ones could be enough in order to give the code a sort of generality, allowing it to be applied to any body with this type of mooring system.

Bibliography

[1] R. K. Pachauri, L. A. Meyer L. A., Core Writing Team. Ipcc, 2014: Climate change 2014: Synthesis report. contribution of working groups I, II and III to the fifth assessment report of the intergovernmental panel on climate change, 2014.

[2] URL https://www.irena.org. Accessed: 26/04/2019.

[3] URL https://www.iea.org/tcep/power/renewables/offshorewind/. Accessed: 26/04/2019

[4] URL https://greennetwork.it. Accessed: 27/04/2019.

[5] M.E. McCormick. Ocean Engineering Mechanics. Cambridge University Press, 2010.

[6] R.G. Dean, R.A. Dalrymple. Water wave mechanics for engineers and scientists. World Scientific, 41-77, 1991.

[7] P. De Girolamo, L. Franco, A. Noli. Notes "Fondamenti di oceanografia e idraulica marittima per ingegneria", 119-195, 2003.

[8] A. Moreno Miquel. Development, analysis and comparison of two concepts for wave energy conversion in the Mediterranean Sea. PhD thesis, 2017.

[9] P. Biscari, T. Ruggeri, G. Saccomandi, M. Vianello. Meccanica Razionale. Springer, 75-94, 2013.

[10] A. Moreno Miquel. Wave Energy Conversion, Numerical modelling. DICAM - Alma Mater Studiorum Università di Bologna. Lecture, 2018.

[11] A. Campos, C. Molins, X. Gironella, P. Trubat, D. Alarcón. Experimental RAO's analysis of a monolithic concrete spar structure for offshore floating wind turbines. In Proc. of the 34th International Conference on Ocean, Offshore and Arctic Engineering, Canada, 2015.

[12] Y.A. Cengel, J.M. Cimbala. Fluid mechanics. McGraw Hill education, 607-645, 2014.

[13] L.T. Alberti. Flow around cylindrical towers: the stabilising role of vertical ribs. Thesis presented in partial fulfilment of the requirements for the degree of Master of Civil Engineering at the University of Stellenbosch, 2006.

[14] G. Delhommeau. Numerical Simulation of Hydrodynarnics: shipsand Offshore Structures, Sea keeping codes AQUADYN and AQUAPLUS. Ecole Centrale de Nantes, 1993.

[15] URL https://lpsa.swarthmore.edu/NumInt/NumIntFourth.html. Runge-Kutta method of Fourth order. Accessed: 2/02/2019.

[16] URL https://www.researchgate.net/figure/Geometric-interpretation-of-the-fourth-order-Runge-Kutta- method. Accessed: 2/02/2019.

[17]URLhttp://www.diee.unica.it/misure/Dispense/Misure_Elettroniche_dm270/Analisi_di_segnali_campionati.pdf. PDF document, Università degli studi di Cagliari, 2010.

[18] URL https://www.mathworks.com/help/matlab/ref/fft.html. Accessed: 2/11/2019

[19] A. Paci, M.G. Gaeta, A. Antonini, R. Archetti. 3D numerical analysis of wave-floating structure interaction with OpenFOAM®. DICAM University of Bologna, 2016.

[20] M. Rahman Soeb, A.B.M. Saiful Islam, M. Zamin Jumaat, N. Huda, F. Arzu. Response of nonlinear offshore spar platform under wave and current. Ocean Engineering, 144:296-304, 2017.

[21] G. Passoni, S. Bozzi. Numerical modelling of wave energy converters - 10th exercise of Ocean and coastal engineering course. Politecnico di Milano, 2016.

[22] A. Babarit, G. Delhommeau. Theoretical and numerical aspects of the open source BEM solver nemoh. In Proc. of the 11th European Wave and Tidal Energy Conference (EWTEC2015), Nantes, France, 2015.

[23] P. Ricci, J. Saulnier, A.F. de O. Falcao, T. Pontes. Time-domain models and wave energy converters performance assessment. In Proc. of the 27th International Conference on Offshore, Mechanics and Arctic Engineering. 6:699-708, 2008.

[24] B. J. Koo, M. H. Kim, R. E. Randall. Mathieu instability of a spar platform with mooring and risers. Ocean Engineering. 31:2175–2208, 2004.

[25] E. Esmailzhade, A. Goodarzi. Stability analysis of a calm floating offshore structure. International Journal of Non-linear Mechanics. 36:917–926, 2001.

[26] Analytic Geometry. Encyclopaedia Britannica, 2008.

[27] L. Castro-Santos, V. Diaz-Casas. Departamento de Exeñaria Naval e Océanica, Universidade da Coruña Ferrol, Spain. Floating Offshore Wind Farms. Springer, 2016.

[28] AQWA User Manual. http://www.ansys.com/Products/Structures/ANSYS- Aqwa.

[29] A. Babarit. On the park effect in arrays of oscillating wave energy converters. Renewable Energy, 58:68–78, 2013.

[30] G. Delhommeau. Les problemèmes de diffraction-radiation et de résistance de vagues: étude théeorique et résolution numérique par le method des singularités. PhD thesis, E.N.S.M. Nantes, 1987.

[31] Y. Goda, Y. Suzuki. Estimation of Incident and Reflected Waves in Random Wave Experiments. 1:828–845, 1976.

[32] J.N. Newman. The evaluation of free surface green functions. In Proc. Of the 4th International Conference on Ship Hydrodynamics. Washington, 1985.

[33] M. Sadraey. Aircraft Performance. VDM Verlag, 2011.

[34] Wamit user manual. http://www.wamit.com/manual.htm.

[35] J. Twidell, T.Weir. Renewable Energy Resources. Routledge, 2015.

[36] URL https://lheea.ec-nantes.fr/...et.../nemoh. Lheea website for the nemoh toolbox. Accessed: 29/10/2018.

[37] J.M.J. Journée, W.W. Massie. ”OFFSHORE HYDROMECHANICS”, First Edition, Delft University of Technology. Chapter 12, 2001.

[38] G.B. Airy. On tides and waves. Encyclopaedia Metropolitana. 5:241–396, 1845.

[39] G.F. Rosetti, G. Vaz, A.L.C. Fujarra. URANs calculations for smooth circular cylinder flow in a wide range of Reynolds numbers: solution verification and validation. In Proc. of the 31st International Conference on Ocean, Offshore and Arctic Engineering. 5:549-571, 2012.

[40] A. Moreno Miquel, A. Antonini, R. Archetti, S. Bozzi, A. Lamberti. Non-linear modelling of a heaving point absorber: the surge effect. International Journal of Marine Energy, 19:95-109, 2017.

[41] S. Bozzi, A. Moreno Miquel, A. Antonini, G. Passoni, R. Archetti. Modelling of a point absorber for energy conversion in Italian seas. Energies, 6:3033–3051, 2013.

[42] S. Bozzi, M. Giassi, A. Moreno Miquel, A. Antonini, F. Bizzozero, G. Gruosso, R. Archetti, G. Passoni. Wave energy farm design in real wave climates: the Italian offshore. Energy. 122:378-389, 2017.